

Gravity-Driven Microfiltration for Enriching Circulating Tumour Cells and Clusters

Nicholas Chahley

Department of Biomedical Engineering
Integrated Program in Neuroscience
McGill University
Montreal, Canada

April 2022

*A thesis submitted to McGill University in partial fulfillment
of the requirements of the degree of
Master of Science*

Contents

List of Figures	ii
Acknowledgments	iii
Abstract	iv
Résumé	vi
1 Introduction and Thesis Objectives	1
1.1 Introduction	1
1.2 Thesis Objectives	2
1.2.1 Aim 1: Fabrication of High-Throughput Polymer Microfilters	3
1.2.2 Aim 2: Automated Image Acquisition	3
1.2.3 Aim 3: Clinical Study of cCTC Incidence in CRCLM	3
2 Background Information	4
2.1 Rationale for Liquid Biopsy	4
2.2 History of Circulating Tumour Cell Clusters	7
2.3 Biology of Circulating Tumour Cell Clusters	8
2.4 Isolation of CTC Clusters	10
2.4.1 Cluster-Specific Isolation Technologies	12
2.4.2 Gravity Driven Microfiltration	13
2.5 Limitations of the G _μ F Platform	16
3 Aim 1: Fabrication of High-Throughput Polymer Microfilters	19
3.1 Methods	19
3.2 Results	22
3.3 Discussion	26
4 Aim 2: Automated Image Acquisition	26
4.1 Methods	27
4.2 Discussion	30
5 Aim 3: Clinical Study of cCTC Incidence in CRCLM	31
5.1 Methods	32
5.1.1 Participants	32
5.1.2 Isolation of CTCs from Blood by Gravity Microfiltration	35
5.1.3 Immunofluorescent Labeling of Captured Cells	36
5.1.4 Image Classification	36
5.2 Results	36
5.3 Discussion	38
6 Conclusion	42

References	45
Appendices	55
A Manuscript Contribution	55

List of Figures

1	Overview of circulating tumour cell clusters	9
2	Schematic of the gravity microfiltration (G μ F) platform	15
3	Time-course study for one metastatic HGSC patient	17
4	Mold preparation and assembly	21
5	Mold filling and demolding	22
6	Comparison of master mold photomask layouts	23
7	Cleaning PDMS top-off from silicon mold using TBAF/NMP etching	25
8	ROI partitioning of a 8 mm diameter filter	29
9	Illustration of histological growth pattern (HGP) morphologies in CRCLM	33
10	Examples of cells isolated from CRCLM patients	37
11	CTC and cCTC concentration	39
12	CTC cluster size distribution	40

List of Tables

1	CRCLM patient information	34
2	CRCLM CTC counts	38

Acknowledgments

I would like to thank Prof. David Juncker for the opportunity to work in his lab, and his supervision and support throughout this degree. This work was made possible by the resources and expertise made available by the Juncker Lab, and it has been a privilege to work with a group of such talented and broadly disciplined scientists. These friends and colleagues have provided continuous guidance, support, and camaraderie over these years. Special thanks to Oriol Ymbern, Molly Shen, Zijie Jin, Andrew Tan, Philippe DeCorwin-Martin, and Grant Ongo for the marks they've made on my life. To Anne Meunier, Alex Hernandez, and Newsha Koushki, who were my teachers and CTC team alumni, and to Stephanie Petrillo and Laudine Communal for their help and coordination of clinical samples. Thank you to Dr. Anne-Marie Mes-Masson and Dr. Peter Metrakos for allowing me access to their labs and their collaboration on this project. My deepest gratitude to Dr. Andy Ng for his saintly patience and extremely effective feedback during the writing of this document.

Thank you to Michael Blough and my friends from the Charbonneau in Calgary, whom I admire and miss dearly — your mentorship and belief helped inspire me to move across the country in pursuit of my goals. Exponentially so to my parents and sister for their undying support and pride. To my friend Maverick, for his companionship these last few years in Montreal. Finally, and most of all, to Marie — for everything.

Abstract

Cancer is a leading cause of death worldwide, and metastatic lesions the primary mortal complication in solid tumour cancers. Tumour characterization by tissue biopsy is an invasive process that fails to fully account for widely prevalent spatiotemporal heterogeneity due to being assessed on a limited fraction of tissue taken at a single site and timepoint. Biopsy is often taken only during surgical resection, this can deny patients improved treatment informed by understanding tumour phenotype or worse, subject patients to costly and even harmful unnecessary treatment. This is true of colorectal cancer liver metastasis (CRCLM) in Canada, where patients receive pre-operative bevacizumab, which worsens outcome in a histological growth pattern (HGP) that is only diagnosed after the surgery.

Circulating tumour cells (CTCs) in blood have a demonstrated clinical significance and are used for prognosis and monitoring in a wide range of cancers. They are much more rarely found as clusters (cCTCs), which have increased metastatic potential and may contain tumour-associated stromal and immune cells. However, most of the commonly used CTC isolation technologies are designed for isolating single cells and do not capture many cCTCs. The Juncker Lab has developed a gravity-driven microfiltration (G μ F) platform suitable for the enrichment of single cell CTCs (scCTCs) and CTC clusters from blood samples on the basis of their size and mechanical properties. The platform has demonstrated excellent capture efficiency with spiked cells and has lead to exciting findings of cCTCs in ovarian cancer patients. However, bottlenecks in sample and analysis throughput need to be overcome to take advantage of the platform's strengths in large-scale studies.

This works goes towards increasing the scalability of the G μ F platform. First, high open-ratio membranes are designed and their fabrication optimized. These membranes allow for a five-fold increase in flow rate while maintaining the same shear-stress conditions. Next, a programmable confocal microscope routine is implemented to facilitate scalable data acquisition. Finally, we demonstrated the applicability of the improved platform in isolating CTCs from CRCLM patients. scCTCs and cCTCs were found in 13/13 patients. To the best

of our knowledge, this is an unprecedented cCTC-positive rate (100%) in a set of CRCLM samples. This finding suggests that cCTC counts might be under-reported in literature due to the common use of CTC enrichment technologies that are incompatible with cCTC isolation or have low cCTC sensitivity. The outcome of this work improves the throughput of the G μ F platform, which will facilitate its use in the pursuit of clinical translation research. Future studies are likely to investigate the particular role of cCTCs in the metastatic cascade, and assess their value as liquid analytes for cancer diagnosis, prognosis, and monitoring.

Résumé

À travers le monde, le cancer est une des principales cause de décès, et les lésions causées par les métastases sont la cause première des complications mortelles reliées aux tumeurs cancéreuses solides. La caractérisation des tumeurs par biopsie est un processus invasif qui ne tient pas compte de l'hétérogénéité spatio-temporelle, étant donné que les analyses sont faites sur une quantité limités de tissus prélevés à une seul moment et à un seul endroit. Les biopsies sont souvent présent lors de résections chirurgicales; cela prive les patients de traitements bonifiés par une meilleur compréhension du phénotype des tumeurs. Pire encore, cela place les patients face à des traitements couteux, qui peuvent même s'avérer nuisibles et inutiles. Cela est vrai des métastases hépatiques liées au cancer colorectal (CRCLM; colorectal cancer liver metastasis): au Canada, les patients reçoivent du bevacizumab pré-opératoires, ce qui empire le résultat croissance histologique (HGP; histological growth pattern) qui est seulement diagnostiqué après la chirurgie.

Les cellules de tumeur en circulation (CTC; *circulating tumour cells*) dans le sang ont une importance clinique elles sont utilisées pour diagnostiquer et mesurer la progression un grand nombre de cancer. Ces cellules de tumeurs en circulation dans le sang sont beaucoup plus rarement trouvé en forme de regroupement (cCTCs; *circulating tumour cell clusters*): ce format augmente le potentiel métastatique et on peut y retrouver des tumeurs stromals et des cellules immunes. Par contre, la plupart des techniques d'isolation des cCTCs communément utilisées servent à isoler des cellules uniques, et non à capter plusieurs cCTCs. Le Juncker Lab a développé une plateforme de microfiltration basé sur la gravité (G μ F; *gravity microfiltration*) en mesure d'isoler des cellules uniques et des regroupements de CTC à partir d'échantillons sanguins sur le base de leur grosseur et de leurs propriétés mécaniques. Cette plateforme a démontré une excellente efficacité de capture des tests d'inoculation et nous amène vers des découvertes excitantes de cCTCs chez les patients atteints de cancer ovarien. Cependant, des obstacles au niveau des échantillons et du débit des analyses doivent être surmontés afin de pleinement profiter des forces et avantages de la plateforme dans un

contexte d'étude de grande échelle.

La recherche effectuée a pour but d'accroître l'évolutivité de la plateforme $G_{\mu}F$. En premier lieu, des membranes haute porosité ont été conçues et leur fabrication a été optimisée. Ces membranes permettent d'accroître par cinq fois la capacité de débit tout en maintenant les mêmes conditions de cisaillement. Ensuite, une routine programmable de microscopie confocale est mise en œuvre pour faciliter l'acquisition de données évolutives. Enfin, nous avons démontré l'applicabilité de la plateforme améliorée pour isoler les CTCs de patients atteints de CRCLM. Des scCTCs et des cCTCs ont été trouvés chez 13/13 patients. À notre connaissance, il s'agit d'un taux sans précédent de cCTC-positifs (100%) dans un ensemble d'échantillons CRCLM. Ce résultat suggère que le nombre de cCTC pourrait être sous-estimé dans la littérature en raison de l'utilisation courante de technologies d'enrichissement des cCTC qui sont incompatibles avec l'isolement des cCTC ou qui ont une faible sensibilité aux cCTC. Le résultat de ce travail améliore le débit de la plateforme $G_{\mu}F$, ce qui facilitera son utilisation dans la poursuite de la recherche translationnelle clinique. Les études futures porteront probablement sur le rôle particulier des cCTC dans la cascade métastatique, et sur l'évaluation de leur valeur en tant qu'analytes liquides pour le diagnostic, le pronostic et le suivi du cancer.

1 Introduction and Thesis Objectives

Title: Gravity-Driven Microfiltration for Enriching Circulating Tumour Cells and Clusters

1.1 Introduction

Metastasis, the spread of tumour cells from the primary tumour to distal secondary sites, is the leading cause of mortality in patients with epithelial cancers[1]. Studying the process by which metastases arise, known the metastatic cascade, is valuable to our understanding and treatment of the disease. Circulating tumour cells (CTCs), shed from a tumour into the bloodstream, represent a critical intermediary in the metastatic cascade and have become a target of interest as predictive and prognostic markers[2]. Quantity of CTCs found in blood samples has been correlated with poor outcome, recurrence, and resistance to treatment[3, 4].

In order to study CTCs we must first isolate them. However, the properties of CTCs make them challenging to isolate: they are extremely rare ($\sim 1-100$ CTCs vs 1×10^6 leukocytes and 1×10^9 erythrocytes per ml of blood) and present a high degree of morphological and molecular heterogeneity[5, 6]. An additional complication is the existence of multicell CTC clusters (cCTCs), which can contain tumour-associated immune and stromal cells. cCTCs have demonstrated an increased metastatic potential over scCTCs and thus represent a subpopulation of high clinical relevance[7, 8]. Isolating clusters presents unique challenges due to their additional dimensions of heterogeneity and tendency to break up under shear stress during routine blood processing steps, such as centrifugation.

The Juncker Lab has developed a gravity-driven microfiltration platform (G μ F platform) suitable for the enrichment of single cell CTCs and CTC clusters from blood samples[9]. The platform uses polymer membranes fabricated by a vacuum assisted UV micro-molding (VAUM) process developed in collaboration with, and fabricated at Teodor Veres's lab at National Research Council (NRC) Canada[10]. The filter captures cells based on their size

and deformability, and can be functionalized with antibodies to provide combined molecular and mechanical capture. A gentle, gravity-driven flow regime limits the shear stress placed on captured objects, preserving delicate cCTCs. Captured cells are fixed and stained on-filter and analysed by fluorescence microscopy. Staining allows the differentiation between CTCs (DNA+/CK+/CD45-) and leukocytes (DNA+/CK-/CD45+). The platform has been shown to capture scCTCs and cCTCs with high efficiency in spike-in experiments, and has been used to study CTCs in clinical samples from ovarian cancer patients in collaboration with Dr. Anne-Marie Mes-Masson at the Centre Hospitalier de l'Université de Montréal (CHUM)[11].

The throughput of Juncker Lab's CTC platform is limited by bottlenecks in three key areas. (1) The system filtration rate (0.1 ml/min), which is limited by the membrane porosity and diameter of the polymer microfilters. (2) Fluorescence imaging is manual and time consuming; acquisition of a pair of filters takes hours of operator time. (3) The quantification and analysis of the image data is also done by hand. In addition to being extremely labour-intensive, manual image acquisition and analysis can be subject to inter and intra operator variability. Addressing any of these bottlenecks would increase the scalability overall efficacy of the CTC filtration platform and facilitate its use in further clinical research, which could lead to valuable developments in our understanding of CTC biology and their use in cancer diagnosis, prognosis, and monitoring.

1.2 Thesis Objectives

The goal of this thesis was to increase the throughput of the G μ F CTC enrichment platform so make it more suitable for research at scale. This was accomplished through technology development targeting two of the three identified bottlenecks: filtration rate and image acquisition. Afterwards, the enhanced platform was used to isolate CTCs from clinical blood samples obtained from colorectal cancer patients.

1.2.1 Aim 1: Fabrication of High-Throughput Polymer Microfilters

First, polymer microfilters with porosity and diameter were developed. A new photomask was designed and used to produce master molds for use in VAUM. The VAUM protocol was adapted and optimized to overcome challenges encountered from producing high area, high porosity membranes outside of a cleanroom. This allows the in-house production of large filters, or batches of conventional-sized filters from a single mold.

1.2.2 Aim 2: Automated Image Acquisition

Second, a programmable microscope routine was developed to automate imaging the filters. This was implemented using modules in the software of our confocal microscope. The skeleton for the workflow is as follows: (1) user sets their desired imaging parameters (objective, laser power, z stack, etc.), executes the program, and is free to go; (2) a low-magnification brightfield image is taken in order to calculate the bounds of the filter; (3) a multipoint confocal scan is performed within the calculated area. The result is scalable image acquisition in which active time is limited to setting up parameters and is independent of filter size. It carries additional benefits of increasing the replicability and reducing the operator bias of the microscopy.

1.2.3 Aim 3: Clinical Study of cCTC Incidence in CRCLM

Lastly, incorporating the technology developments in Aim 1 and Aim 2, the enhanced G μ F platform was used to investigate the incidence of scCTCs and cCTCs in a sample of colorectal cancer liver metastasis (CRCLM) patients. This was done in follow up to previous work with the G μ F platform that found higher than expected prevalence of clusters in endothelial ovarian cancer (EOC) patients[11]. Blood samples were collected in collaboration with Peter Metrakos' lab and clinics at the MUHC and processed and fixed on site using G μ F . The filters were stained and imaged at McGill and analysis was performed manually.

2 Background Information

2.1 Rationale for Liquid Biopsy

Cancer is a leading cause of premature death worldwide[12]. According to the GLOBOCAN 2020 estimates, there were 18 million new cases of and 9.2 million deaths from solid-tumour cancers in 2020 alone[13]. Metastases are by far the most commonly cited source of death within these cancers [14, 1, 15]. Beyond simply the burden of an additional tumour, metastatic lesions may develop resistance to a previously effective therapy and exhibit molecularly distinct characteristics from the primary tumour[16]. Tumour characterisation is an important resource in informing therapeutic strategies.

Characterisation of patient tumours is frequently assessed from tissue biopsy of a single primary or metastatic lesion[17]. However, tumours are known to be highly heterogeneous in phenotype over many dimensions: spatially within a single lesion, between primary and metastatic sites, and within the same tumour over time[18, 19]. The high degree of tumour variability creates a representation issue when biopsying only a fraction of a single tumour. Although it would improve representation, biopsying multiple areas and lesions over time is often undesirable due to the invasiveness of the procedure, especially for tumours in difficult to access locations such with glioblastoma[20]. Thus, biopsy is frequently only taken during surgical resection and tumour characterisation happens only after its resection[21], presenting no opportunity for personalized treatment based on tumour phenotyping before the surgery. This may be improved by liquid biopsy, which is the enrichment and analysis of tumour-derived analytes from bodily fluids (most commonly blood), is minimally invasive and enables timecourse sampling of multiple tumour sites. Tumour material of ranging complexity can be detected in blood: circulating biomarkers, tumour derived extracellular vesicles, and entire cancer cells. In general, more complex targets, such as cells, provide richer data, but are rarer and more challenging to isolate.

Circulating Biomolecules Freely circulating DNA, proteins, and metabolites are the smallest and most simple tumour products detectable in blood. Prospective candidate markers are typically identified by high throughput screening of a smaller number of samples and then validated in larger studies using lower-cost targeted tests. Candidate genetic biomarker screening employs high-throughput microarrays before seeking to validate the hits in larger PCR studies which compare the relative expression of the markers in patients vs healthy controls[22]. In addition to loci expression, chromosomal aberrations (*e.g.*, single nucleotide polymorphisms, copy number loss/variation) can be assessed by cytogenetic analyses[23, 24]. Protein and metabolic biomarkers screening is commonly done with nuclear magnetic or mass spectroscopy[25, 26]. Once identified, these biomarkers can be routinely measured using methods such as ELISA, as is routine with CA125 in ovarian cancer[27, 28]. Circulating biomarkers generally have a short half-life, are quickly renewed and do not require any of the pre-analysis enrichment beyond blood fractionation necessary of more complex targets[21]. However, because the origin and relationship between individual molecules is unknown, they provide no means of identifying subpopulations or otherwise evaluating tumour heterogeneity. Each biomarker could have originated from any number of different cells, tumour areas, or tumour sites. Furthermore they have limited potential for functional studies compared to extracellular vesicles and cells.

Extracellular Vesicles Colocalized tumour material of same-cell origin can be found in extracellular vesicles (EVs). EVs are small secreted membrane vesicles containing functional biomolecules (proteins, lipids, DNA, and RNA) that can be horizontally transferred to recipient cells[29]. They have roles in intercellular communication and it has been demonstrated that some EVs have targeted destinations and fuse in a tissue-specific manner[30]. EVs are commonly enriched from serum based on their size (*e.g.*, using gradient density centrifugation or size-exclusion chromatography). Once isolated, the abundant contents of EVs may be analysed in aggregate or at a single vesicle resolution[31]. Aggregate

analyses include conventional biomarker analysis following bulk lysis and immunoassays on small aggregates captured by antibody microarrays or beads[32, 33]. Single EV resolution analysis is predominantly reliant on the use of specialized flow cytometers (*e.g.*, Micro Flow Cytometer[34]) due to their small size (standard cytometers have a limit of detection in the range of 300–500 nm)[35], but recently some unique microfluidic platforms have been reported, such as the interferometric-based ExoView chip[36]. EVs can provide richer data in comparison to freely circulating biomarkers. (1) The relative abundance of RNA allows the study and monitoring of non-coding gene regulatory elements such as micro RNAs (miRNAs)[37, 38]. (2) Heterogeneity and subpopulations can be characterised using single-EV analysis methods. (3) They can be used in functional studies *in vitro* and in animal models[39, 40]. EVs are proposed to have a more direct role in the metastatic cascade (*e.g.*, organotropic preparation of premetastatic niches[41, 42]) compared to freely circulating biomarkers, and are thus, in addition to their prospects as cancer biomarkers, an interesting target from a fundamental oncology research standpoint in (how carcinogenesis develops vs simply detection and monitoring). In 2015, Hoshino et al. identified subpopulations of cancer cell line derived EVs with distinct integrin expression profiles that preferentially target different tissues in a mouse model[43]. Furthermore, these EVs were sufficient to induce organotropic metastasis in xenograft tumour cells that otherwise do not metastasize to a specific organ.

Cells Moving up in size and complexity, circulating tumour cells (CTCs) are extremely rare in blood (1–100 CTCs/ml vs 1×10^6 leukocytes and 1×10^9 erythrocytes) and present high physical and molecular heterogeneity[5, 6]. They present unique challenges in their isolation compared to EVs and circulating biomarkers, but have enormous potential in the richness of data they can provide for analysis: from genomics and proteomics, to morphological analysis and functional *in vitro/in vivo* assays. Furthermore, individual circulating cells do not always travel alone: clusters of circulating tumour cells (cCTCs) with or without any associated

immune and stromal cells can uniquely provide insights about cell interactions within their tumour of origin.

2.2 History of Circulating Tumour Cell Clusters

CTCs were first described in 1869 by Australian physician Tomas Ashworth who reported cells with similar morphology to those of the primary tumour in the blood of a patient[44]. The role of CTC clusters (cCTCs) in metastasis was first highlighted in 1954 when Satoru Watanabe demonstrated that clusters of bronchogenic carcinoma cells injected intravenously into mice more readily formed metastases than individual cells[45]. In the following 25 years studies established a correlation between the size, number of cells, and concentration of cCTCs with their metastatic potential in animal models[46, 47].

Despite the evidence from early studies linking cCTCs to the metastatic cascade, there followed a period in which subsequent research into CTCs largely overlooked clusters. One explanation for this is that early CTC enrichment technologies could not distinguish cCTCs from single cells or may even disassociate some cCTCs with high-shear steps such as centrifugation[48]. It is only recently that isolation technologies specifically targeting clusters have been developed and an understanding of the role of cCTCs in the metastatic cascade begin to emerge.

In 2004 CellSearch became the first FDA-approved CTC enrichment technology, marking the start of CTCs being used as a diagnostic analyte in the clinic for the general public. In 2007 the Toner group reported the first immunocapture microfluidic device to capture CTCs from peripheral blood[49]. The CTC-Chip was cleanroom fabricated out of silicon using photolithography and utilized EpCAM antibody-microposts to selectively trap EpCAM+ CTCs. In 2015, 13 years later the same group published the first microfluidic device specifically designed for the isolation of CTC clusters[48]. The Cluster-Chip was made using soft lithography out of poly(dimethylsiloxane) (PDMS) cast from a silicon mold and utilized sets of triangular microposts for label-free capture of two or more cell clusters.

Yet in the short time dedicated isolation technologies have been on the scene, cCTCs have been detected in a range of cancers. Their presence has been associated with worse outcome in patients with lung, breast, prostate, and ovarian cancer[50, 51, 52, 53]. Surprisingly, given the rarity of extracranial metastasis (<2%) found in disease, recent studies have even detected scCTCs and cCTCs in glioblastoma (GBM) patients[54, 55]. The rarity of metastasis outside the brain in GBM has been attributed to the short survival of GBM patients providing insufficient time for extracranial lesions to form and differences between the blood-brain barrier and capillaries of normal vasculature[56]. Thus, CTCs may still provide a valuable prognostic and diagnostic tool in these patients.

2.3 Biology of Circulating Tumour Cell Clusters

CTCs are shed from a tumour into the bloodstream where they are thought to migrate to distal tissues with the ability to implant, proliferate, and give rise to secondary metastases[2]. They are proxies for their tumour of origin and represent an important intermediary of the metastatic cascade. As intermediaries of the metastatic cascade, CTCs are a particularly important subpopulation of tumour cells with increased metastatic potential. Interest in CTCs as predictive and prognostic oncology markers has increased in recent decades following technological advancements allowing for their isolation, quantification, and phenotyping[57].

There is consensus that CTC clusters are bulk detachments, or collective dissemination, from the tumour, not aggregations or proliferations of scCTCs in blood[58, 59], and can form heterotypic clusters through interaction with tumour-associated stromal and immune cells (Figure 1)[60, 61]. Clusters are thought to have higher survivability and metastatic potential compared to scCTCs which makes them an especially relevant subpopulation for understanding metastasis. cCTCs are held together by cell-cell adhesion interactions and can travel through narrow capillaries as a single file of attached cells due to their deformability, allowing cCTCs to migrate to distant tissues[62].

Interaction with normal circulating cells can support scCTC and cCTC migration and

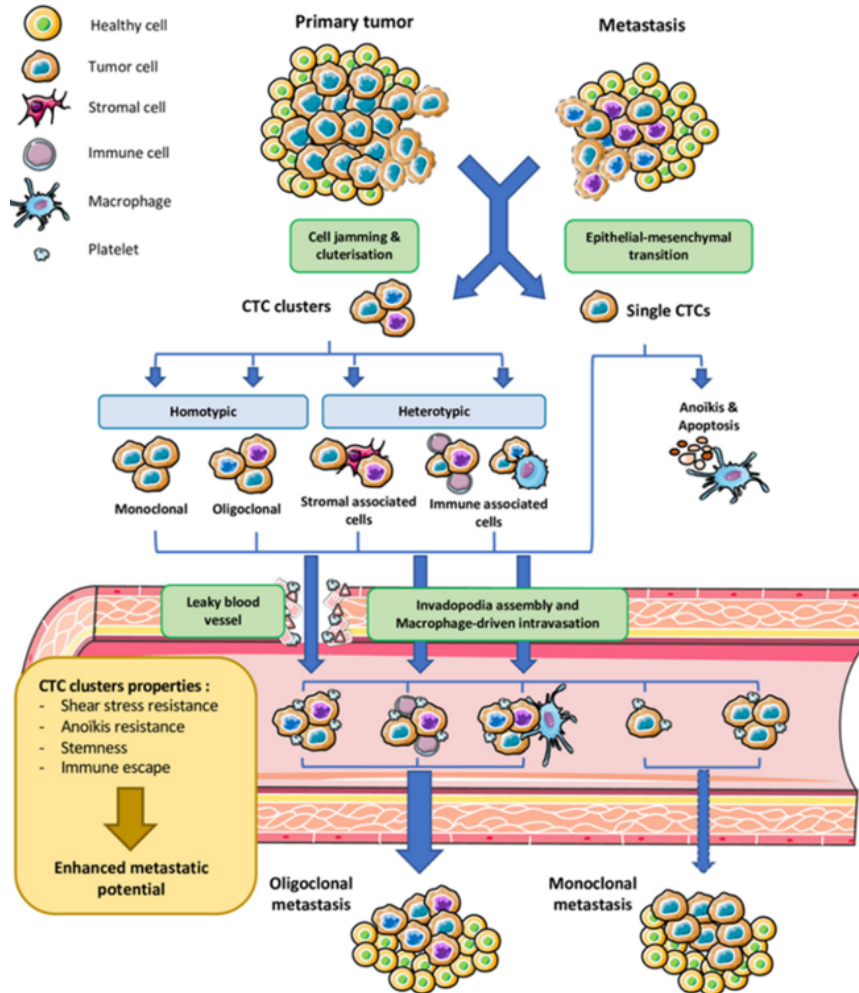


Figure 1: Overview of circulating tumour cell clusters (cCTCs) origin, composition, and dissemination. CTCs detach in bulk from the tumour site as homotypic clusters. These cells can also form heterotypic clusters through interactions with stromal and immune cells in the peri-tumoural infiltrate. Intravasation may be lead by invadopodia or macrophages, or occurs through the abnormal vasculature of the tumour microenvironment. The protective effects of clustering enhances the survivability in circulation, and thus metastatic potential, of cCTCs compared to solo CTCs. After extravasation from the blood stream, cCTCs can form metastases in distant tissues. Reproduced from[62] under CC BY 4.0.

invasion[63]. Macrophages can undergo cell fusion into hybrid CTCs[64, 65], which have been shown to have increased invasiveness in GBM models[66]. CTCs can interact with neutrophils to form tight junctions which promote metastasis, and neutrophil extracellular traps (NETs) can promote the extravasation of CTCs[67]. In addition, clusters can independently facilitate intra/extravasation by the formation of specialized cytoskeleton protrusions from the plasma membrane called invadopodia[68].

Due to maintaining close interactions with stromal and other tumour cells, CTCs in clusters exhibit different molecular features compared to their single cell counterparts. cCTCs more highly express tight junction and desmosome proteins such as plakoglobin. and plakoglobin inhibition decreased cluster formation, but not scCTCs, in metastatic breast cancer models[69, 70] Clinically, plakoglobin expression in cCTCs has been found to be an independent prognostic factor in breast cancer patients[71]. Clusters can show increased stemness through the upregulation of the cancer stem cell (CSC) marker CD44[72]. It is thought that clustering forms a favorable niche for CSCs[62]. There is evidence that cCTCs confer survival advantages and immune escape. In vitro breast cancer cCTCs overexpress Bcl2 (anti-apoptotic, anoikis resistance) and have a higher proportion of KI67+ (proliferation) cells[73, 74]. Immune escape may be facilitated in cCTCs by downregulation of type II interferon (IFN-gamma), TNF signalling, and MHC II and T-cell activation genes, and upregulation of the immune inhibitor CD24.

2.4 Isolation of CTC Clusters

The operational definition of CTCs is fluid within the literature, but the common core is that a CTC is a nucleated cell that is positive for one or more CTC marker and negative for the leukocyte marker CD45[6, 75, 4]. CTCs were traditionally isolated and identified based on the expression of the epithelial markers EpCAM and CK, but consensus that CTCs undergo epithelial-mesenchymal transition (EMT), which leads to downregulation of epithelial markers, has expanded the definition to include mesenchymal markers such as

Vimentin and Plastin1[76, 17, 77]. Following enrichment, fluorescence staining is commonly used to identify CTCs (*e.g.*, DNA+/EpCAM+/CD45-) and distinguish them from WBCs (*e.g.*, DNA+/EpCAM-/CD45+). Cell diameter has a wide range that overlaps with WBCs and WBC contamination is a common problem in mechanical capture methods. WBCs are more deformable than CTCs and this property is exploitable to decrease WBC contamination[57].

Enrichment of CTCs may be based off of targeting one, or a combination, of molecular or mechanical features that distinguish them from other cells found in blood. Molecular capture methods commonly target CD45 to deplete WBCs and/or EpCAM to enrich CTCs[57]. The most well-known molecular enrichment platform is the FDA-approved CellSearch (Veridex), which uses antibody coated magnetic beads to first deplete WBCs (anti CD45, negative enrichment) and then pull up CTCs (anti EpCAM, positive enrichment) into a cartridge for staining and fluorescence readout for identification and qualification[78]. Mechanical capture exploits differences features such as size, morphology, deformability, and density to separate CTCs from other cells present in blood in an epitope-independent manner. These are primarily gradient centrifugations or microfluidic devices utilizing filtration and/or inertia-based particle separation. Molecular and mechanical capture may be combined in order to enhance CTC capture or target epitope-expressing subpopulations. This can be done by using one discrete technology as a pre-enrichment step for another (*e.g.*, [79, 55]), or by integrating molecular and mechanical based capture into a single capture technology (*e.g.*, [80, 9]).

In all cases, the method used will bias the population of CTCs that are enriched. Antibody-based molecular capture is epitope-dependant and will miss any CTCs that have low expression of the specific markers targeted and mechanical methods will miss CTCs that are outside of the critical dimensions the device has been optimized for. Even in epitope-independent capture, reliance on immunofluorescence for identifying positive CTCs introduces another bias. CTC heterogeneity makes it difficult to cover the full spectrum

and the presence of clusters adds a further complication. cCTCs have a larger size range than scCTCs and can be heterogeneous in cell expression and cell composition, including non-CTC stromal cells. Enrichment epitopes within the cluster can be concealed by epitope negative CTCs or stromal cells, and the presence of ECM interactions and non-CTCs can affect deformability[62]. cCTCs will break up into scCTCs under high shear stress, making some methods incompatible with capturing cCTCs.

2.4.1 Cluster-Specific Isolation Technologies

Initial CTC isolation technologies were developed for isolating single cells, often including shear-inducing centrifugation steps, and studies utilizing them rarely, if at all, reported cCTCs[57, 62]. The occasional capture of cCTCs lead to efforts directed at specifically isolating clusters. A pioneering cCTC isolation method from Toner and colleagues is the Cluster-chip, a filtration-based microfluidic chip consisting of 4000 parallel $12 \times 100 \mu\text{m}^2$ slit openings designed to capture cCTCs while allowing scCTCs to pass through[49]. The group has since developed several microfluidic devices for cluster capture including a two stage deterministic lateral displacement (DLD) device that first removes large ($>30 \mu\text{m}$ diameter) clusters based on size and then isolates any remaining clusters from scCTCs and blood cells based off of their asymmetry[81]. Each stage contains an array of micropillars with geometry designed to deflect the particle of interest ($>30 \mu\text{m}$ and asymmetric particles, respectively) into a collection channel. Parsortix (Angle PLC) is a microfluidic size-based CTC filtration method capable of capturing and releasing single cells and clusters that utilizes a disposable chip with parallel channels with step gradient closing the channel width to a critical gap of 10 to $4.5 \mu\text{m}$ [75]. Cells can be stained and analysed on-device or released as viable cells can be released by backflow. Parsortix has been used as a pre-enrichment step for automated single cell seeding technology such as the VyCAP puncher. Parsortix cassettes with a $6.5 \mu\text{m}$ critical gap were used by Krol et al. in the first study to isolate CTC clusters in GBM[55].

Successful cCTC capture methods tend to favour mechanical capture and gentle

treatment of the cells. Limiting shear in a microfluidic chip typically necessitates slow flow rates and either low sample volumes or long processing times. Angle states that a typical flow rate for Parsortix is 5 ml/h (0.083 ml/min) and Krol et al. used 1.2 ml/h (0.020 ml/min) in their GBM study[75, 55]. Smaller sample volumes decrease the number of these rare cells, and even rarer clusters, captured, and long processing times diminishes the viability of isolated cells[82]. Device clogging is a common problem faced by microfluidic methods[57] that is especially relevant to cCTCs. As geometric features become blocked by cells, clusters, or other debris the remaining sample volume must travel through a progressively smaller area. In a pressure-driven system, as is ubiquitous in pump-based microfluidics, this increases fluid velocity which increases the amount of shear experienced by objects in the device. This risks breaking up clusters if the shear exceeds the strength of the extracellular interactions holding them together[62], or, in the case of a partial obstruction, breaking up clusters trapped in the device. In filtration devices some degree of channel obstruction is unavoidable, since they by design trap objects on device. To avoid cluster breakup, a pressure-driven filtration system with at fixed flow rate must be set below the theoretical maximum that avoids breakup in order to account for increasing shear as objects become captured in the device.

2.4.2 Gravity Driven Microfiltration

Microfiltration membranes can accommodate a high density of pores, each forming a parallel flow path with low shear stress relative to a microfluidic chip with the same system flow rate. The first report of CTC isolation by microfiltration was in 1964[83] using track-etched membranes which, by modern standards, have an impractically low throughput due to their limited porosity (<5%)[84]. Advances in microfabrication have allowed the manufacture of high porosity membranes with regular pore distribution that facilitate higher flow rates while maintaining low shear, significantly increasing throughput[10, 85]. Gravity-based microfiltration avoids the problem of increased pressure and shear from filter clogging because it provides a constant pressure condition given a constant fluid column height[86]. As pores

clog and reduce the number of open flow paths, the flow rate of a gravity-driven filter will decrease while maintaining pressure. This is in contrast to a pump-driven system, which supplies a constant flow rate, where increased clogging results in increased pressure in the remaining flow paths.

We previously developed a gravity-based microfiltration (G μ F) platform that allows for the epitope-independent isolation of both single CTCs and CTC clusters from blood (Figure 2). The system is an iteration based on a previous system that was pump-driven[9]. It utilizes 8 mm diameter polymer microfilters inside a 3D printed cartridge combined with off the shelf fluidic components. The microfilters are fabricated in-house by a vacuum-assisted micromolding (VAUM) process which produces transparent, non-autofluorescent, high open-ratio membranes with specific pore diameter and distribution[10]. Immunofluorescence can be performed directly on the membrane due to its favourable optical properties, or captured cells can be released by backflow for cell culture and other downstream analysis. An arbitrary number of filters with different pore diameters may be stacked sequentially through the use of printed adapters to fractionalize captured cells. This affords a degree of setup modularity; the system has been tested in configurations from a single filter to 6 filters in a serial gradient with pores from 28 to 8 μ m.

Previous work optimized a stack of 15 and 8 μ m pore diameter filters (19.6 and 8% porosity) to filter blood diluted 1:6 with PBS at a flow rate of 0.1 ml/min and found this setup to capture spiked OV-90 cells at an efficiency of 86% for single cells and 84% for clusters[11]. Compared pump-driven flow, G μ F was found to be more efficient at capturing cCTCs with an 8 μ m pore filter (80% vs 35% at 0.1 ml/min) while maintaining the same efficiency for scCTCs. Increasing flow rate decreased cCTC capture and increased scCTC capture efficiency above 100% in both flow regimes, consistent with cluster break up due to increased shear. Release efficiency of clusters from the 15 μ m filter at 0.1 ml/min was 83% with 75% viability and there was no difference in mean cluster size before capture and after release. The viability of released clusters was independent to the different release

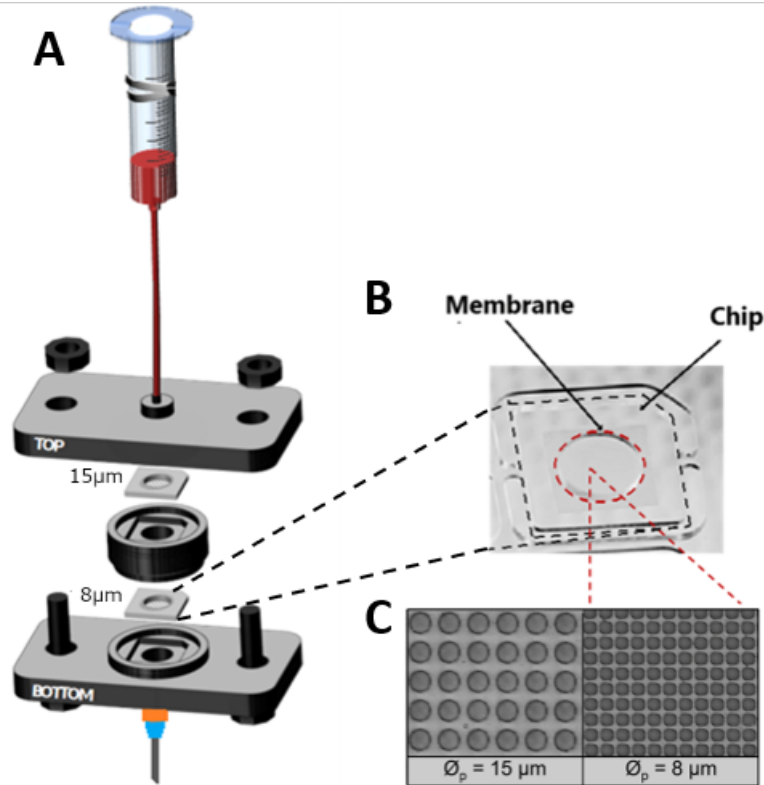


Figure 2: Schematic of the gravity microfiltration (G μ F) platform for CTC isolation. (A) Apparatus assembly in a two filter (15 μ m over 8 μ m) configuration. A 3D printed cartridge encloses the two filter chips which are separated by a 3D printed adapter. A 50 ml syringe is connected to the cartridge inlet and a dispensing needle to the outlet. Polymer membranes bonded on plastic chips (B) contain regularly spaced pores of specific diameter (C). Membranes shown are the 40% porosity variety developed during this thesis.

media (PBS, FBS, OSE media) and temperatures (4°C, 20°C, 37°C) tested, unlike scCTC viability which varied across conditions and was only equal to cCTCs at 4°C in PBS. This highlights the increased survivability of cCTCs which, in addition to their metastatic potential, is relevant to downstream applications depending on live cells, such as cell culture and secretomics.

The G μ F platform has been used to isolate cCTCs from clinical endothelial ovarian cancer (EOC) blood samples[11]. cCTCs were found in all 3 ml samples tested: high grade serous cystadenocarcinoma (HGSC) chemo treated (n=4) and naive (n=1), and chemo-naive patients of other EOC histological subtype (n=5). In chemo HGSC samples, a low proportion of cCTC capture events and higher proportion of small (2- and 3-cell) clusters was correlated with low CA125, an index of good chemotherapy response. The timecourse study of a single HGSC patient with good chemotherapy response showed a differential reduction of cCTC scCTC counts, and a decrease in the size of cCTCs over treatment (Figure 3).

2.5 Limitations of the G μ F Platform

Our G μ F platform is an exciting prospect for the study of CTC clusters. An initial study using the tool found cCTCs in 10/10 EOC patients, which suggests a higher prevalence of cCTCs general literature, which could be attributed to its gentle sample handling[11]. However, the sample size of 10 is too low to be confident in this claim. A broader study containing more samples and types of cancers is needed.

The most glaring limitations imposed by the G μ F platform to the broad study of clinical samples are in its throughput. These can be broken down into three areas: fluidic, imaging, and image analysis. Although it has a satisfactory overall capacity (*e.g.*, the device can handle the CellSearch-induced standard of 7.5 ml without completely clogging), the necessitated 1:6 dilution of whole blood and maximum flow rate of 0.1 ml/min results in unfavorable scaling of runtime with volume (*e.g.*, over 8.75 hours for 7.5 ml whole blood). Typically the platform is used with 3 ml of whole blood (21 ml after dilution) and filtration takes between 3.5 and

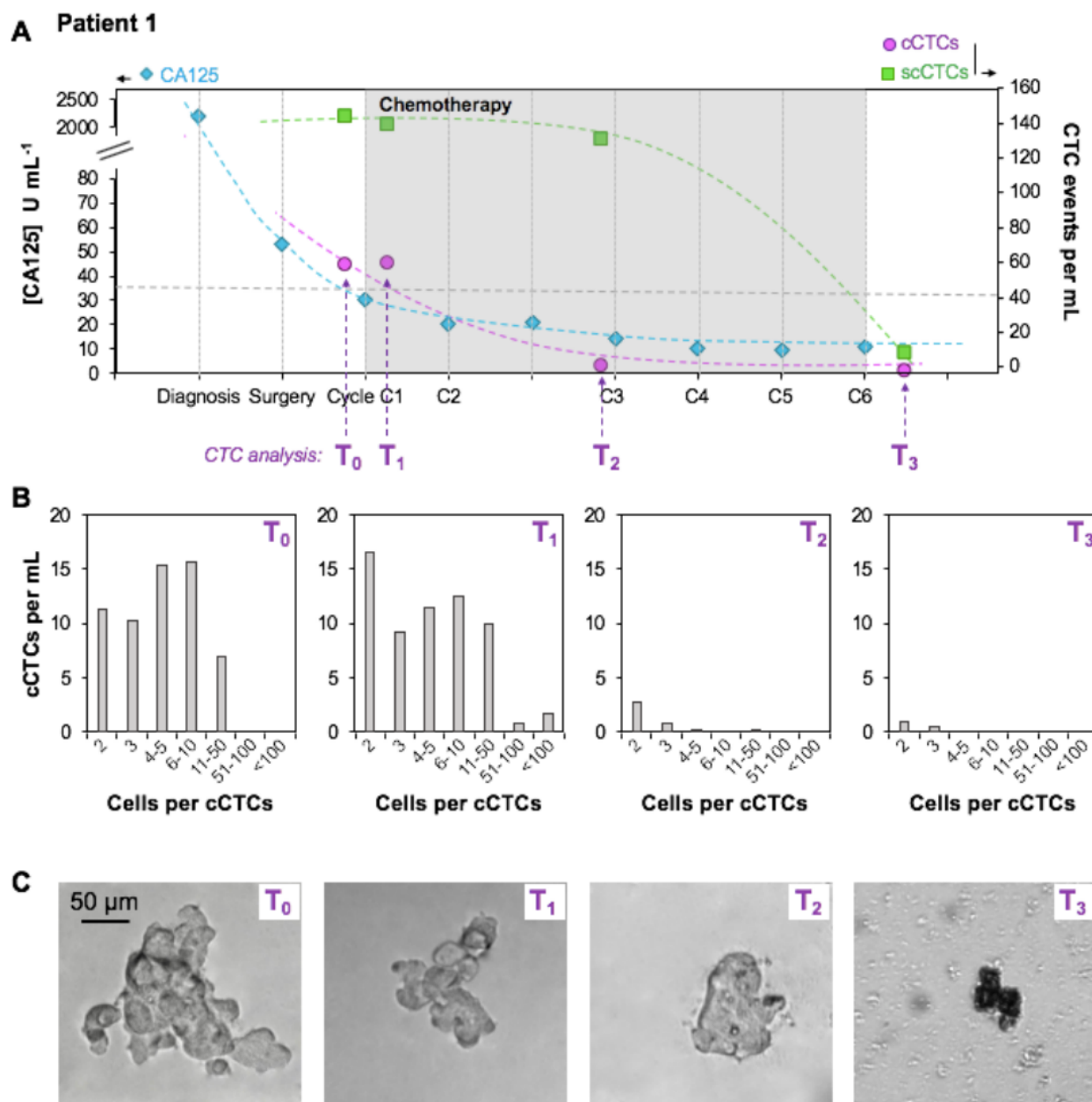


Figure 3: Time-course study for one metastatic HGSC patient[11]. (A) Time course study for P1 who responded to therapy, showing the CA125 concentration as well as the number of scCTC and cCTC events per ml of blood at different time points during chemotherapy. (B) cCTCs size distribution and (C) representative brightfield images of cCTCs captured from the blood of the patient at four time points.

4 hours, exclusive of any post-filtration steps. There are several advantages to increasing fluidic throughput beyond facilitating direct comparison to CellSearch: processing larger volumes of blood should provide a more complete sample of tumour heterogeneity; in the case of releasing cells, decreasing processing the same amount of blood faster should improve viability; and faster processing times improve convenience of the technology and quality of life of the researchers using it. Increasing the system's flow rate must be done with care to preserve the low shear that allows it to capture cCTCs so effectively. The most viable methods for doing so in this manner are (1) increasing the porosity of the filters (more channels in the same amount of space), and/or (2) increasing the overall area of the filter (more parallel microchannels).

Enumeration of CTCs captured by the G μ F platform is done through immunofluorescence microscopy. When done manually, this process is laborious. Anecdotally, the typical acquisition rate for 3-channel imaging is between 1 and 2 hours per filter (3 to 4 hours for a typical two filter sample). This is all active time, requiring the full attention of the microscope operator. Modern microscopes are commonly completely operable from software and feature interfaces through which routines can be programmed and automated. Developing an algorithm to programmatically scan the filters will, at minimum, reduce active operator time and should increase the rate of acquisition.

Manual image analysis is the largest throughput bottleneck faced by the G μ F platform. CTCs must be distinguished from WBCs and background debris. Anecdotally, it is a typical rate of analysis is on the order of one sample per week. Not only is the work cumbersome and slow, but, due to the subjective nature of image classification, it is also highly subject to interoperator variability in terms of speed and results. Intraoperator variability is another potential pitfall; humans get tired and are liable to become less efficient and make mistakes over extended sessions of repetitive work. Using algorithms for semi or fully automated image analysis is an attractive avenue to pursue for increasing analysis throughput with the added benefit of reducing human variability.

3 Aim 1: Fabrication of High-Throughput Polymer Microfilters

Previous work has identified a gravity-driven two filter stack with 15 μm and 8 μm pore diameters as an effective system configuration for CTC capture from blood samples. A key point of this setup is that it effects low shear stress on particles trapped on the filter surface, which is important for preserving multicellular aggregates of CTCs. Controlling the maximal shear stress is equivalent to controlling the maximal flow rate through any single pore. The flow rate of the system is a function of the open area of the filters: more open area increases the flow rate which, given a fixed pore size and through-pore flow rate, is proportional to total number of pores on the filter. Increasing the system flow rate will be accomplished through increasing the size and porosity of the polymer microfilters. This will increase the total number of pores for fluid to flow through without increasing the per-pore flow rate or shear stress.

Prior to the start of the current project, the fabrication of the polymer microfilters used in the CTC platform was carried out exclusively by Alex Hernandez, the primary developer of the method, at NRC Boucherville. The facilities and equipment available at NRC Boucherville and the Juncker Lab are largely different. Moving the fabrication from NRC to McGill required the adjustment of parameters to account for variation between different pieces of equipment and adaptations in cases where comparable equipment is not available. Optimization of the fabrication protocol was performed using a mold design previously used for the CTC platform and using the NRC fabrication parameters as a starting point.

3.1 Methods

UV curable resins Ebecryl3708 UV curable resin was prepared from 7:3 mixture of Ebecryl 3708 and tripropylene glycol diacrylate (TPGDA) (Allnex Canada Inc.) with

+1% w/w Darocur 1173 (Sigma-Aldrich) as curing agent. UVA1534 UV-curable resin was prepared from a 1:1 mixture of 3,4-Epoxy cyclohexylmethyl-3,4 epoxy cyclohexanecarboxylate (Sigma-Aldrich) and CAPA 3050 (Allnex Canada Inc.) with +2% w/w UVAcure 1600 (Allnex Canada Inc.) as the curing agent. MD700 UV-curable resin was prepared from Fluorolink MD700 (Solvay Specialty Polymers USA) with +2% Darocur 1173 as the curing agent.

Polymer membrane fabrication Polymer membranes are fabricated through vacuum assisted UV micro-molding (VAUM) (Figures 4 and 5). The Ebecryl3708 and UVA1534 resins are spin-coated onto a single-side silicone-coated PET film (FRA-371, Fox River Associates USA) using a PDMS-coated wafer as a substrate prior to their use in molding steps (Figure 4-3 and 4-5). The resulting membrane is cut with a blade to size and heat-bonded to a laser-cut polymethyl methacrylate (PMMA) carrier chip to provide structural support of the thin MD700 and facilitate easy assembly into a filtration cartridge.

Master mold fabrication Two 6 inch silicon wafer master molds were designed according to the following specification (Figure 6A and 6B): two 55 mm², 30 μm deep pillar arrays spaced 60 mm apart with a post diameters of 8 μm or 15 μm and each with a 300 μm inlet at top-center. The molds differ in their porosities and arrangement of posts: square grid at $\phi=40\%$, and hexagonal grid at $\phi=50\%$. These porosities were chosen to maximize the open-ratio of the resulting membranes while maintaining enough membrane material to facilitate a reasonable fabrication yield. The 40% porosity molds represent a 5-fold and 2-fold increase in open ratio for the 8 and 15 μm pore diameters, respectively (Figure 6C and 6D), compared to the previous design ($\Phi_{8\mu m} = 8\%$, $\Phi_{15\mu m} = 19.6\%$). 55 mm² is the maximum array size to fit two arrays on a 6-inch wafer while leaving enough room for edge bead removal during photolithography.

The master molds are prepared from a 6 inch silicon wafer (University Wafer) using standard photolithography. AZ 5214E photoresist (AZ Electronic Materials) is applied

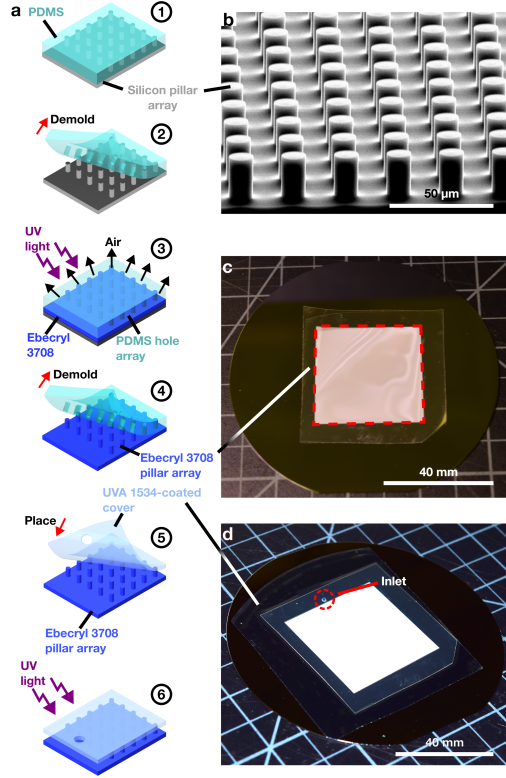


Figure 4: VAUM mold preparation and assembly. The process begins with a PDMS replication from a silicon master mold (1–2). The PDMS negative mold is silanized with Trichlorol(1H,1H,2H,2H)-perfluorooctyl-silane and from it a pillar array is replicated using Ebecryl3708 (3–4). The cover of the mold assembly is created from a film coated with partially-cured UVA1534 with a matched to the inlet of the pillar array. The cover and pillars are assembled and cured to create an enclosed mold. (b) SEM image of silicon pillar array. (c) Picture of the cured Ebecryl pillar array. (d) Picture of the enclosed mold assembly. Reproduced with premission from [10].

by spin coating following baking the wafer at 120°C for 90 s. The film is exposed to patterned UV light using a chrome-on-sodalime photomask (HTA photomask) followed by development in MIF-300 (AZ Electronic Materials). The exposed pattern is etched into the silicon substrate via deep reactive ion etching (DRIE) (Oxford Instruments PlasmaLab System 100) using Bosch processing to achieve an etch depth of either 20 μm or 30 μm. After etching, the remaining photoresist is stripped by exposure to oxygen plasma. The cleaned silicon master mold is then coated with a thin antiadhesive layer of Trichlorol(1H,1H,2H,2H)-perfluorooctyl-silane (Sigma-Aldrich) by vapor deposition in a vacuum desiccator. The photolithography and etching steps must be carried out in a

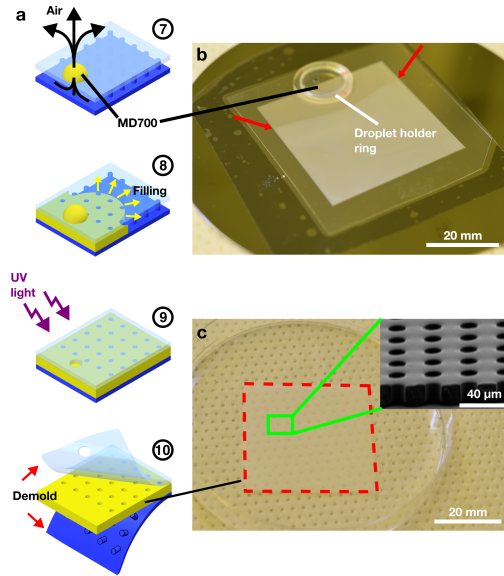


Figure 5: VAUM mold filling and demolding. A droplet of Fluorolink MD700 (UV-curable resin) is applied over the inlet. The assembled mold is placed under vacuum (7) to degas the air in the gaps between the pillars out of the inlet and re-pressurization drives the MD700 into the gaps (8). The MD700 is cured by UV (9) and the membrane is released from the mold (10). (b) Picture of the mold during the filling process. A PDMS ring is used to prevent movement of the MD700 droplet. (c) SEM image of the membrane. Reproduced with permission from [10].

cleanroom environment, but silanization and all subsequent VAUM fabrication steps can be done in a conventional laboratory.

3.2 Results

Fabrication of silicon master molds and casting holders Photomask layouts were designed in Tanner L-Edit and sent to HTA Photomask for production of the chrome-on-sodalime photomasks. Two batches of silicon master molds were made using these masks. The first batch was fabricated by Alex Hernandez at NRC Boucherville with an etch depth of 30 μm. The second batch was produced with shallower 20 μm etch depth to address demolding issues which will be described later. Photolithography was carried out at McGill Nanotools and DRIE performed by Christh e Clement at Polytechnique.

The logistics of casting PDMS from the master mold (Figure 4-1 and 4-2) proved

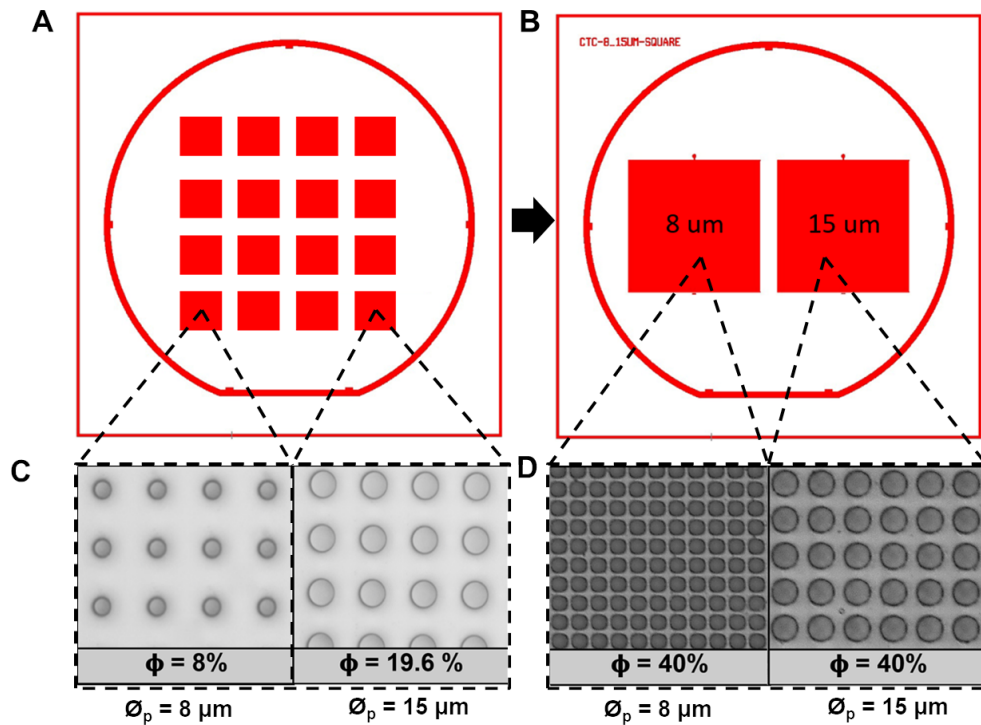


Figure 6: Comparison of previous $12\ 20\text{ mm}^2$ array layout (A) and the photomask designed in this work consisting of two 55 mm^2 arrays (B). Brightfield images of sections from the previous porosity (C) new (D) designs showcasing the increased feature density.

challenging. Typically in PDMS molding, the mold is placed in a container and covered in a 10:1 PDMS to cross-linker mix up to a height of at least 4 mm above the features. The assembly is placed under vacuum in a desiccator to remove any air bubbles in the PDMS and then allowed to cure at 60°C for at least 4 hours. The patterned PDMS is then cut out from the dish with a knife and peeled from the master mold. An ideal container for molding is one internal dimensions just larger than the master mold, external dimensions which fit inside of the desiccator to be used, is flat-bottomed, and/or sealed to the bottom of the master mold (to produce a level product and prevent PDMS under the mold). A number of solutions were attempted and abandoned. 150 mm petri dishes are too small to hold a 150 mm wafer. A 200 mm^2 bioassay dish meets the internal dimensions and flatness criteria, its large volume necessitates hours long degassing outside of the desiccator and a large initial volume of PDMS. This method also lead to the loss of one master mold which

cracked during demolding.

A wafer holder for casting PDMS was created to simplify and minimize the volume of PDMS used during the master mold replication step[87]. This is a 180x180x6 mm piece (dimensions which fit inside of a standard desiccator) of PMMA with a cutout (155 mm), just larger than the silicon wafer. The piece was cut from a sheet of PMMA using a laser cutter. A piece of adhesive Frisket Film is stuck to one end and the wafer is gently pressed into the film to seal the bottom. The PDMS is then poured, degassed, and cured. To demold the cured PDMS and master mold, the adhesive film is peeled off and the molds released by cutting around the perimeter of the PMMA circle with a scalpel. This is a cheap and clean system for casting PDMS from silicon master molds with minimal stress to the mold and polymer consumption.

Cleaning master molds by PDMS wet etching In some cases there was incomplete silanization of the silicon master mold and failed demolding where some of the cured PDMS remains stuck in silicon features. The size of the remaining PDMS ranged from thin millimeter-scale sections to large 2 cm² chunks 1 cm² thick. To clean out the master molds without damaging its features we employed a wet etching technique developed for PDMS micropatterning. Briefly, the cured PDMS is dissolved with tetrabutylammonium fluoride (TBAF) in 1-methyl-2-pyrrolidinone (NMP); TBAF etches the PDMS, but does not attack silicon, while NMP dissolves the product of the etching reaction. Although the etch rates reported in literature are quite slow (1.5 $\mu\text{m min}^{-1}$ to 5 $\mu\text{m min}^{-1}$ [88]) we found that a 1:3 75% TBAF:NMP bath with constant agitation (using a orbital shaker) was able to remove any PDMS residue from the master molds after one to five days (Figure 7). After wet etching the molds were washed with ultrapure water and resilanized.

Silanization of PDMS molds The high porosity of the membrane design results in very thin (down to 3 μm) areas of material in between pores. This makes the fabrication sensitive to any adhesion between materials tearing the thin sections during the demolding steps

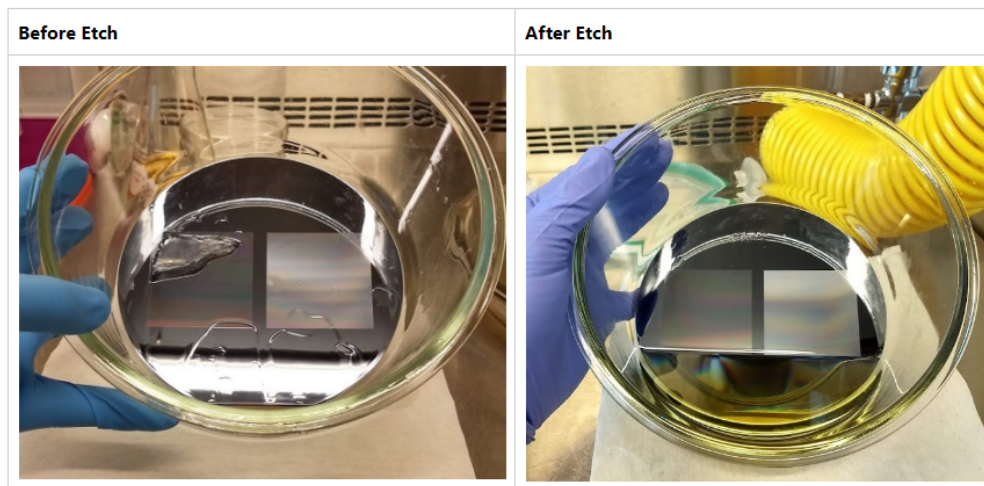


Figure 7: Cleaning PDMS from silicon mold using TBAF/NMP etching. The PDMS slab left behind during a failed demolding is visible in the top left of the leftmost pillar array in the before etch photo.

(Figures 4-2, 4-4, and 5-10). The original PDMS silanization protocol (vapor deposition without surface activation) was found to be inadequate for the new membrane design and would reliably lead to the top of PDMS features breaking off (“top-off”) and remaining in the pillar array during PDMS-ebecryl demolding (Figure 4-4). To increase the strength of silanization we experimented with different surface activation methods to oxidize the PDMS before vapor deposition. The best results were obtained from oxidizing the PDMS mold in a UV-ozone chamber with a cover to shield the PDMS from direct exposure to the UV lamp, followed by overnight silane vapor deposition. This provided adequately strong silanization (PDMS-ebecryl demolding without top-off) without introducing surface defects in, or inhibiting infilling (Figure 4-3) of the PDMS mold.

Demolding membrane from pillar array Acetone alone was not enough to achieve self-demolding of the final polymer membrane from the pillar array of its mold (Figure 5-10). We found that a short (under 1 minute) acid pre-treatment using Nano-Strip 2X (KMG) facilitated the membrane to self-demold in an acetone bath. Nano-Strip 2X (a stabilized formation of 85% sulfuric acid, 10% peroxymonosulfuric acid, and <1% hydrogen peroxide)

worked better than either pure sulfuric acid or piranha solution (sulfuric acid hydrogen peroxide). All three solutions attack the ebecryl mold material, but piranha and sulfuric acid do so more aggressively which leads to the mold tightly curling up and tearing the membrane into small pieces.

3.3 Discussion

We iterated on a previously used master mold design and can now produce membranes with 40% porosity up to 55 mm² in area. This represents a 5-fold and 2-fold increase in open-ratio of the 8 μm and 15 μm diameter pore membranes, respectively, and a 7.5-fold increase in membrane area. Membranes of this design can be used in our currently existing 3D printed cartridges at an increased flow rate while maintaining the same shear stress, due to their higher porosity, and also provide the possibility of scaling up to significantly larger area membranes should the need arise. A number of adaptations were made to the fabrication protocol to address challenges in fabrication stemming from large area of dense features: the use of a acrylic/film PDMS casting holder, UV-ozone surface activation during PDMS silanization, and Nano-Strip in the demolding process. As a silver lining to a number of failed PDMS-silicon master demoldings, we have found a wet etching method that can clean substantial PDMS top-off from the master molds.

4 Aim 2: Automated Image Acquisition

The readout of the CTC filtration platform is fluorescence microscopy. A minimum of three channels are required to identify CTC-like cells (DNA+/CK+/CD45-) and differentiate them from WBCs (DNA+/CK-/CD45+).

Image acquisition has been a bottleneck prior to the introduction of larger filters. Acquisition was done manually, with the microscope operator moving the stage and selecting which areas of the filter to image. This typically results in between 80 to 120 tricolour images

per 8 mm diameter filter, each containing one or more regions of interest (ROI) for later analysis. The time required to image a single filter was commonly in the realm of one to two hours. Manual image acquisition in this fashion is extremely time and labour-intensive, and it's drawbacks will only be exasperated by increasing filter area: presenting a major obstacle to platform scalability. In the pursuit of a scalable, high-throughput imaging solution for the G μ F platform, we developed a programmable confocal microscope routine that scans the filters.

4.1 Methods

Imaging Setup Cells are fixed on-filter in 4% paraformaldehyde (PFA) and stained with Dapi (nucleus stain), anti-CK18/AF488 (epithelial marker), and anti-CD45/AF647 (lymphocyte marker). Membranes are removed from the plastic carrier chip and placed filter face up on a glass slide. A #1.5 coverslip is mounted using a drop of Fluro-Gel (Electron Microscopy Sciences) and the edges sealed with transparent nail polish (Xtream Wear 100, Sally Hansen). A circle is drawn on the coverslip to denote the filter area for imaging. Prepared samples are stored in the dark at 4°C.

Fluorescence imaging is performed using a resonant-capable laser scanning confocal (A1R, Nikon) on an inverted microscope body (Ti2 Eclipse, Nikon). It is also equipped with a camera (Prime 95B, Photometrics) for Brightfield imaging, which is used in the routine for filter alignment. The microscope is controlled and programmed using Nikon's (NIS-Elements, Nikon) software. Multiple acquisition and analysis steps can be programmed into a single 'JOB' using the software's so-called JOBS module. The smallest number of fluorophores for enumeration of CTCs from blood is three and the setup can accommodate a maximum of five (four lasers on the A1R box plus an external 730 nm line). An objective of at least 20X is used for positive cell identification.

Acquisition Algorithm and Standard Operating Procedure Confocal microscopy allows for thin optical sectioning due to a pinhole aperture that blocks out of focus light from entering the detector. The algorithm takes advantage of this by taking a set of images at progressive Z positions (a Z-stack) to produce a 3-dimensional image of the filter without the need for selecting between focus planes. This is useful for imaging the CTC clusters targeted by the G μ F platform, as with it it may not always be possible to capture all cells in the same focus plane with a widefield microscope and obscured inner cells can be missed.

An acquisition experiment takes place in three phases: (1) parameter configuration, (2) filter alignment, and (3) automated imaging. (1) First the user defines the optical configuration and Z stack to be used for filter imaging. The optical configuration includes laser power, PMT (detector) offset and gain, and channel sequence. Multiple optical configurations can be set to obtain multiple image stacks captured under differing conditions, but only a single image stack/optical configuration is required to analyse a filter. A Z stack is a list of stage Z coordinates defined by the range (top and bottom stage positions) and step size (Z plane distance between each optical section). Once the Z stack and optical configurations are plugged in, the user executes the JOB and the remaining steps are carried out automatically. (2) Filter alignment determines filtration area to be imaged (denoted by either the carrier chip or ring drawn on the slide) and outputs the list of XY stage coordinates (multipoints or M) necessary to scan the area. This is done by capturing a stitched brightfield image of whole filter with the 4X objective, detecting the largest circle to create a binary mask, and calculating the M coordinates to approximate the mask with square frames the size of the field of view (FOV) of the optical configuration at a 5% frame overlap. Optionally, the scan area can be manually defined by drawing one or more regions on the overview image. (3) No user input is required from this point. For each defined optical configuration, at each multipoint a Z stack is captured to produce N images of [M, Z, C] dimensionality (N = optical configurations, C = channels). Multiple filters can be configured and then run in sequence, as in the typical use case for the CTC platform.

The external 730 nm laser line is connected to the confocal scan head by a different port (port 2) than the A1R-native 405/488/561/640 nm lasers (port 1). Within port 1, the channels can be acquired simultaneously (*e.g.*, [1,2,3,4]) or in a sequence of individual and/or mixed channels (*e.g.*, [1,4]>[2]>[3]). The former provides the fastest frame time, while the latter is slower (multiplying the frame time by the number of steps in the sequence), but limits spectral bleed between channels. Switching between 730 nm and the other lines requires the scanner to rotate ports and change the dichroic mirror, a process which takes about 12 seconds (24 seconds including the switch back to port 1). This is significantly slower than the millisecond intervals to move the stage between XY points and through a Z stack. As a result, the most time-efficient method for acquisitions incorporating the 730 nm line is to first scan the entire filter with port 1, then port 2, and merge the images afterwards. This method requires only a single port switch.

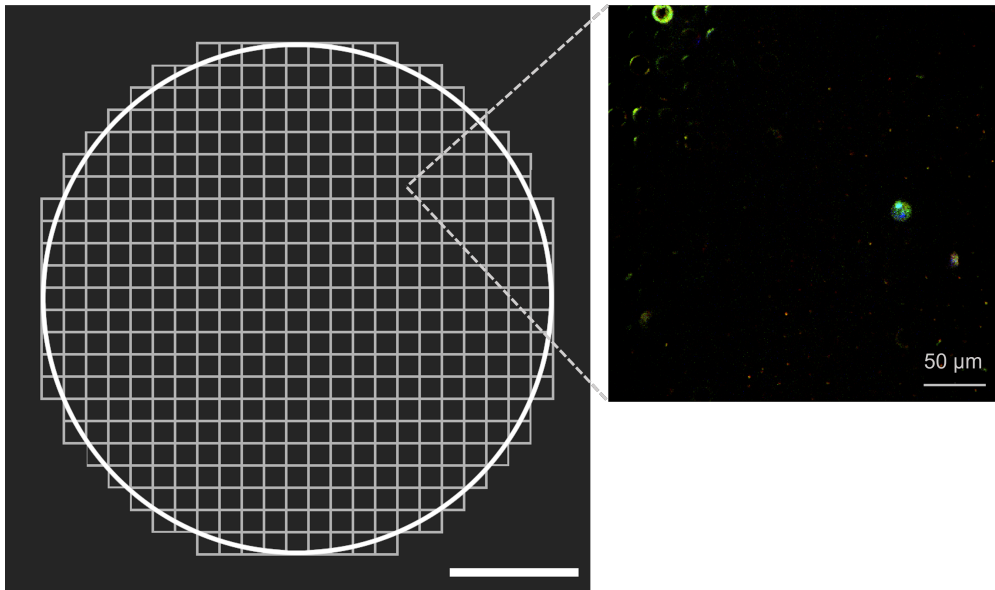


Figure 8: Partitioning of a hypothetical 8 mm diameter filter into ROIs for imaging with a 20X objective. A typical scan at 20X will involve 124 FOVs. Scale bar is 2 mm.

4.2 Discussion

The acquisition algorithm implemented is a practical method for imaging the filters of the G μ F CTC platform which, as of writing, it has been used for over 30 clinical samples. In comparison to manual acquisition, it facilitates collecting more images and richer data in a shorter amount of overall time and much shorter amount of active time. Active time, which consists of setup, is independent of the number of images acquired. This increases the practicality of using larger objectives, tighter z stack steps, and makes the question of acquiring richer data through these means one of data size, rather than of time and human endurance. The drawback of the algorithm is that it must collect more data than an ideal human operator would, because an ideal operator would only capture relevant object-containing images. The algorithm scans the entirety of the designated area without making any decision on whether it is looking at nothing, background signal, or regions of interest. The result is an increased number of images to analyse, which will increase analysis length, especially if being done manually.

Runtime is a function of the number of images to be captured, the dimensions of the resultant scan, and the frame time of the scanner. The XY dimension contributes much more than the Z dimension and is the primary source of variability in runtime between samples. Frame time factors include scan mode (resonant vs galvanometric), scan resolution, sequential vs simultaneous channels, and, if sequential, the number of channels. The resonant scanner is capable of high speed imaging compared to the linear galvanometric scanner (30 vs 4 frames per second at 512x512 pixels) but produces a noisier image. Provided that it meets the minimum quality standards to allow analysis (cell identification and counting, in this case) the fastest option is preferred. We have found resonant scanning at 512x512, followed by denoising (`denoise_ai`, NIS-Elements 5.30) to be of sufficient quality for CTC identification and enumeration at 20X and 40X objectives. Sequential acquisition of individual channels multiplies the frametime by the number of channels, but is preferential to simultaneous acquisition because it limits spectral bleed, does not increase active time, and still results in a

practical overall runtime. Although, subject to fluorophore selection, it is usually feasible to acquire channels 2 and 4 (488 and 640 nm excitation) simultaneously without serious overlap of emission spectra (*e.g.*, with Alexa Fluor 488 and Alexa Fluor 647). Scanning a filter at 40X in resonant mode at 512x512 with sequential channels images typically takes 40–60 minutes and produces 600x20 images (3–5 4-channel images per second).

5 Aim 3: Clinical Study of cCTC Incidence in CRCLM

Colorectal cancer (CRC) is one of the three most common cancers worldwide[15, 89]. The majority of CRC patients will develop metastases, the most common site of which is the liver[90, 91]. Survival of untreated patients with colorectal cancer liver metastases (CRCLM) is very poor; 5-year survival is 3.3% for metastases that develop within one year of CRC diagnosis and 6.1% for metastases developed over a year after CRC diagnosis[92]. Resection of liver lesions (hepatectomy) can improve 5-year survival by up to 50–60%[93] and is the only proven curative measure[94]. Unfortunately, the disease is commonly advanced enough that only a minority of CRCLM patients are eligible for the surgery[94, 95]. Preoperative therapy of chemotherapeutics, with or without the addition of biologicals, can turn initially unresectable metastases resectable, increasing the number of patients eligible for a potentially curative surgery. However, there is evidence of differential postsurgical outcome in patients categorized in the same TNM stage and receiving the same preoperative treatment[96, 95]. CRCLM treatment stands to improve from a deeper understanding of why this differential response occurs, and more precise eligibility criteria for hepatectomy selection.

HGP is a predictor of preoperative therapy response in CRCLM Recently, two major histological growth patterns (HGPs), replacement and desmoplastic, have been identified in resected CRCLM lesions which are able to stratify the differential outcomes not explained by the traditional TNM staging system[97, 98, 99]. A less common third pattern, pushing, has also been identified. These HGPs are distinguished by the interface

between the tumour and surrounding normal liver tissue (Figure 9[100]). In desmoplastic lesions tumour cells are separated from hepatocytes by a rim of desmoplastic stroma with inflammation present at the interface. In pushing lesions the liver plates are pushed aside to run parallel to the tumour which is separated from hepatocytes by a thin layer of reticulin fibers with mild inflammation at the interface. In replacement lesions tumour cells appear to replace hepatocytes and have direct hepatocyte contact with no inflammation at the interface[97]. It has been observed that CRCLM patients with desmoplastic lesions responded better to a regime of chemotherapy plus the antiangiogenic monoclonal antibody bevacizumab (bev-chemo) than those with replacement lesions[95, 98]. Not only has bev-chemo been found to be less effective for replacement HGP patients, but there is evidence of it actually worsening the outcome of patients with replacement pattern lesions compared to chemotherapy alone[98].

Bevacizumab is an expensive drug that can improve or worsen the outcome of CRCLM hepatectomy when used as in concert with chemotherapeutics as a multimodal preoperative therapy. This differential outcome is predicted HGP which is currently determined from analysing resected lesions at the time of surgery. Therefore, there is need to find a non-invasive predictor of HGP that can be analysed before hepatectomy in order to maximize the effectiveness and minimize the harmfulness and cost of preoperative bev-chemo in CRCLM patients. This motivated us to investigate if CTCs and CTC clusters captured by our G μ F platform could be used to stratify HGP in CRCLM patients.

5.1 Methods

5.1.1 Participants

13 blood samples (Table 1) were collected from patients diagnosed with colorectal cancer with liver metastasis (CRCLM). Samples are included from both treatment naïve (N=4) and patients who had undergone one or more cycles of chemotherapy (N=10). Blood was collected before surgical resection. The HGP type of the patient, either replacement (rHGP)

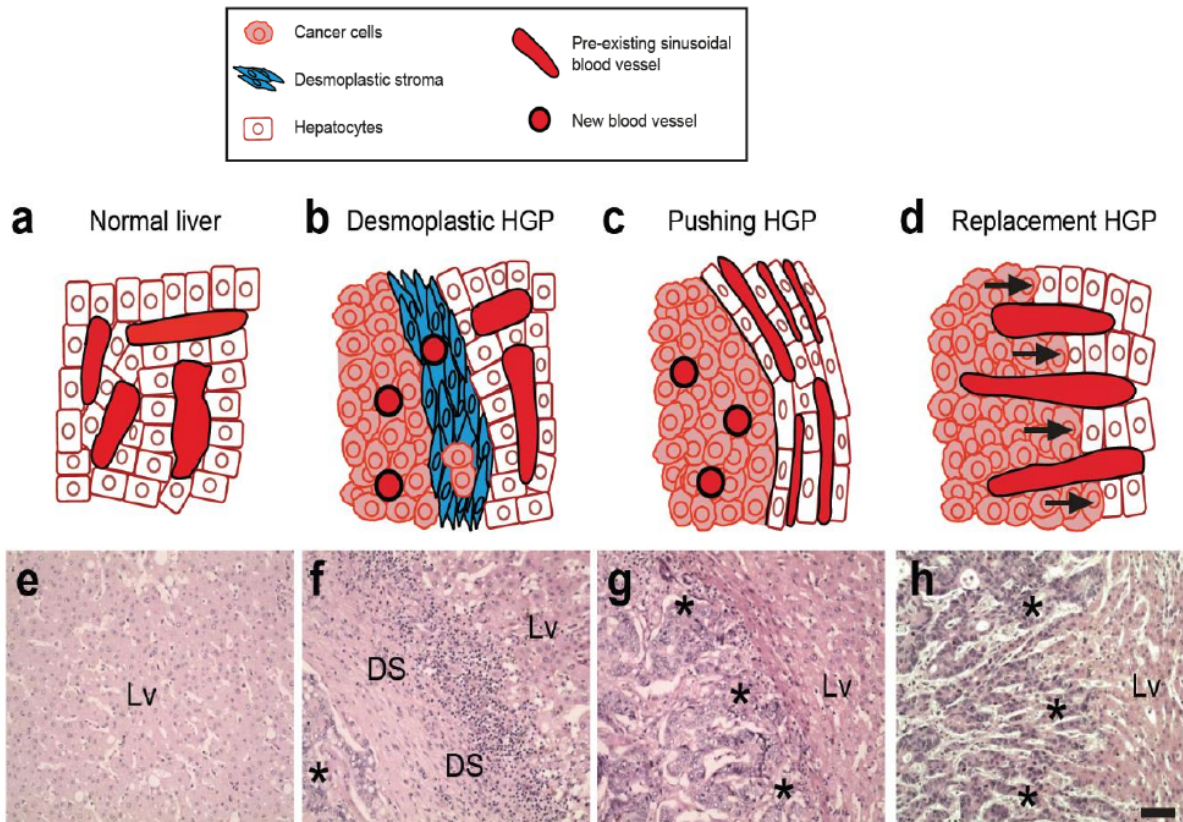


Figure 9: Diagrams (a–d) and hematoxylin & eosin histology (e–f) illustrating normal liver morphology and the tumour/hepatocyte interface morphology characteristics differentiating desmoplastic, pushing, and replacement HGP. Histology images are have annotations for normal liver (Lv), tumour cells (*), and desmoplastic stroma (Ds). Reproduced from [100] under CC BY 4.0

desmoplastic (dHGP), pushing (pHGP), or mixed, was determined from histology of tumour samples after the resection and defined as follows. Between one and five lesions were resected per patient. The subtype of each lesion is defined by the pattern that constitutes the majority of its area (*e.g.*, a lesion that is 51% desmoplastic and 49% replacement is classified as desmoplastic HGP). Patients with multiple lesions of different subtype are classified as mixed HGP (*e.g.*, a patient with four >50% lesions and one 80% desmoplastic lesion is classified as mixed HGP).

Sample	Volume Filtered (ml)	Sex	Diagnosis	Treatment Status	HGP	HGP Analysis
CR1	5.0	F	CRCLM	Naïve	rHGP	2 lesions: 99% replacement & 1% desmoplastic
CR2	5.0	F	CRCLM	Treated	rHGP	5 lesions: All at least 90% Replacement
CR3	3.0	M	CRCLM	Treated	rHGP	1 lesion: 80% Replacement & 20% desmoplastic
CR4	3.0	M	CRCLM	Treated	rHGP	1 lesion: Replacement
CR8	3.0	M	CRCLM	Treated	rHGP	
CR10	5.0	M	CRCLM	Treated	rHGP	1 lesion 100% replacement
CR13	3.0	F	CRCLM	Naïve	rHGP	3 lesions: 2 (90% replacement & 10% pushing) & 1 (98% replacement & 2% desmoplastic)
CR5	3.0	F	CRCLM	Treated	dHGP	3 lesions: Desmoplastic
CR6	3.0	M	CRCLM	Treated	dHGP	1 lesion: 15% Replacement & 85% Desmoplastic
CR7	3.0	M	CRCLM	Naïve	dHGP	1 lesion: Desmoplastic
CR12	3.0	F	CRCLM	Naïve	pHGP	1 lesion: 40% Replacement & 60% Pushing
CR9	2.5	M	CRCLM	Treated	Mixed	4 lesions: 3 >50% replacement, 1 lesion >80% desmoplastic
CR11	2.5	M	CRCLM	Treated	Mixed	2 lesions: 1 pushing & 1 desmoplastic

Table 1: CRCLM patient information. Histological growth pattern types: replacement (rHGP, N=7), desmoplastic (dHGP, N=3), pushing (pHGP, N=1), and mixed (N=2)

5.1.2 Isolation of CTCs from Blood by Gravity Microfiltration

The filtration setup consists of a cartridge assembly containing the 15 and 8 μm filters connected at the inlet to a reservoir (50 ml syringe with the plunger removed) via a 18 cm PVC inlet tube (1/16 inch ID, 1/8 inch OD) and at the outlet to a 26 gauge dispensing needle. The cartridge has male Luer-lock interfaces at the inlet and outlet. The reservoir and cartridge are affixed to a retort stand above a waste collection tube. A clamp on the inlet tube is used to stop and restart flow when necessary, such as when adding the blood sample to the reservoir, changing outlet connections, and during incubations. Blood samples are processed at room temperature within 24 hours of drawing and are stored at 4°C if processing is the next day.

Filters are assembled into the filtration cartridge and then are passivated to reduce nonspecific interaction by incubating in 2% bovine serum albumin (BSA) overnight at 4°C or 1 hour at room temperature. BSA solution is flowed through the cartridge by a syringe at the inlet and an tube is connected to the outlet to visualize air leaving the cartridge. Once no air bubbles are present in the outlet tube it is clamped, the inlet syringe is removed and replaced with a stopper, and finally the outlet tube replaced with a stopper. This results in a primed cartridge free of air, which could affect flow and create uneven distribution of fluid on the filter.

After incubation, the cartridge is connected to a PBS-primed reservoir and inlet tube, then a PBS-primed dispensing needle and rinsed with 3 ml PBS. Because the cartridge is primed with the BSA solution, flow should initiate on its own. The whole blood is diluted 1:6 with PBS and the surfactant pluronic to a final concentration of 0.05% pluronic. Mixing is done by inversion in order to gently treat the sample. The 21 ml of diluted blood is added to the reservoir and allowed to filter (about 60 min, maximum flow rate is 0.4 ml/min). Two backrinses are preformed using syringe pump (2 ml at 0.2 ml/min) followed by gravity flow.

5.1.3 Immunofluorescent Labeling of Captured Cells

After backrinsing the captured cells are fixed in-cartridge (4% PFA, 10 min), rinsed (PBS, 15 min), permeabilized (0.2% Triton-X, 5 min), rinsed (PBS, 15 min), and incubated with a blocking buffer (2 hours). These steps are carried out at room temperature, using the same gravity-driven flow as for filtration. Filters are incubated with pre-conjugated antibodies targeting CTC and WBC epitopes (CK18-AF488, CD45-AF647, 2 hours) followed by Hoechst 34580 (1/1000, 10 min) for DNA staining. Cartridges are dried by aspirating from the outlet and disassembled. Filter membranes are carefully removed or cut from their plastic carrier chips and mounted on a glass slide with a coverslip using Fluorogel and the coverslip sealed with transparent nail polish.

5.1.4 Image Classification

Positive CTCs are defined as DNA+/CK18+/CD45- objects greater than 6 μm in diameter and having cell-associated morphology (examples: Figure 10). DNA signal must be localized in defined nuclei that are not greater in size than the CK signal. Multinucleated CTCs, two or more nuclei localized within the same CK boundary, are counted as single cells. A cCTC consists of two or more CTCs linked by overlapping CK signal and/or connected by one or more WBCs (DNA+/CK18-/CD45+) in the XY or Z dimensions. Each cluster is considered a cCTC capture event containing N CTCs.

5.2 Results

scCTCs and cCTCs were found in all samples. The concentration of scCTCs (per ml of whole blood) ranged 4 to 99 for replacement (rHGP) patients, 14 to 26 for desmoplastic (dHGP), 31 to 51 for mixed HGP, and 61 for the pushing (pHGP) patient (Figure 11). Concentration of cCTCs (per ml) ranged 1 to 18 in rHGP, 2 to 4 in dHGP, 3 to 26 in mixed HGP, and was 30 in the pHGP patient (Table 2). The size of clusters captured ranged from 2–11 CTCs. rHGP samples were more likely to contain more (mean cCTC/ml of 7) and larger clusters

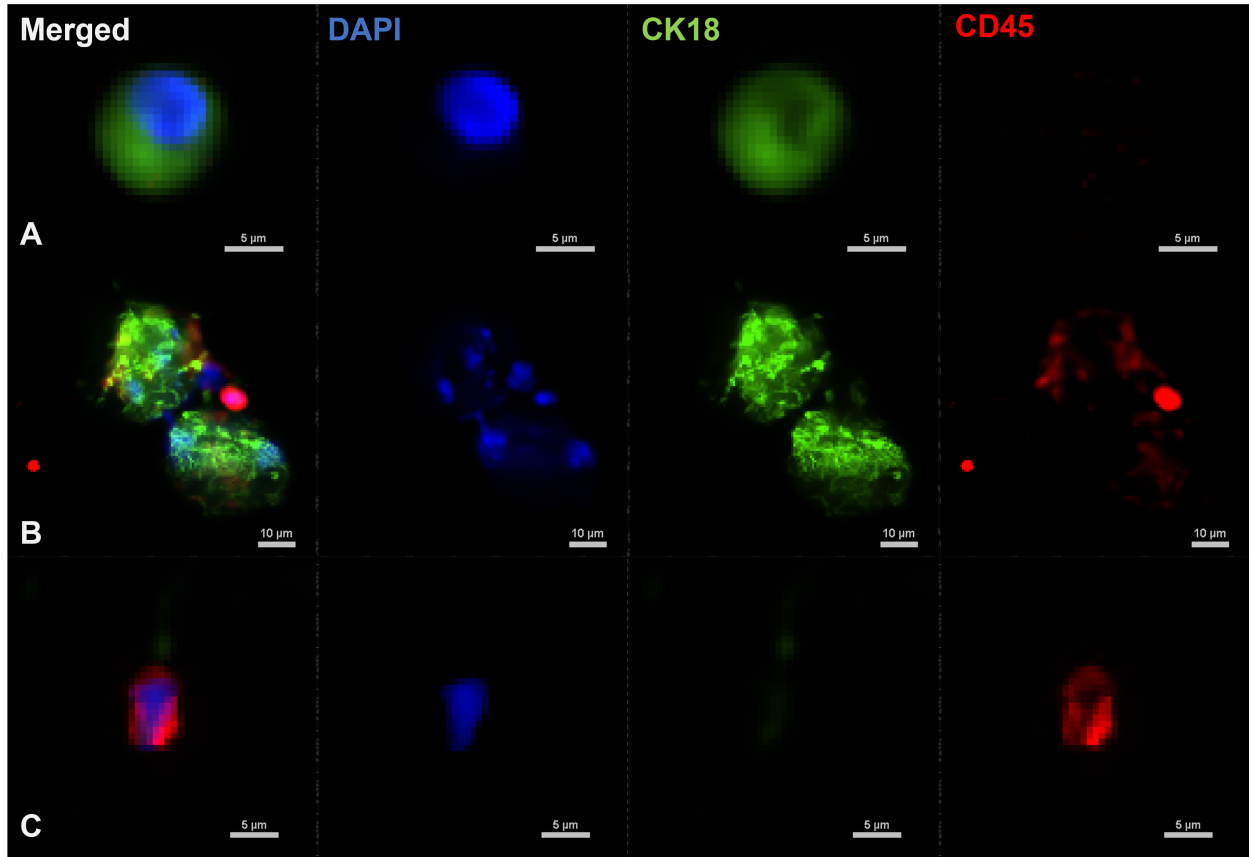


Figure 10: Fluorescence images showing examples of the different classes of cells captured and analysed from CRCLM blood samples: single CTC (A), a CTC cluster with two associated white blood cells (B), a white blood cell (C).

(Figure 12) compared to dHGP samples (mean cCTC/ml of 3).

Sample	HGP	WBC + cCTC	scCTC	cCTC Events	cCTC Cells	cCTC Size Min	cCTC Size Max	CTC /ml	cCTC /ml	% From cCTC
CR1	rHGP	Yes	23	6	43	4	11	13	1	65
CR2	rHGP	No	20	4	9	2	3	6	1	31
CR3	rHGP	Yes	73	27	77	2	7	50	9	51
CR4	rHGP	Yes	106	37	110	2	7	72	12	51
CR8	rHGP	Yes	167	4	10	2	3	59	1	6
CR10	rHGP	No	296	16	41	2	5	112	5	12
CR13	rHGP	Yes	107	45	134	2	10	96	18	56
CR5	dHGP	Yes	41	9	24	2	8	22	3	37
CR6	dHGP	No	83	22	52	2	4	27	4	39
CR7	dHGP	No	77	5	13	2	4	30	2	14
CR12	Mixed	Yes	92	10	29	2	5	40	3	24
CR9	Mixed	Yes	153	77	214	2	8	122	26	58
CR11	pHGP	Yes	153	74	191	2	6	138	30	56

Table 2: CRCLM CTC counts. WBC+CTC denotes whether any of the observed clusters contained leukocytes (≥ 2 CTCs and ≥ 1 WBCs). Each cCTC is considered a single event with a size equal to the number of CTCs it contains (excluding WBCs). cCTC cells is the total number of CTCs found in clusters. % from cCTC is percentage of total CTCs (scCTC + cCTC cells) found in clusters.

The concentration of cCTC cells per ml varied from 2 to 54 in rHGP, 4 to 10 in dHGP, 10 to 71 in mixed HGP, and was 76 in the pHGP patient. Cells from clusters represented the majority of total CTCs in the majority of rHGP (4/7) and none of the dHGP (0/3) patients (6/13 over all HGP subtypes). Both the patient with the lowest (6%) and highest (65%) proportion of cells found in cCTCs had replacement HGP.

5.3 Discussion

Incidence of CTCs and clusters The most prolific CTC isolation method in CRC literature is CellSearch and a count of ≥ 3 CTCs/7.5ml from this method is commonly considered an index of poor prognosis[101]. The CTC detection rate and counts from

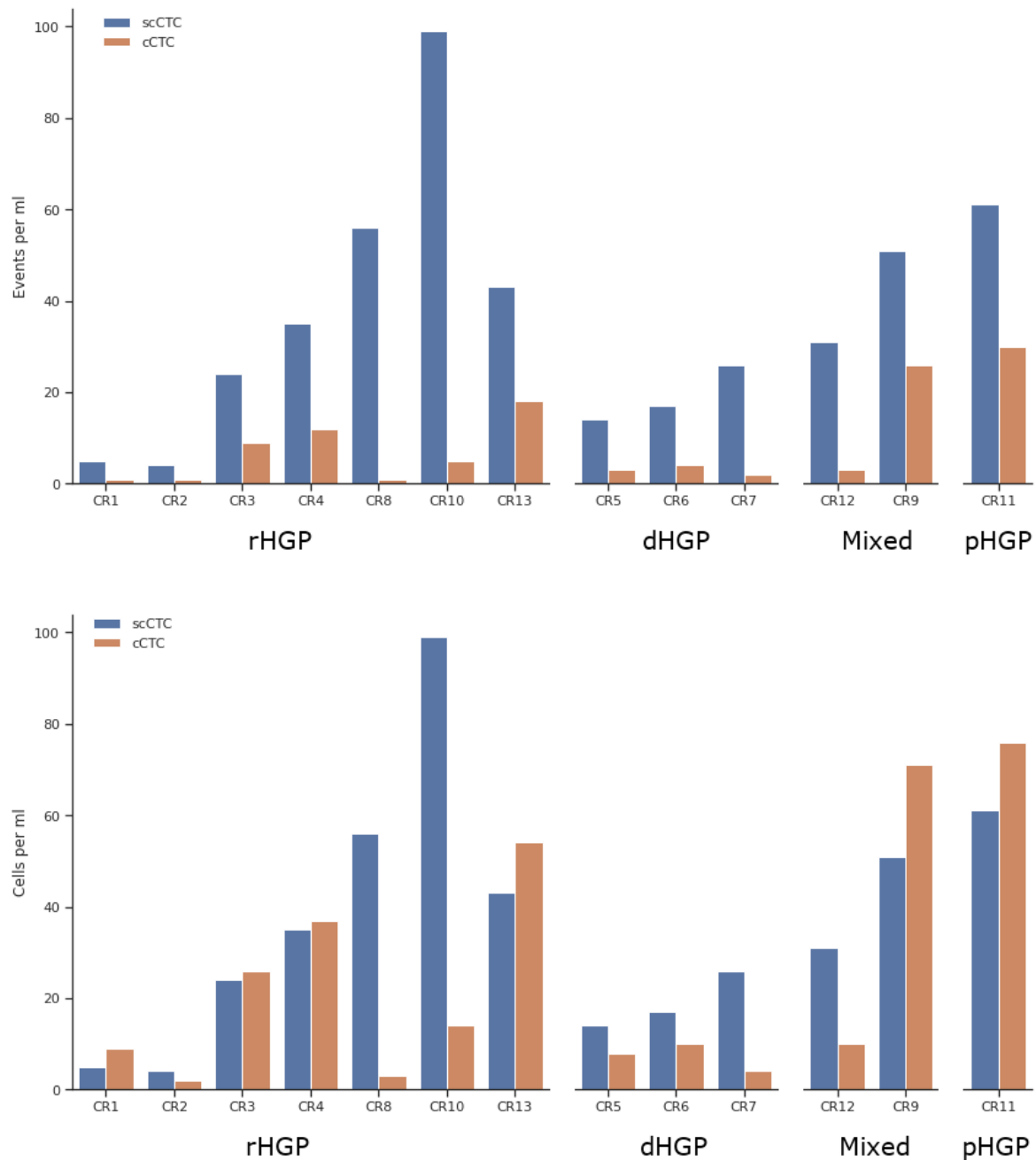


Figure 11: Concentrations of single CTCs (scCTCs), CTC clusters (cCTCs), and CTC cells found within clusters from CRCLM patient blood samples using the G_μF platform.

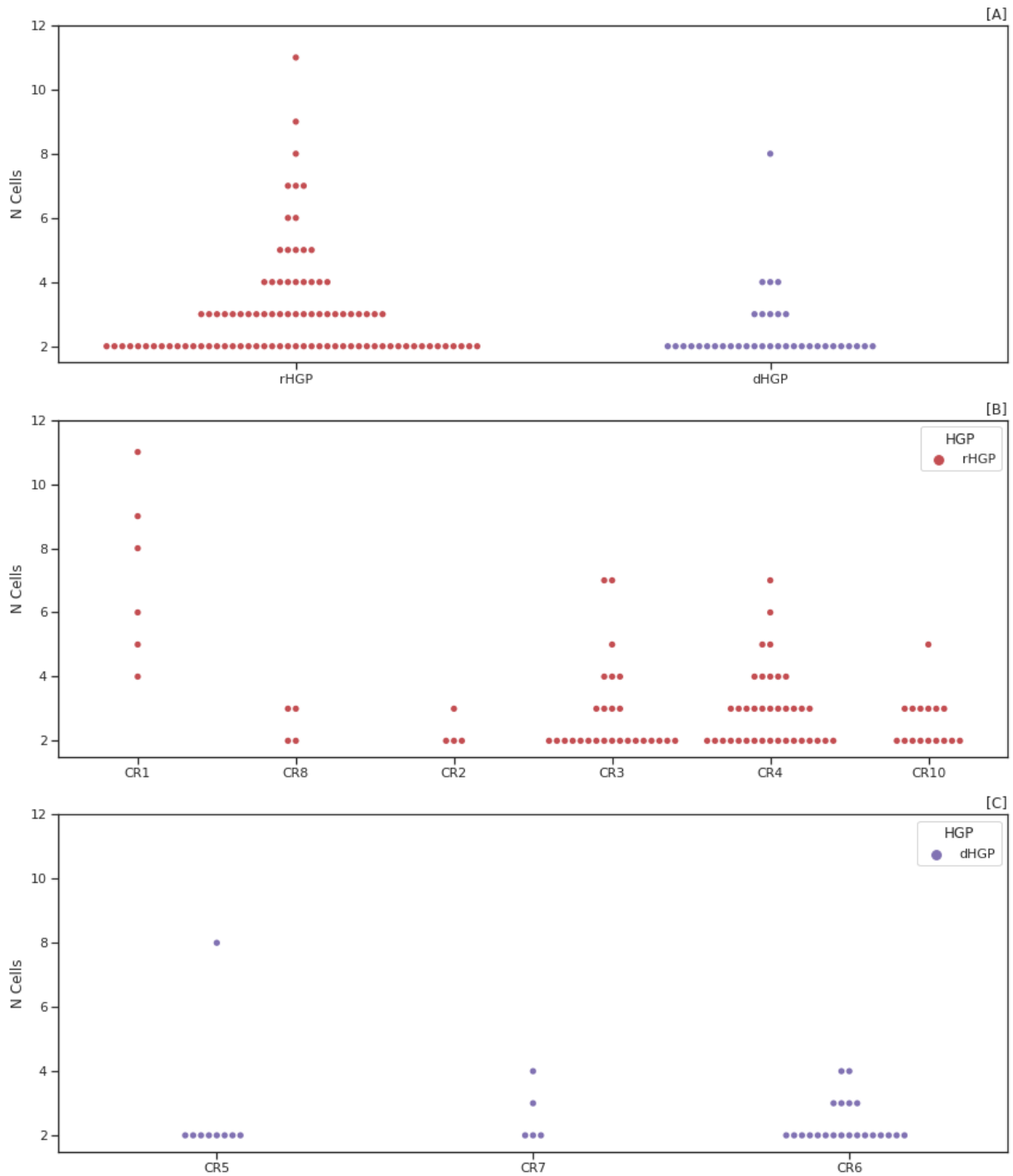


Figure 12: [A] Pooled CTC cluster (cCTC) size distributions of replacement (rHGP, N=7) and desmoplastic (dHGP, N=3) histological growth pattern CRCLM patients. [B,C] Per-sample cluster size distributions. Each dot represents one CTC cluster and its size (N Cells) is the number of CTCs (DNA+/CK+/CD45-) it contains, not including any WBCs (DNA+/CK-/CD45+).

CellSearch are generally low compared to more recently developed CTC isolation methods[75, 102, 103]. A meta-analysis of three studies using CellSearch reported that ≥ 3 CTCs/7.5 ml were found in only 68% (138/203) of CRCLM patients taken at baseline before treatment [104]. We found scCTCs at a concentration above 3 CTCs/7.5 ml and CTC clusters in 13/13 CRCLM patients.

Reports of CTC cluster counts in CRCLM patients are harder to come by in the literature, but those available find lower incidence rates than we have. For example, an ISET study (epitope-independent, track-etched membranes) found clusters in 18% of patients with advanced CRC undergoing chemotherapy [105]. A study using a microfluidic self-assembled cell array found EpCAM+ CTC clusters in 50% (8/16) of stage IV CRC patients[106]. We report a higher cluster-positive rate of 100% (13/13), a result that might be attributed to the sensitivity and gentle, self-adjusting, flow rate of the G μ F platform.

Comparison of rHGP and dHGP samples Replacement samples had higher average concentrations of total CTCs, scCTCs, and cCTCs, but much higher variance compared to desmoplastic samples. Thus, mean cell counts alone are not appropriate for distinguishing these two HGP subtypes in our data. Although the difference in per-subtype mean and median are both less than one, cCTC size still appears the most promising measure for HGP stratification (Figure 12). rHGP samples were more likely to contain larger clusters. Cells found in clusters accounted for >50% of the total CTCs captured in the majority of rHGP samples and none of the dHGP samples (Figure 11). If these observation were to hold over a larger sample, a possible explanation could be that the vascular co-option typical of replacement lesions[100] creates conditions more favorable to cluster extravasation.

These extremely preliminary results suggest that, from the measures we assessed, CTC cluster size and the proportion of CTCs found in clusters are the most promising candidates for stratifying replacement and desmoplastic HGP subtypes. Our G μ F platform is suitable for continuing this line of research due to its capacity to efficiently isolate CTC clusters.

However, it is important to consider that, because it is a strength of the technology, we are biased towards investigating the clinical utility of cCTCs captured in this manner. Both in terms of the research questions we select and in the measures the platform is currently able to provide: we are not performing any genomic tests and have only examined the minimal number of protein markers for CTC identification. Additional markers would enable estimations of phenotypes of interest. The mesenchymal marker Vim1 would provide a measure of EMT phenotype and allow identification of CK18-/Vim1+ CTCs and is therefore an intuitive choice. Another valuable addition to the panel would be the neutrophil marker CD16, both for the general roles they are proposed to play in extravasation of CTCs and specifically because of evidence that LOXL4-expressing neutrophils support the replacement HGP phenotype[107]. The inclusion of these markers would fit within our conventional five channel fluorescence microscopy setup; moving to larger numbers of markers would necessitate more specialized imaging technologies such as DNA exchange imaging (DEI).

6 Conclusion

Clinical application Gravity microfiltration (G μ F) using a sequence of 15 μ m and 8 μ m pore diameter filters has been demonstrated as an effective circulating tumour cell (CTC) enrichment technology using spike-in and ovarian cancer samples[11, 108]. Here we have shown the applicability of G μ F in isolating single cell CTCs (scCTCs) and CTC clusters (cCTCs) from the blood of colorectal cancer liver metastasis (CRCLM) patients. CTCs were found above the established clinical relevance threshold of 3 CTC/7.5 ml[109, 110] in 13/13 patients. In addition, we detected cCTCs in every patient, the first time to the best of our knowledge, and cluster-associated WBCs in 9/13 patients. We believe this high sensitivity to cCTCs reflects how the G μ F platform meets many of the technical challenges faced by the most widely-used CTC enrichment technologies. The system's uses gravity-driven, constant pressure flow, is gentle and prevents mechanical dissociation of the fragile clusters.

Epitope-independent mechanical capture provides unbiased capture of clusters with diverse bimolecular phenotype and heterogeneous cell composition. The technology does not sacrifice effective capture of single cells; we simultaneously capture scCTCs and cCTCs with high efficiency.

Technology development The technology development in this thesis has benefited the throughput of the G μ F platform, enabling greater clinical translation. By increasing the open-ratio of the membranes (Aim 1), the system flow rate was increased five-fold without increasing cluster-disrupting shear stress at the pore interface. Even without increasing the filter diameter, the flow rate achieved with 40% porosity filters has made running multiple parallel samples in a day manageable. Using a 15 μ m, 8 μ m stack with 8 mm diameter filters, the time to filter and fixate 3 ml of whole blood (diluted 1:6 to 21 ml) is 1.5 hours, compared to 5 hours with the previous 19.6% (15 μ m) and 8% (8 μ m) porosity stack. Increasing the volume of whole blood to 5 ml results in a runtime of approximately 2 hours (+15 minutes/ml). Adding a second sample in parallel typically only increases the time by 20 minutes. Thus, the practical bottleneck for sample parallelization is now the number of syringe pumps available for the backflow steps. The larger molds (Aim 1) have improved fabrication efficiency (more filters produced per mold assembly) and leave ample dimensional overhead for targeting even higher flow rates by increasing the filter diameter in the future. The programmable confocal routine (Aim 2) makes it trivial to scale up image acquisition for these hypothetical large filters. However, at current filter diameter, it already results in vast amounts of images which exasperates the length of manual analysis. It is not practical to increase the filter diameter so long as there is a reliance on manual image analysis; automated or even semi-automated image analysis presents the largest opportunity for breakthroughs in throughput. A simple, high-return, target would be a conservative, coarse region of interest (ROI) detection to remove data that is obviously junk (*e.g.*, areas with no signal or oversaturated membrane artifacts). This would remove a manual analysis step, reduce data weight, and ultimately

could be fed back into the acquisition algorithm for a coarse overview, high-magnification ROI scanning routine.

Future development The data from CRCLM patients (Aim 3) hints at the exciting possibility that the platform might be poised to identify and phenotype the individual tumour and non-tumour cells within CTC clusters; fertile ground for the discovery of novel biomarkers. There is increasing recognition in the CTC field of the importance of understanding the interactions between tumour, stroma, and immune cells. The complexity of CTC clusters begs for compatible highly-multiplexed proteomic analyses. One can quickly develop a list of relevant markers for characterizing CTCs (*e.g.*, EpCAM, CK, Vim1, Slug), ECM interactions (*e.g.*, integrins, claudins, ARP-2/3)[98], and, in the case of heterotypic clusters, non-tumour cells (*e.g.*, CD45, CD11b, LOXL4, CD169) that eclipses the spectral capacity of conventional immunofluorescence microscopy. Using DNA-barcoded labeling probes, such as with DNA exchange imaging (DEI) could overcome this limitation. DEI allows for rapid in-situ multiplexing without spectral constraints and is compatible with fixed cells[111, 112]. For DEI with cCTCs, it will be important to avoid dissociating clusters or affecting the spatial relationship between the cells. Cells captured on our filters could be "locked" into place using an imprint-transfer method to embed them in a thin hydrogel. As the membrane is transparent, it does not need to be removed to allow imaging from either above or below the filter surface. However, the membrane would ideally be separated from the cells in order to minimize the thickness of the hydrogel; a thinner hydrogel will facilitate faster flushing of reagents, and therefore faster DEI cycles. DEI would be especially potent if developed alongside CTC biobanking capacity. Because DEI is non-destructive, banked CTCs could be re-analysed for new biomarkers of interest. This would alleviate the need to recruit and draw fresh blood for every new CTC analysis, speeding up research and facilitating clinical translation.

References

- [1] Danny R. Welch and Douglas R. Hurst. “Defining the Hallmarks of Metastasis”. In: *Cancer Research* 79.12 (June 2019), pp. 3011–3027. ISSN: 0008-5472, 1538-7445. DOI: 10.1158/0008-5472.CAN-19-0458.
- [2] K. Pantel and M. R. Speicher. “The Biology of Circulating Tumor Cells”. In: *Oncogene* 35.10 (Mar. 2016), pp. 1216–1224. ISSN: 1476-5594. DOI: 10.1038/onc.2015.192.
- [3] Afroditi Nanou et al. “Tumour-Derived Extracellular Vesicles in Blood of Metastatic Cancer Patients Associate with Overall Survival”. In: *British Journal of Cancer* 122.6 (Mar. 2020), pp. 801–811. ISSN: 1532-1827. DOI: 10.1038/s41416-019-0726-9.
- [4] F. a. W. Coumans et al. “All Circulating EpCAM+CK+CD45- Objects Predict Overall Survival in Castration-Resistant Prostate Cancer”. In: *Annals of Oncology: Official Journal of the European Society for Medical Oncology* 21.9 (Sept. 2010), pp. 1851–1857. ISSN: 1569-8041. DOI: 10.1093/annonc/mdq030.
- [5] Dena Marrinucci et al. “Case Study of the Morphologic Variation of Circulating Tumor Cells”. In: *Human Pathology* 38.3 (Mar. 2007), pp. 514–519. ISSN: 0046-8177. DOI: 10.1016/j.humpath.2006.08.027.
- [6] Leonie L. Zeune et al. “How to Agree on a CTC: Evaluating the Consensus in Circulating Tumor Cell Scoring”. In: *Cytometry Part A* 93.12 (2018), pp. 1202–1206. ISSN: 1552-4930. DOI: 10.1002/cyto.a.23576.
- [7] Tyler A. Allen et al. “Circulating Tumor Cells Exit Circulation While Maintaining Multicellularity, Augmenting Metastatic Potential”. In: *Journal of Cell Science* 132.17 (Sept. 2019), jcs231563. ISSN: 0021-9533. DOI: 10.1242/jcs.231563.
- [8] Michael R. King et al. “A Physical Sciences Network Characterization of Circulating Tumor Cell Aggregate Transport”. In: *American Journal of Physiology-Cell Physiology* 308.10 (May 2015), pp. C792–C802. ISSN: 0363-6143. DOI: 10.1152/ajpcell.00346.2014.
- [9] Anne Meunier et al. “Combination of Mechanical and Molecular Filtration for Enhanced Enrichment of Circulating Tumor Cells”. In: *Analytical Chemistry* 88.17 (Sept. 2016), pp. 8510–8517. ISSN: 0003-2700, 1520-6882. DOI: 10.1021/acs.analchem.6b01324.
- [10] Javier Alejandro Hernández-Castro et al. “Fabrication of Large-Area Polymer Microfilter Membranes and Their Application for Particle and Cell Enrichment”. In: *Lab on a Chip* 17.11 (2017), pp. 1960–1969. ISSN: 1473-0197, 1473-0189. DOI: 10.1039/C6LC01525E.
- [11] Anne Meunier et al. “Gravity-Based Microfiltration Reveals Unexpected Prevalence of Circulating Tumor Cell Clusters in Ovarian Cancer”. In: *bioRxiv* (Sept. 2019), p. 773507. DOI: 10.1101/773507.
- [12] Freddie Bray et al. “The Ever-Increasing Importance of Cancer as a Leading Cause of Premature Death Worldwide”. In: *Cancer* 127.16 (2021), pp. 3029–3030. ISSN: 1097-0142. DOI: 10.1002/cncr.33587.

- [13] Hyuna Sung et al. “Global Cancer Statistics 2020: GLOBOCAN Estimates of Incidence and Mortality Worldwide for 36 Cancers in 185 Countries”. In: *CA: A Cancer Journal for Clinicians* 71.3 (2021), pp. 209–249. ISSN: 1542-4863. DOI: 10.3322/caac.21660.
- [14] Hanna Dillekås, Michael S. Rogers, and Oddbjørn Straume. “Are 90% of Deaths from Cancer Caused by Metastases?” In: *Cancer Medicine* 8.12 (Aug. 2019), pp. 5574–5576. ISSN: 2045-7634. DOI: 10.1002/cam4.2474.
- [15] J. Ferlay, D. M. Parkin, and E. Steliarova-Foucher. “Estimates of Cancer Incidence and Mortality in Europe in 2008”. In: *European Journal of Cancer* 46.4 (Mar. 2010), pp. 765–781. ISSN: 0959-8049. DOI: 10.1016/j.ejca.2009.12.014.
- [16] Mariangela Russo et al. “Tumor Heterogeneity and Lesion-Specific Response to Targeted Therapy in Colorectal Cancer”. In: *Cancer Discovery* 6.2 (Feb. 2016), pp. 147–153. ISSN: 2159-8274. DOI: 10.1158/2159-8290.CD-15-1283.
- [17] Wendy Onstenk et al. “Molecular Characteristics of Circulating Tumor Cells Resemble the Liver Metastasis More Closely than the Primary Tumor in Metastatic Colorectal Cancer”. In: *Oncotarget* 7.37 (Sept. 2016), pp. 59058–59069. ISSN: 1949-2553. DOI: 10.18632/oncotarget.10175.
- [18] Jiawei Zhou, Quefeng Li, and Yanguang Cao. “Spatiotemporal Heterogeneity across Metastases and Organ-Specific Response Informs Drug Efficacy and Patient Survival in Colorectal Cancer”. In: *Cancer Research* 81.9 (May 2021), pp. 2522–2533. ISSN: 0008-5472. DOI: 10.1158/0008-5472.CAN-20-3665.
- [19] Philippe L. Bedard et al. “Tumour Heterogeneity in the Clinic”. In: *Nature* 501.7467 (Sept. 2013), pp. 355–364. ISSN: 1476-4687. DOI: 10.1038/nature12627.
- [20] Michael Weller et al. “How We Treat Glioblastoma”. In: *ESMO Open*. How I Treat Cancer Special Issue 4 (Jan. 2019), e000520. ISSN: 2059-7029. DOI: 10.1136/esmoopen-2019-000520.
- [21] Giulia Siravegna et al. “Integrating Liquid Biopsies into the Management of Cancer”. In: *Nature Reviews Clinical Oncology* 14.9 (Sept. 2017), pp. 531–548. ISSN: 1759-4782. DOI: 10.1038/nrclinonc.2017.14.
- [22] Vathany Kulasingham, Maria P. Pavlou, and Eleftherios P. Diamandis. “Integrating High-Throughput Technologies in the Quest for Effective Biomarkers for Ovarian Cancer”. In: *Nature Reviews Cancer* 10.5 (May 2010), pp. 371–378. ISSN: 1474-1768. DOI: 10.1038/nrc2831.
- [23] Gianluca Lopez et al. “Molecular and Immunohistochemical Markers with Prognostic and Predictive Significance in Liver Metastases from Colorectal Carcinoma”. In: *International Journal of Molecular Sciences* 19.10 (Oct. 2018), p. 3014. ISSN: 1422-0067. DOI: 10.3390/ijms19103014.
- [24] Carme Balaña et al. “O6-Methyl-Guanine-DNA Methyltransferase Methylation in Serum and Tumor DNA Predicts Response to 1,3-Bis(2-Chloroethyl)-1-Nitrosourea but Not to Temozolamide Plus Cisplatin in Glioblastoma Multiforme1”. In: *Clinical Cancer Research* 9.4 (Apr. 2003), pp. 1461–1468. ISSN: 1078-0432.

- [25] Shalini Makawita and Eleftherios P Diamandis. “The Bottleneck in the Cancer Biomarker Pipeline and Protein Quantification through Mass Spectrometry–Based Approaches: Current Strategies for Candidate Verification”. In: *Clinical Chemistry* 56.2 (Feb. 2010), pp. 212–222. ISSN: 0009-9147. DOI: 10.1373/clinchem.2009.127019.
- [26] Małgorzata Muc-Wierzgoń et al. “Specific Metabolic Biomarkers as Risk and Prognostic Factors in Colorectal Cancer”. In: *World Journal of Gastroenterology : WJG* 20.29 (Aug. 2014), pp. 9759–9774. ISSN: 1007-9327. DOI: 10.3748/wjg.v20.i29.9759.
- [27] Parsa Charkhchi et al. “CA125 and Ovarian Cancer: A Comprehensive Review”. In: *Cancers* 12.12 (Dec. 2020), p. 3730. ISSN: 2072-6694. DOI: 10.3390/cancers12123730.
- [28] Florian Weiland et al. “Methods for Identification of CA125 from Ovarian Cancer Ascites by High Resolution Mass Spectrometry”. In: *International Journal of Molecular Sciences* 13.8 (Aug. 2012), pp. 9942–9958. ISSN: 1422-0067. DOI: 10.3390/ijms13089942.
- [29] Basant Kumar Thakur et al. “Double-Stranded DNA in Exosomes: A Novel Biomarker in Cancer Detection”. In: *Cell Research* 24.6 (June 2014), pp. 766–769. ISSN: 1748-7838. DOI: 10.1038/cr.2014.44.
- [30] Yaxin Guo et al. “Effects of Exosomes on Pre-Metastatic Niche Formation in Tumors”. In: *Molecular Cancer* 18.1 (Mar. 2019), p. 39. ISSN: 1476-4598. DOI: 10.1186/s12943-019-0995-1.
- [31] Mengdi Zhang et al. “Methods and Technologies for Exosome Isolation and Characterization”. In: *Small Methods* 2.9 (2018), p. 1800021. ISSN: 2366-9608. DOI: 10.1002/smt.201800021.
- [32] Johan Skog et al. “Glioblastoma Microvesicles Transport RNA and Proteins That Promote Tumour Growth and Provide Diagnostic Biomarkers”. In: *Nature Cell Biology* 10.12 (Dec. 2008), pp. 1470–1476. ISSN: 1476-4679. DOI: 10.1038/ncb1800.
- [33] Marie-Nicole Theodoraki et al. “Evaluation of Exosome Proteins by On-Bead Flow Cytometry”. In: *Cytometry Part A* 99.4 (2021), pp. 372–381. ISSN: 1552-4930. DOI: 10.1002/cyto.a.24193.
- [34] Golam Kibria et al. “A Rapid, Automated Surface Protein Profiling of Single Circulating Exosomes in Human Blood”. In: *Scientific Reports* 6.1 (Nov. 2016), p. 36502. ISSN: 2045-2322. DOI: 10.1038/srep36502.
- [35] E. Van Der Pol et al. “Optical and Non-Optical Methods for Detection and Characterization of Microparticles and Exosomes”. In: *Journal of Thrombosis and Haemostasis* 8.12 (2010), pp. 2596–2607. ISSN: 1538-7836. DOI: 10.1111/j.1538-7836.2010.04074.x.
- [36] George G. Daaboul et al. “Digital Detection of Exosomes by Interferometric Imaging”. In: *Scientific Reports* 6.1 (Nov. 2016), p. 37246. ISSN: 2045-2322. DOI: 10.1038/srep37246.
- [37] Shulin Huang et al. “microRNA Biomarkers in Colorectal Cancer Liver Metastasis”. In: *Journal of Cancer* 9.21 (Oct. 2018), pp. 3867–3873. ISSN: 1837-9664. DOI: 10.7150/jca.28588.

- [38] Shaniya Ahmad et al. “Long Non-Coding RNAs Regulated NF- κ B Signaling in Cancer Metastasis: Micromanaging by Not so Small Non-Coding RNAs”. In: *Seminars in Cancer Biology* (July 2021). ISSN: 1044-579X. DOI: 10.1016/j.semcan.2021.07.015.
- [39] Chang-Sook Hong et al. “Human Acute Myeloid Leukemia Blast-Derived Exosomes in Patient-Derived Xenograft Mice Mediate Immune Suppression”. In: *Experimental Hematology* 76 (Aug. 2019), 60–66.e2. ISSN: 0301-472X. DOI: 10.1016/j.exphem.2019.07.005.
- [40] Atsushi Suetsugu et al. “Imaging Exosome Transfer from Breast Cancer Cells to Stroma at Metastatic Sites in Orthotopic Nude-Mouse Models”. In: *Advanced Drug Delivery Reviews*. Exosomes; a Key to Delivering Genetic Materials 65.3 (Mar. 2013), pp. 383–390. ISSN: 0169-409X. DOI: 10.1016/j.addr.2012.08.007.
- [41] Rosandra N. Kaplan et al. “VEGFR1-positive Haematopoietic Bone Marrow Progenitors Initiate the Pre-Metastatic Niche”. In: *Nature* 438.7069 (Dec. 2005), pp. 820–827. ISSN: 1476-4687. DOI: 10.1038/nature04186.
- [42] Sachie Hiratsuka et al. “MMP9 Induction by Vascular Endothelial Growth Factor Receptor-1 Is Involved in Lung-Specific Metastasis”. In: *Cancer Cell* 2.4 (Oct. 2002), pp. 289–300. ISSN: 1535-6108. DOI: 10.1016/S1535-6108(02)00153-8.
- [43] Ayuko Hoshino et al. “Tumour Exosome Integrins Determine Organotropic Metastasis”. In: *Nature* 527.7578 (Nov. 2015), pp. 329–335. ISSN: 1476-4687. DOI: 10.1038/nature15756.
- [44] TR. ASHWORTH. “A Case of Cancer in Which Cells Similar to Those in the Tumours Were Seen in the Blood after Death”. In: *Aust Med J.* 14 (1869), p. 146.
- [45] Satoru Watanabe. “The Metastasizability of Tumor Cells”. In: *Cancer* 7.2 (1954), pp. 215–223. ISSN: 1097-0142. DOI: 10.1002/1097-0142(195403)7:2<215::AID-CNCR2820070203>3.0.CO;2-6.
- [46] William H. Knisely and M. S. Mahaley. “Relationship between Size and Distribution of “Spontaneous” Metastases and Three Sizes of Intravenously Injected Particles of VX2 Carcinoma”. In: *Cancer Research* 18.8 Part 1 (Sept. 1958), pp. 900–905. ISSN: 0008-5472, 1538-7445.
- [47] Isaiah J. Fidler. “The Relationship of Embolic Homogeneity, Number, Size and Viability to the Incidence of Experimental Metastasis”. In: *European Journal of Cancer (1965)* 9.3 (Mar. 1973), pp. 223–227. ISSN: 0014-2964. DOI: 10.1016/S0014-2964(73)80022-2.
- [48] A. Fatih Sarioglu et al. “A Microfluidic Device for Label-Free, Physical Capture of Circulating Tumor Cell Clusters”. In: *Nature Methods* 12.7 (July 2015), pp. 685–691. ISSN: 1548-7105. DOI: 10.1038/nmeth.3404.
- [49] Sunitha Nagrath et al. “Isolation of Rare Circulating Tumour Cells in Cancer Patients by Microchip Technology”. In: *Nature* 450.7173 (Dec. 2007), pp. 1235–1239. ISSN: 1476-4687. DOI: 10.1038/nature06385.

- [50] Vasudha Murlidhar et al. “Poor Prognosis Indicated by Venous Circulating Tumor Cell Clusters in Early-Stage Lung Cancers”. In: *Cancer Research* 77.18 (Sept. 2017), pp. 5194–5206. ISSN: 0008-5472. DOI: 10.1158/0008-5472.CAN-16-2072.
- [51] Costanza Paoletti et al. “Circulating Tumor Cell Clusters in Patients with Metastatic Breast Cancer: A SWOG S0500 Translational Medicine Study”. In: *Clinical Cancer Research* 25.20 (Oct. 2019), pp. 6089–6097. ISSN: 1078-0432. DOI: 10.1158/1078-0432.CCR-19-0208.
- [52] Chun Wang et al. “Improved Prognostic Stratification Using Circulating Tumor Cell Clusters in Patients with Metastatic Castration-Resistant Prostate Cancer”. In: *Cancers* 13.2 (Jan. 2021), p. 268. ISSN: 2072-6694. DOI: 10.3390/cancers13020268.
- [53] Maria Lee et al. “Predictive Value of Circulating Tumor Cells (CTCs) Captured by Microfluidic Device in Patients with Epithelial Ovarian Cancer”. In: *Gynecologic Oncology* 145.2 (May 2017), pp. 361–365. ISSN: 0090-8258. DOI: 10.1016/j.ygyno.2017.02.042.
- [54] Kelly M. MacArthur et al. “Detection of Brain Tumor Cells in the Peripheral Blood by a Telomerase Promoter-Based Assay”. In: *Cancer Research* 74.8 (Apr. 2014), pp. 2152–2159. ISSN: 0008-5472, 1538-7445. DOI: 10.1158/0008-5472.CAN-13-0813.
- [55] Ilona Krol et al. “Detection of Circulating Tumour Cell Clusters in Human Glioblastoma”. In: *British Journal of Cancer* 119.4 (Aug. 2018), pp. 487–491. ISSN: 1532-1827. DOI: 10.1038/s41416-018-0186-7.
- [56] Jackson D. Hamilton et al. “Glioblastoma Multiforme Metastasis Outside the CNS: Three Case Reports and Possible Mechanisms of Escape”. In: *Journal of Clinical Oncology* 32.22 (Feb. 2014), e80–e84. ISSN: 0732-183X. DOI: 10.1200/JCO.2013.48.7546.
- [57] Amelia J. Rushton et al. “A Review of Circulating Tumour Cell Enrichment Technologies”. In: *Cancers* 13.5 (Jan. 2021), p. 970. DOI: 10.3390/cancers13050970.
- [58] Kevin J. Cheung et al. “Polyclonal Breast Cancer Metastases Arise from Collective Dissemination of Keratin 14-Expressing Tumor Cell Clusters”. In: *Proceedings of the National Academy of Sciences* 113.7 (Feb. 2016), E854–E863. DOI: 10.1073/pnas.1508541113.
- [59] Ravikanth Maddipati and Ben Z. Stanger. “Pancreatic Cancer Metastases Harbor Evidence of Polyclonality”. In: *Cancer Discovery* 5.10 (Sept. 2015), pp. 1086–1097. ISSN: 2159-8274. DOI: 10.1158/2159-8290.CD-15-0120.
- [60] Barbara Maria Szczerba et al. “Neutrophils Escort Circulating Tumour Cells to Enable Cell Cycle Progression”. In: *Nature* 566.7745 (Feb. 2019), pp. 553–557. ISSN: 1476-4687. DOI: 10.1038/s41586-019-0915-y.
- [61] Roula Tziortzioti. “Color-Coded Imaging of Syngeneic Orthotopic Malignant Lymphoma Interacting with Host Stromal Cells During Metastasis”. In: *ANTICANCER RESEARCH* (2016), p. 6.

- [62] Samuel Amintas et al. “Circulating Tumor Cell Clusters: United We Stand Divided We Fall”. In: *International Journal of Molecular Sciences* 21.7 (Apr. 2020). ISSN: 1422-0067. DOI: 10.3390/ijms21072653.
- [63] Simon Heeke et al. “Never Travel Alone: The Crosstalk of Circulating Tumor Cells and the Blood Microenvironment”. In: *Cells* 8.7 (July 2019), p. 714. DOI: 10.3390/cells8070714.
- [64] Charles E. Gast et al. “Cell Fusion Potentiates Tumor Heterogeneity and Reveals Circulating Hybrid Cells That Correlate with Stage and Survival”. In: *Science Advances* 4.9 (Sept. 2018), eaat7828. ISSN: 2375-2548. DOI: 10.1126/sciadv.aat7828.
- [65] Yariswamy Manjunath et al. “Tumor-Cell-Macrophage Fusion Cells as Liquid Biomarkers and Tumor Enhancers in Cancer”. In: *International Journal of Molecular Sciences* 21.5 (Jan. 2020), p. 1872. DOI: 10.3390/ijms21051872.
- [66] Mian-Fu Cao et al. “Hybrids by Tumor-Associated Macrophages × Glioblastoma Cells Entail Nuclear Reprogramming and Glioblastoma Invasion”. In: *Cancer Letters* 442 (Feb. 2019), pp. 445–452. ISSN: 0304-3835. DOI: 10.1016/j.canlet.2018.11.016.
- [67] Michelle B. Chen et al. “Inflamed Neutrophils Sequestered at Entrapped Tumor Cells via Chemotactic Confinement Promote Tumor Cell Extravasation”. In: *Proceedings of the National Academy of Sciences* 115.27 (July 2018), pp. 7022–7027. ISSN: 0027-8424, 1091-6490. DOI: 10.1073/pnas.1715932115.
- [68] Monika Vishnoi et al. “The Isolation and Characterization of CTC Subsets Related to Breast Cancer Dormancy”. In: *Scientific Reports* 5.1 (Dec. 2015), p. 17533. ISSN: 2045-2322. DOI: 10.1038/srep17533.
- [69] Lan Huang et al. “High Expression of Plakoglobin Promotes Metastasis in Invasive Micropapillary Carcinoma of the Breast via Tumor Cluster Formation”. In: *Journal of Cancer* 10.12 (2019), pp. 2800–2810. ISSN: 1837-9664. DOI: 10.7150/jca.31411.
- [70] Nicola Aceto et al. “Circulating Tumor Cell Clusters Are Oligoclonal Precursors of Breast Cancer Metastasis”. In: *Cell* 158.5 (Aug. 2014), pp. 1110–1122. ISSN: 0092-8674. DOI: 10.1016/j.cell.2014.07.013.
- [71] Wataru Goto et al. “Circulating Tumor Cell Clusters-Associated Gene Plakoglobin Is a Significant Prognostic Predictor in Patients with Breast Cancer”. In: *Biomarker Research* 5.1 (May 2017), p. 19. ISSN: 2050-7771. DOI: 10.1186/s40364-017-0099-2.
- [72] Ruifang Gao et al. “CD44ICD Promotes Breast Cancer Stemness via PFKFB4-mediated Glucose Metabolism”. In: *Theranostics* 8.22 (2018), pp. 6248–6262. ISSN: 1838-7640. DOI: 10.7150/thno.28721.
- [73] Sofia Gkoutela et al. “Circulating Tumor Cell Clustering Shapes DNA Methylation to Enable Metastasis Seeding”. In: *Cell* 176.1 (Jan. 2019), 98–112.e14. ISSN: 0092-8674. DOI: 10.1016/j.cell.2018.11.046.
- [74] Hariprasad Thangavel et al. “A CTC-Cluster-Specific Signature Derived from OMICS Analysis of Patient-Derived Xenograft Tumors Predicts Outcomes in Basal-Like Breast Cancer”. In: *Journal of Clinical Medicine* 8.11 (Nov. 2019), p. 1772. DOI: 10.3390/jcm8111772.

- [75] M. Craig Miller et al. “The Parsortix™ Cell Separation System—A Versatile Liquid Biopsy Platform”. In: *Cytometry Part A* 93.12 (2018), pp. 1234–1239. ISSN: 1552-4930. DOI: 10.1002/cyto.a.23571.
- [76] Kay T. Yeung and Jing Yang. “Epithelial-Mesenchymal Transition in Tumor Metastasis”. In: *Molecular Oncology* 11.1 (Jan. 2017), pp. 28–39. ISSN: 15747891. DOI: 10.1002/1878-0261.12017.
- [77] S. H.-S. Lim et al. “Circulating Tumour Cells and the Epithelial Mesenchymal Transition in Colorectal Cancer”. In: *Journal of Clinical Pathology* 67.10 (Oct. 2014), pp. 848–853. ISSN: 0021-9746, 1472-4146. DOI: 10.1136/jclinpath-2014-202499.
- [78] F. Farace et al. “A Direct Comparison of CellSearch and ISET for Circulating Tumour-Cell Detection in Patients with Metastatic Carcinomas”. In: *British Journal of Cancer* 105.6 (Sept. 2011), pp. 847–853. ISSN: 1532-1827. DOI: 10.1038/bjc.2011.294.
- [79] Michiel Stevens et al. “VyCAP’s Puncher Technology for Single Cell Identification, Isolation, and Analysis”. In: *Cytometry Part A* 93.12 (2018), pp. 1255–1259. ISSN: 1552-4930. DOI: 10.1002/cyto.a.23631.
- [80] Chia-Heng Chu et al. “Hybrid Negative Enrichment of Circulating Tumor Cells from Whole Blood in a 3D-printed Monolithic Device”. In: *Lab on a Chip* 19.20 (2019), pp. 3427–3437. DOI: 10.1039/C9LC00575G.
- [81] Sam H. Au et al. “Microfluidic Isolation of Circulating Tumor Cell Clusters by Size and Asymmetry”. In: *Scientific Reports* 7.1 (May 2017), p. 2433. ISSN: 2045-2322. DOI: 10.1038/s41598-017-01150-3.
- [82] Swee Jin Tan et al. “Microdevice for the Isolation and Enumeration of Cancer Cells from Blood”. In: *Biomedical Microdevices* 11.4 (Aug. 2009), pp. 883–892. ISSN: 1572-8781. DOI: 10.1007/s10544-009-9305-9.
- [83] S. H. Seal. “A Sieve for the Isolation of Cancer Cells and Other Large Cells from the Blood”. In: *Cancer* 17.5 (1964), pp. 637–642. ISSN: 1097-0142. DOI: 10.1002/1097-0142(196405)17:5<637::AID-CNCR2820170512>3.0.CO;2-I.
- [84] Daniel L. Adams et al. “The Systematic Study of Circulating Tumor Cell Isolation Using Lithographic Microfilters”. In: *RSC Advances* 4.9 (2014), pp. 4334–4342. DOI: 10.1039/C3RA46839A.
- [85] Li Shi Lim et al. “Microsieve Lab-Chip Device for Rapid Enumeration and Fluorescence in Situ Hybridization of Circulating Tumor Cells”. In: *Lab on a Chip* 12.21 (Oct. 2012), pp. 4388–4396. ISSN: 1473-0189. DOI: 10.1039/C2LC20750H.
- [86] Siegfried Ripperger et al. “Filtration, 1. Fundamentals”. In: *Ullmann’s Encyclopedia of Industrial Chemistry*. American Cancer Society, 2013, pp. 1–38. ISBN: 978-3-527-30673-2. DOI: 10.1002/14356007.b02_10.pub3.
- [87] *A Simple and Economical Holder for Casting PDMS Chips – Chips and Tips*.
- [88] Maya Kleiman, Keun Ah Ryu, and Aaron P. Esser-Kahn. “Determination of Factors Influencing the Wet Etching of Polydimethylsiloxane Using Tetra-n-butylammonium Fluoride”. In: *Macromolecular Chemistry and Physics* 217.2 (2016), pp. 284–291. ISSN: 1521-3935. DOI: 10.1002/macp.201500225.

- [89] René Adam et al. “The Oncosurgery Approach to Managing Liver Metastases from Colorectal Cancer: A Multidisciplinary International Consensus”. In: *The Oncologist* 17.10 (Oct. 2012), pp. 1225–1239. ISSN: 1083-7159. DOI: 10.1634/theoncologist.2012-0121.
- [90] Mustafa Raof et al. “Systematic Failure to Operate on Colorectal Cancer Liver Metastases in California”. In: *Cancer Medicine* 9.17 (2020), pp. 6256–6267. ISSN: 2045-7634. DOI: 10.1002/cam4.3316.
- [91] H. J. Schmoll et al. “ESMO Consensus Guidelines for Management of Patients with Colon and Rectal Cancer. A Personalized Approach to Clinical Decision Making”. In: *Annals of Oncology* 23.10 (Oct. 2012), pp. 2479–2516. ISSN: 0923-7534. DOI: 10.1093/annonc/mds236.
- [92] Sylvain Manfredi et al. “Epidemiology and Management of Liver Metastases From Colorectal Cancer”. In: *Annals of Surgery* 244.2 (Aug. 2006), pp. 254–259. ISSN: 0003-4932. DOI: 10.1097/01.sla.0000217629.94941.cf.
- [93] Antoine Brouquet et al. “High Survival Rate After Two-Stage Resection of Advanced Colorectal Liver Metastases: Response-Based Selection and Complete Resection Define Outcome”. In: *Journal of Clinical Oncology* 29.8 (Mar. 2011), pp. 1083–1090. ISSN: 0732-183X. DOI: 10.1200/JCO.2010.32.6132.
- [94] Vijay P. Khatri, Nicholas J. Petrelli, and Jacques Belghiti. “Extending the Frontiers of Surgical Therapy for Hepatic Colorectal Metastases: Is There a Limit?” In: *Journal of Clinical Oncology* 23.33 (Nov. 2005), pp. 8490–8499. ISSN: 0732-183X. DOI: 10.1200/JCO.2004.00.6155.
- [95] Graeme J. Poston et al. “Urgent Need for a New Staging System in Advanced Colorectal Cancer”. In: *Journal of Clinical Oncology* 26.29 (Oct. 2008), pp. 4828–4833. ISSN: 0732-183X, 1527-7755. DOI: 10.1200/JCO.2008.17.6453.
- [96] Iris D. Nagtegaal, Phil Quirke, and Hans-Joachim Schmoll. “Has the New TNM Classification for Colorectal Cancer Improved Care?” In: *Nature Reviews Clinical Oncology* 9.2 (Feb. 2012), pp. 119–123. ISSN: 1759-4782. DOI: 10.1038/nrclinonc.2011.157.
- [97] Peter B. Vermeulen et al. “Liver Metastases from Colorectal Adenocarcinomas Grow in Three Patterns with Different Angiogenesis and Desmoplasia”. In: *The Journal of Pathology* 195.3 (2001), pp. 336–342. ISSN: 1096-9896. DOI: 10.1002/path.966.
- [98] Sophia Frentzas et al. “Vessel Co-Option Mediates Resistance to Anti-Angiogenic Therapy in Liver Metastases”. In: *Nature Medicine* 22.11 (Nov. 2016), pp. 1294–1302. ISSN: 1546-170X. DOI: 10.1038/nm.4197.
- [99] Pieter-Jan van Dam et al. “International Consensus Guidelines for Scoring the Histopathological Growth Patterns of Liver Metastasis”. In: *British Journal of Cancer* 117.10 (Nov. 2017), pp. 1427–1441. ISSN: 1532-1827. DOI: 10.1038/bjc.2017.334.
- [100] Rafif Mattar. *Colorectal cancer liver metastasis histological growth patterns; the role of the immune system*. <https://escholarship.mcgill.ca/concern/theses/3r074x61k>.

- [101] Jennifer E. Hardingham et al. “Detection and Clinical Significance of Circulating Tumor Cells in Colorectal Cancer—20 Years of Progress”. In: *Molecular Medicine* 21.1 (Jan. 2015), S25–S31. ISSN: 1528-3658. DOI: 10.2119/molmed.2015.00149.
- [102] Muhammad Umer et al. “Circulating Tumor Microemboli: Progress in Molecular Understanding and Enrichment Technologies”. In: *Biotechnology Advances* 36.4 (July 2018), pp. 1367–1389. ISSN: 0734-9750. DOI: 10.1016/j.biotechadv.2018.05.002.
- [103] Arash Dalili, Ehsan Samiei, and Mina Hoorfar. “A Review of Sorting, Separation and Isolation of Cells and Microbeads for Biomedical Applications: Microfluidic Approaches”. In: *Analyst* 144.1 (2019), pp. 87–113. DOI: 10.1039/C8AN01061G.
- [104] Xuanzhang Huang et al. “Meta-Analysis of the Prognostic Value of Circulating Tumor Cells Detected with the CellSearch System in Colorectal Cancer”. In: *BMC Cancer* 15.1 (Mar. 2015), p. 202. ISSN: 1471-2407. DOI: 10.1186/s12885-015-1218-9.
- [105] Dejun Zhang et al. “Circulating Tumor Microemboli (CTM) and Vimentin+ Circulating Tumor Cells (CTCs) Detected by a Size-Based Platform Predict Worse Prognosis in Advanced Colorectal Cancer Patients during Chemotherapy”. In: *Cancer Cell International* 17.1 (Jan. 2017), p. 6. ISSN: 1475-2867. DOI: 10.1186/s12935-016-0373-7.
- [106] Hsueh-Yao Chu et al. “Highly Correlated Recurrence Prognosis in Patients with Metastatic Colorectal Cancer by Synergistic Consideration of Circulating Tumor Cells/Microemboli and Tumor Markers CEA/CA19-9”. In: *Cells* 10.5 (May 2021), p. 1149. ISSN: 2073-4409. DOI: 10.3390/cells10051149.
- [107] Vincent Palmieri et al. “Neutrophils Expressing Lysyl Oxidase-like 4 Protein Are Present in Colorectal Cancer Liver Metastases Resistant to Anti-Angiogenic Therapy”. In: *The Journal of Pathology* 251.2 (2020), pp. 213–223. ISSN: 1096-9896. DOI: 10.1002/path.5449.
- [108] Anne Meunier et al. “Abstract 1562: Clusters of Circulating Tumor Cells Were Selectively Isolated in the Blood of 12/12 Epithelial Ovarian Cancer Patients Using Facile Gravity-Flow-Based Filtration Method Adapted to Clinical Use”. In: *Cancer Research* 78.13 Supplement (July 2018), pp. 1562–1562. ISSN: 0008-5472, 1538-7445. DOI: 10.1158/1538-7445.AM2018-1562.
- [109] Steven J. Cohen et al. “Relationship of Circulating Tumor Cells to Tumor Response, Progression-Free Survival, and Overall Survival in Patients With Metastatic Colorectal Cancer”. In: *Journal of Clinical Oncology* 26.19 (July 2008), pp. 3213–3221. ISSN: 0732-183X. DOI: 10.1200/JCO.2007.15.8923.
- [110] Shiyu Jia et al. “Clinical and Biological Significance of Circulating Tumor Cells, Circulating Tumor DNA, and Exosomes as Biomarkers in Colorectal Cancer”. In: *Oncotarget* 8.33 (Apr. 2017), pp. 55632–55645. ISSN: 1949-2553. DOI: 10.18632/oncotarget.17184.
- [111] Randy J. Giedt et al. “Single-Cell Barcode Analysis Provides a Rapid Readout of Cellular Signaling Pathways in Clinical Specimens”. In: *Nature Communications* 9.1 (Oct. 2018), p. 4550. ISSN: 2041-1723. DOI: 10.1038/s41467-018-07002-6.

- [112] Erik Gerdtsen et al. “Multiplex Protein Detection on Circulating Tumor Cells from Liquid Biopsies Using Imaging Mass Cytometry”. In: *Convergent Science Physical Oncology* 4.1 (Jan. 2018), p. 015002. ISSN: 2057-1739. DOI: 10.1088/2057-1739/aaa013.

Appendices

A Manuscript Contribution

During the course of this thesis I was fortunate to be able to contribute my work to a manuscript (attached below). Specifically, I fabricated the filters and performed the microscopy for the majority of the samples in the 'capture of cCTCs from cancer patients' experiment (Figure 5). I also processed (filtration and staining of cells from blood samples) and performed cell characterization and analyses for the CRCLM patient samples (Figure 5-C, F, and I).

Gravity-based microfiltration reveals unexpected prevalence of circulating tumor cell clusters in ovarian cancer

Anne Meunier,^{1,2} Javier Alejandro Hernández-Castro,^{1,2,3} Nicholas Chahley,^{1,2} Laudine Communal,⁴ Sara Kheireddine,^{1,2} Newsha Koushki,^{1,2} Sara Al Habyan,^{5,6} Benjamin Péant,⁴ Anthoula Lazaris,⁷ Andy Ng,^{1,2} Teodor Veres,^{1,3} Luke McCaffrey,^{5,6,8} Diane Provencher,^{4,9} Peter Metrakos,⁷ Anne-Marie Mes-Masson,^{4,10} and David Juncker^{1,2,5,6,11*}

Affiliations

¹ Biomedical Engineering Department, McGill University, Montreal, QC, H3A 2B4, Canada

² McGill Genome Centre, McGill University, Montreal, QC, H3A 0G1, Canada

³ National Research Council of Canada, QC, J4B 6Y4, Canada

⁴ Institut du cancer de Montréal and Centre de recherche du Centre hospitalier de l'Université de Montréal (CRCHUM), QC, H2X 0A9, Canada

⁵ Rosalind and Morris Goodman Cancer Research Centre, McGill University, Montreal, QC, H3A 1A3, Canada

⁶ Division of Experimental Medicine, McGill University, Montreal, QC, H4A 3J1, Canada

⁷ Cancer Research Program, The Research Institute of McGill University Health Center, Montreal, Quebec, H4A 3J1, Canada

⁸ Gerald Bronfman Department of Oncology, McGill University, Montreal, QC, H4A 3T2, Canada

⁹ Division of Gynecologic Oncology, Department of Obstetrics-Gynecology, Université de Montréal, Montreal, QC H3T 1J4, Canada

¹⁰ Department of Medicine, Faculty of Medicine, Université de Montréal, Montréal, QC H3T 1J4, Canada

¹¹ Neurology and Neurosurgery Department, McGill University, Montreal, H3A 2B4, QC, Canada

* Correspondence: david.juncker@mcgill.ca

Summary

Circulating tumor cells (CTCs) are rare (few cells per milliliter of blood) and mostly isolated as single cell CTCs (scCTCs). CTC clusters (cCTCs), even rarer, are of growing interest, notably because of their higher metastatic potential, but very difficult to isolate. Here, we introduce gravity-based microfiltration (G μ F) for facile isolation of cCTCs while minimizing unwanted cluster disaggregation, with ~85% capture efficiency. G μ F from orthotopic ovarian cancer mouse models, from 17 epithelial ovarian cancer (EOC) with either localized or metastatic disease, and 13 metastatic colorectal cancer liver metastasis (CRCLM) patients uncovered cCTCs in every case, with between 2-100+ cells. cCTCs represented between 5-30% of all CTC capture events, and 10-80% of CTCs were clustered; remarkably, in 10 patients, most CTCs were circulating not as scCTCs, but as cCTCs. G μ F uncovered the unexpected prevalence and frequency of cCTCs including sometimes very large ones in EOC patients, and motivates additional studies to uncover their properties and role in disease progression.

Keywords

Circulating tumor cells (CTCs), clusters of circulating tumor cells (cCTCs), CTC enrichment, gravity-based microfiltration (G μ F), epithelial ovarian cancer (EOC), epithelial-mesenchymal transition (EMT)

Introduction

Circulating tumor cells (CTCs) are shed from the tumor into the bloodstream, then circulate and reach distant locations where they can extravasate, proliferate and seed metastases. CTCs, found in the majority of epithelial cancers (Pantel and Speicher, 2016), represent a crucial intermediate in the metastatic cascade and their study has the potential to help improve patient care. CTCs are extremely rare (~1-10 CTCs vs. $< 10^6$ leukocytes and $< 10^9$ erythrocytes per milliliter of blood) and display extensive molecular heterogeneity. CTCs in blood are correlated with poor outcome, recurrence and resistance to therapy (Pantel and Speicher, 2016, Poveda et al., 2011). CTCs were first reported in 1869 (Ashworth, 1869), and interest has dramatically increased in the last decades following technical advances permitting simplified and effective isolation and quantification.

CTCs exist as single cells (scCTCs) and multicellular aggregates, called CTC clusters (cCTCs). scCTCs were traditionally isolated and identified based on the expression of the Epithelial Cell Adhesion Molecule (EpCAM) and cytokeratins (CK), but it became known that many scCTCs are disseminated following epithelial-mesenchymal transition (EMT) leading to the downregulation of epithelial markers and resulting in their enhanced motility and aggressiveness (Pantel and Speicher, 2016). cCTCs do not arise from scCTC proliferation in blood but separate from the primary tumor as a cluster (collective dissemination) (Aceto et al., 2014). Using mouse models, Aceto *et al.* found that cCTCs accounted for 3% of all captured CTC events, but have a 23- to 50-time higher metastatic potential than scCTCs (Aceto et al., 2014). The presence of cCTCs in blood has been associated with worse outcome in patients with lung, breast, prostate, skin, bladder, (Gazzaniga et al., 2014) pancreatic, (Effenberger et al., 2018) head and neck, (Garrel et al., 2019) colorectal (Yokobori et al., 2013, Abdalla et al., 2021, Heidrich et al., 2021) and ovarian cancer (Au et al., 2016, Sarioglu et al., 2015, Pantel and Speicher, 2016, Aceto et al., 2014).

The five-year survival in EOC is ~45%, owing to late diagnosis and lack of effective therapy (Lheureux et al., 2019). In epithelial ovarian cancer (EOC), CTCs were detected in the blood of ~10 to ~60% patients (Judson et al., 2003, Fan et al., 2009), travelling as scCTCs (Allard et al., 2004) and rarely as cCTCs (Guo et al., 2018). EOC is also characterized by the formation of ascites within the peritoneal cavity, that contain tumor cells and provide a local microenvironment regulating the behavior of scCTCs and cCTCs (Kim et al., 2016). In line with observations of Aceto *et al.* in blood, Al Habyan *et al.* (Al Habyan et al., 2018) showed that CTCs in ascites of EOC mouse models arise from spontaneous detachment as either single cells or clusters with cCTCs representing between 17-49% of all CTC capture events. Enriching

cCTCs is therefore of great interest as their characterization could offer new insights into cancer dissemination, and help improve prognosis and treatments in cancer.

In Colorectal Cancer (CRC), CTC could often only be detected in a subset of patients. One study found ≥ 1 CTC 7.5 per mL in 54%, and ≥ 3 CTC 7.5 per mL in 18.6 to 30% of pre-surgery patients (Cohen *et al.*, 2008). In a more recent study, CTCs were detected in all stages of the Union of International Cancer Control (UICC), while ≥ 1 CTC 7.5 per mL were detected in 46% of pre-surgery patients (Abdalla *et al.*, 2021). The detection of one or more CTCs 7.5 per mL correlated to metastases, shorter progress-free and overall survival. High CTC count was associated with poor prognosis in metastatic CRC (Cohen *et al.*, 2008, Arrazubi *et al.*, 2019, Bidard *et al.*, 2019, Abdalla *et al.*, 2021, Silva *et al.*, 2021). cCTCs have only been rarely reported, while 1 to 5.4 cCTC per mL were detected in advanced and metastatic CRC (Zhang *et al.*, 2017).

Isolating cCTCs is more challenging given their rarity, their short lifespan, and their propensity to disaggregate under shear (Sarioglu *et al.*, 2015). Isolation technologies were initially developed and optimized for scCTCs, but following the occasional capture of cCTCs (Brandt *et al.*, 1996, Reddy *et al.*, 2016, Stott *et al.*, 2010), were overhauled for efficiently and selectively isolating clusters (Ferreira *et al.*, 2016). Toner and colleagues pioneered two advances. One was based on deterministic lateral displacement tuned to deflects particles $> 30 \mu\text{m}$ tested with isolated artificial breast cancer cell clusters spiked in blood, but not yet on patient samples (Au *et al.*, 2017). They also developed a filtration-based chip (Cluster-chip) using shifted triangular pillars forming 4000 parallel $12 \times 100 \mu\text{m}^2$ slit openings designed to permit scCTC passage while capturing cCTCs (Sarioglu *et al.*, 2015). Artificial clusters spiked into blood were captured with a yield of 100% for sizes of 4-cells and above at a flow rate of 0.04 mL min^{-1} by looking at clusters on the filter and in the filtrate. The Cluster-chip was used with blood from metastatic breast, prostate, and skin cancer, and cCTCs with 2-19 cells were isolated from as many as 30-40% patients, the highest reported to date in our knowledge, and illustrating how the performance of the isolation method could bias our perception about cCTC prevalence (Sarioglu *et al.*, 2015).

Limitations of CTC technologies include long processing times for cCTC isolation to reduce shear and the risk of cCTCs dissociation. Therefore lower flow rates are preferred, increasing the processing time. Cheng *et al.* used a three-dimensional scaffold to reduce shear stress, capturing both scCTCs and cCTCs at $50 \mu\text{L min}^{-1}$, but aggregation and break-up on the filter could confound the quantification of cCTC filtration efficiency (Cheng *et al.*, 2017).

Microfiltration is geometrically predisposed to low shear stresses because a small filter < 1 cm in diameter can accommodate hundreds of thousands of pores, each forming a parallel flow path with a very low flow and shear. Microfiltration of scCTC was first reported in 1964 (Seal, 1964), using track-etched membranes with a random pore distribution that limits porosity to < 5% as well as flow rate and throughput (Sarioglu et al., 2015). Interestingly, the use of such microfilters for cCTC isolation has been reported by Sarioglu *et al.* using 5 μm -diameter pores, but with very low yield (Sarioglu et al., 2015). Isoporous membranes with high porosity made by microfabrication can accommodate higher flow rates while maintaining low shear stress (Adams et al., 2014, Ferreira et al., 2016, Lim et al., 2012). We developed high performance polymer microfilters that satisfy key criteria for practical use, namely low-cost, durable, highly transparent, non-autofluorescent and highly porous (20-60%) (Hernandez-Castro et al., 2017). Following optimization, 8 mm-diameter microfilters with 8 μm pores, a 1:6 dilution of whole blood in phosphate buffer saline (PBS), and a flow rate of 0.1 mL min⁻¹ set using programmable syringe pumps allowed us to recover > 80-95% of cancer cells spiked into blood (Meunier et al., 2016).

Here, we introduce gravity-based microfiltration (G μ F) for the efficient isolation of cCTCs using the in-house fabricated microfilters described above (Hernandez-Castro et al., 2017), and 3D printed cartridges (Meunier et al., 2016). First, the gravity-flow of buffer, diluted and whole blood using filters with pores ranging from 8 to 28 μm in diameter was characterized, and flow rates, consistent with predictions, measured. The optimal flow rate and pore size for cCTCs isolation were determined using blood from healthy donors spiked with OV-90 ovarian cancer cells comprising both single cells and clusters. Following a systematic characterization of the cluster morphology, the effect of shear on cluster disaggregation was characterized. Next, blood and ascites from ovarian orthotopic transplanted mice were processed and the number of scCTCs and cCTCs, along with the morphological features and the expression of molecular markers for aggressiveness and EMT were evaluated. Finally, to evaluate the clinical potential of G μ F, blood samples from 30 cancer patients, including 17 EOC with advanced (metastatic) and localized disease (chemo-naïve and post-surgery), and 13 colorectal cancer liver metastasis (CRCLM) patients were processed. The number and size of cCTC events and the proportion of scCTCs vs. cCTCs in the circulation were analyzed.

Results

Gravity-based microfiltration for selective isolation of clustered CTCs

Filter clogging by blood components is expected to increase the pressure and shear stress across the pores under constant flow rate conditions. We reasoned that increased shear would negatively affect the capture of clusters as it could contribute to disrupting or squeezing them through the pores. Thus we adopted gravity-based microfiltration (G μ F), which provides constant pressure with constant total column heights (H_{tot}) of 15, 20, and 30 cm (Figures 1A and S1) (Ripperger et al., 2012). As previously described (Meunier et al., 2016), blood was diluted 1:6 in PBS and an 8 mm-diameter microfilter was clamped in the 3D printed cartridge (Figure 1B). Filters with pores of 8 μm diameter (Table S1) were used initially to characterize flow of G μ F using PBS, diluted blood, and whole blood.

For PBS diluted and whole blood samples, the flow rate was highest at first and quickly decreased during the first seconds to minutes (termed Domain I). For PBS, the flow rate then decreased in concordance with the column height until the end of filtration, (termed Domain II, Figures 1C, S1B and Table S2). For diluted and whole blood, the flow rate then became constant which could last hours (also termed Domain II, Figures 1D and S1C-D). For example, for $H_{\text{tot}} = 20$ cm ($L_1 = 10$ cm), the flow rate in Domain II was ~ 0.09 and ~ 0.02 mL min^{-1} for diluted blood and whole blood, respectively. For both fluids, the flow rate in Domain II varied linearly with H_{tot} . For diluted blood, similar behavior was observed for all filter pore sizes, and calibration curves (Figure S2) allowed the determination of the tube length to use for achieving a specific flow rate (Table S1).

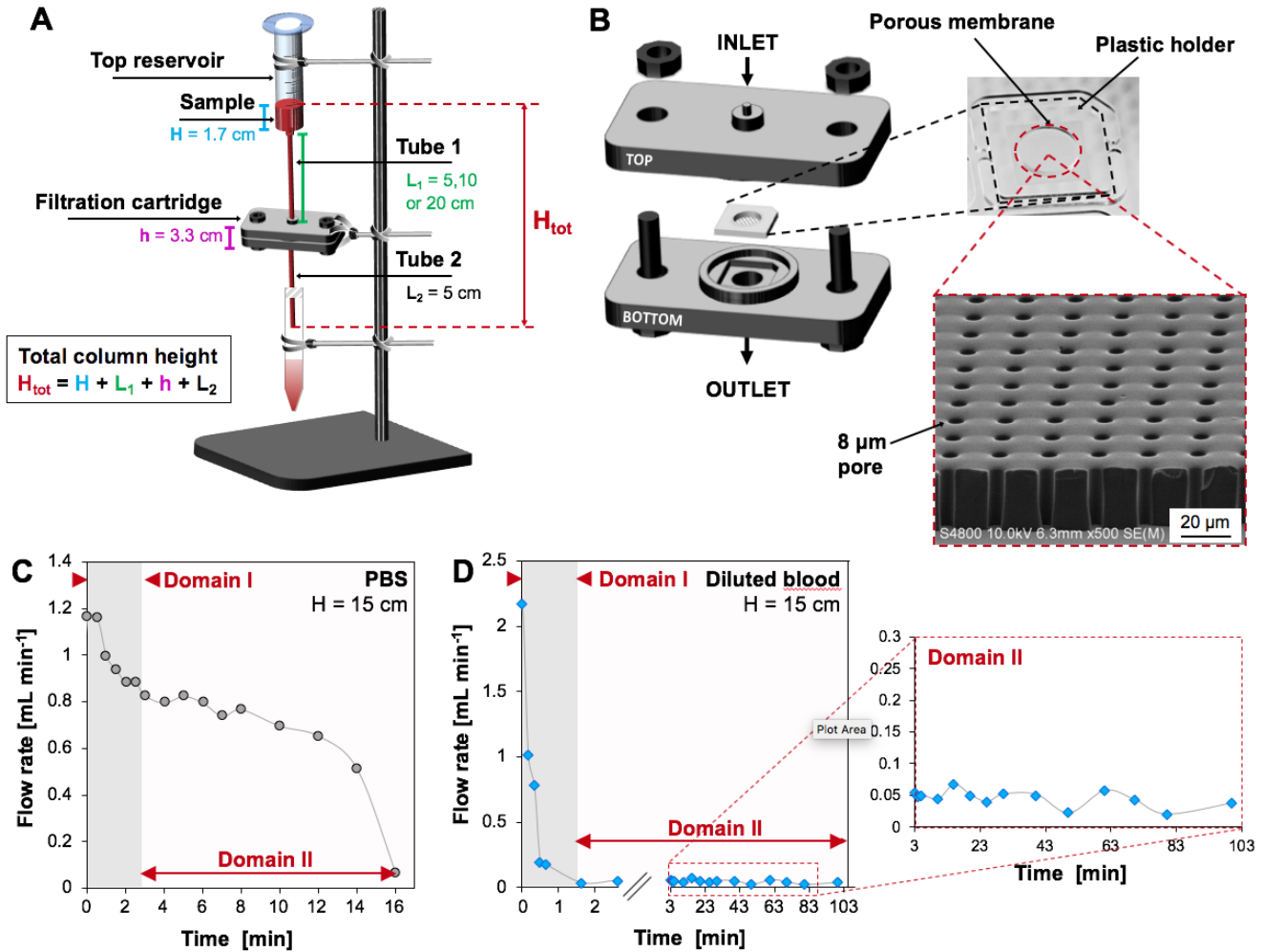


Figure 1. G μ F for CTC enrichment. (A) Schematic of the G μ F set-up. The total column height (H_{tot}) determines the pressure and flow rate when considering the G μ F flow resistance. (B) Exploded view of the filtration cartridge with filter, and close-ups of a polymer filter with 8 μ m diameter pores. (C) and (D) Examples of time course of flow rate for 10 mL of (C) PBS and (D) blood diluted 1:6 in PBS filtered through an 8 μ m filter with H_{tot} = 15 cm, and close-up of domain II (pseudo-steady state) for diluted blood. See also Figures S1 and S2 and Tables S1 and S2.

To assess whether small differences between G μ F and syringe pump driven flow were significant, diluted blood samples were spiked with OV-90 ovarian cancer single cells and clusters, divided into two equal volumes and filtered through 8 μ m filters using both methods: one by G μ F with a tube length L_1 of 12 cm and 66 cm (nominal flow rates of ~ 0.1 and ~ 0.5 mL min⁻¹, Table S1), and the other using a syringe pump with exactly 0.1 and 0.5 mL min⁻¹. For 8- μ m-filters, the calculated shear stress (τ_{max}) was 1.59 Pa

and 5.95 Pa and the transmembrane pressure (ΔP) was 5.2 Pa and 26.1 Pa, respectively (Table S3). After filtration, filters were rinsed with PBS, then cells were stained with DAPI for the nucleus, for epithelial cytokeratin (CK), and for CD45. This panel allowed discrimination of CTCs (CK⁺/CD45⁻/DAPI⁺) from WBCs (CK⁻/CD45⁺/DAPI⁺) (Figure 2A).

The capture efficiency for single cells and clusters showed opposing trends (Figure 2B). When the flow rate increased from 0.1 to 0.5 mL min⁻¹, cluster capture efficiency decreased from ~80% to ~40% for G μ F, and from ~35% to ~25% for pump-controlled flow, while single cell capture increased from 60% to 200% for G μ F, and from 55% to 230% for pump filtration. Percentages over 100% are attributed to the break-up of clusters, which can account for the contradicting trends. These results highlight that G μ F is more efficient at capturing clusters, in both cases, and that increasing the flow rate broke up 50% of clusters for G μ F, and only ~33% of clusters for syringe flow. This discrepancy may be explained by the fact that syringe flow already disrupted clusters at low flow rate.

Next, the size of OV-90 clusters after filtration at a nominal rate of 0.1 mL min⁻¹ for G μ F and syringe pump filtration was compared (Figure 2C). Consistent with cluster breakage, pump filtration showed more 2-cell clusters, but less 3-cell clusters, while 4-cell clusters and larger were essentially absent (~1% of all capture events). Clusters of all sizes were captured by G μ F, and 4-cell clusters and larger collectively accounted for ~30% of all captured events.

Previous optimization showed that the number of clogged pores after filtration and rinsing was negligible (~1%) (Meunier et al., 2016). However, it is most likely that a significant number of WBCs is depleted during the rinse step. The proportion of clogged pore might be higher and vary during filtration. In G μ F, although flow rate remained stable overall in Domain II, the slight fluctuations might reflect pore clogging, which would result in a slight pressure increase with constant flow rate pump filtration and explain the higher breaking rate. At 0.1 mL min⁻¹, the maximum flow speed (v_{\max}) through 8 μ m pores is 827 μ m s⁻¹. For G μ F, v_{\max} remained constant irrespective of pore clogging but increased under constant-flow rate conditions during syringe pump filtration as shown by the FEA in Figure 2D. With 8 μ m filter, for 22% clogging, v_{\max} increased to ~1060 μ m s⁻¹ and the resulting shear stress τ_{\max} from 1.59 to 2.05 (Table S3).

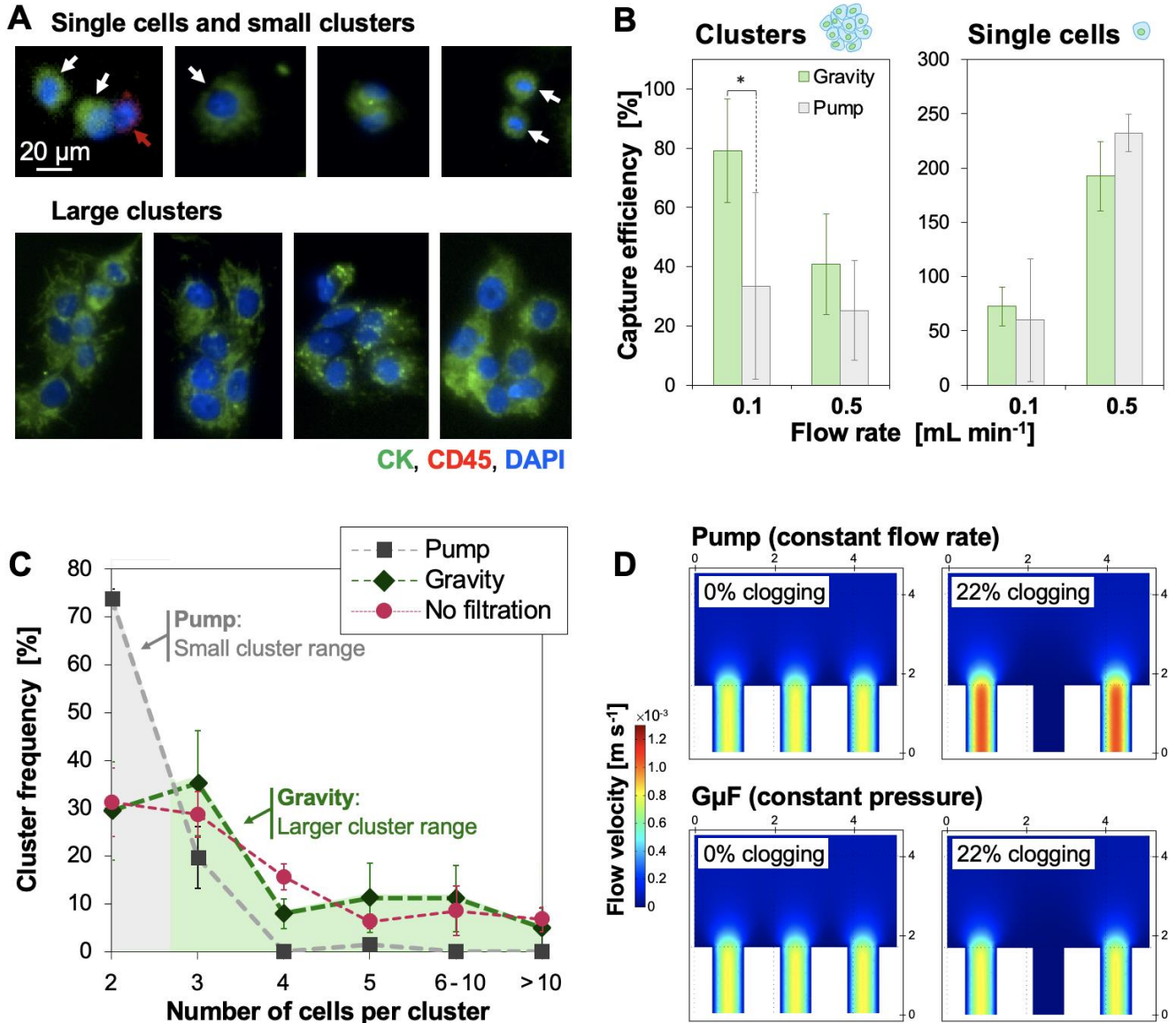


Figure 2. G μ F captured larger clusters than syringe-pump driven flow. (A) Fluorescence images of OV-90 single cells and clusters captured using G μ F and pump filtration using 8 μ m filters. Cells were stained for cytokeratin (green) and CD45 (red). Nuclei were stained with DAPI (blue). Single cells (white arrows), small clusters and WBCs (red arrow) were captured using both configurations. Larger clusters, with > 5-6 cells were only captured with G μ F. (B) Capture efficiency of clusters and single cells for G μ F (green) and pump filtration (grey) at 0.1 and 0.5 mL min⁻¹. (C) Size distribution of the clusters before filtration and captured using G μ F and pump filtration at ~0.1 mL min⁻¹. For each replicate, a known number of OV-90 cells (~120 clusters and ~40 single cells) was spiked in diluted blood. Error bars correspond to the standard deviation of three replicated experiments. (D) Finite-element analysis comparing flow velocity in 8 μ m pores for G μ F and pump filtration at 0.1 mL min⁻¹, for 0% and 22% clogging. See also Tables S1 and S3.

Capture of OV-90 ovarian cancer cell line clusters

Next, again using OV-90 cells, the optimal filter pore size for capturing the largest range of clusters was determined. Following spiking with ~150 single cells and ~100 clusters, each sample was divided into 6 equal aliquots and flowed through filters with 8 μm , 10 μm , 12 μm , 15 μm , 20 μm and 28 μm pores, respectively, using tube length L_1 of 12, 11, 7, 6, 6 and 6 cm ($\sim 0.1 \text{ mL min}^{-1}$) (Figure 3A and 3B). Single OV-90 cells were found on all filters and single cell capture efficiency strongly decreased with increasing pore size, while matching the size distribution of OV-90 cell before filtration, ranging between ~6-50 μm in diameter. ~70% of single cells were captured on 10 μm filters, dropping to ~25% and 2% for 15 and 28 μm filters, respectively. Clusters were also found on all filters, and efficiency also decreased with pore size, but at a different rate and the efficiency was still ~75% for 15 μm pores. Increasing pore size also yielded higher purity, with decreasing number of contaminating WBCs from ~1000 to ~200 WBCs following filtration of 1 mL using 8 μm and 15 μm filters, respectively (Meunier *et al.*, 2016).

Next, diluted blood samples spiked with OV-90 clusters were filtered successively through all filters by order of decreasing porosity and the cluster size distribution on each filter was determined by counting the number of cells they comprised and by measuring their surface area (Figure 3C and S3A). In this repeated filtration, all large clusters, from 6-100+ cells ($> 1200 \mu\text{m}^2$, $\emptyset_{\text{eq}} \sim 40 \mu\text{m}$), were captured on the three first filters with 28, 20 and 15 μm pores. As expected, 28 μm filters allowed for capturing the largest clusters with area $\sim 65000 \mu\text{m}^2$ ($\emptyset_{\text{eq}} \sim 90 \mu\text{m}$) but most of the cluster population was captured on the following 20 μm and 15 μm filters, where cluster with area up to $\sim 2800 \mu\text{m}^2$ and $\sim 5500 \mu\text{m}^2$ were found, respectively. Small pore filters (8, 10, and 12 μm) mostly captured 2- and 3-cell clusters with areas ~ 150 - $300 \mu\text{m}^2$ ($\emptyset_{\text{eq}} \sim 14$ - $19 \mu\text{m}$), that could pass through the preceding larger pore filters. Small clusters were also found on larger pore size filters but to a lesser extent. Interestingly we observed that in small clusters (up to 5-6 cells), the diameter of the biggest cell increased with the pore size (Figure S3B). These results suggest that the capture efficiency of small clusters may not be dictated solely by the size of the cluster, but significantly depends on the size of its largest cell (and more accurately the largest nuclei) in agreement with Toner *et al.* who found that 20-cell clusters could traverse 5-10 μm constrictions in a microfluidic device following an unfolding process (Au *et al.*, 2016).

The 15- μm -filters contained the largest diversity of clusters, while no large clusters were found on the following 12, 10 or 8 μm filters, suggesting that 15 μm filters efficiently capture clusters, and were thus considered optimal. Using 0.1 mL min^{-1} , 15- μm -filters yielded ΔP of 0.61 Pa that resulted in a v_{max} of

340 $\mu\text{m s}^{-1}$ and a τ_{max} of 0.35 Pa, below stress in capillaries (Ballermann et al., 1998) (Tables S3), which provides further support that large clusters can be captured by G μ F without disrupting them.

Release of OV-90 clusters, cluster size distribution and viability

To characterize cell release from the filter, OV-90 single cells and clusters were first stained in suspension, then spiked in diluted blood. Samples were divided into three aliquots. One aliquot was used to determine clusters size distribution before filtration (positive control). The two other aliquots were filtered at 0.1 mL min^{-1} , then cells were released by placing the cartridge upside down and flowing 5 mL of PBS in the reverse direction, either at 0.1 or 1.0 mL min^{-1} , and their size distribution was characterized (Figure 3D).

The average area of clusters before filtration ($795 \pm 82 \mu\text{m}^2$) and after release at 0.1 mL min^{-1} ($974 \pm 57 \mu\text{m}^2$) was comparable, with clusters from $\sim 100 \mu\text{m}^2$ to 5000 and 10000 μm^2 , respectively. Following release at 1.0 mL min^{-1} , average cluster area decreased to $486 \pm 191 \mu\text{m}^2$, and the cluster distribution shrank with a strong increase in small cluster frequency and a significant loss of larger clusters. Clusters smaller than 400 μm^2 represented $23 \pm 6\%$ of the total cluster population before filtration, $16 \pm 7\%$ after release at 0.1 mL min^{-1} , and up to $59 \pm 9\%$ after release at 1 mL min^{-1} . Although high flow rates are likely to help dislodging clusters, release efficiency decreased from $\sim 83\%$ at 0.1 mL min^{-1} to $\sim 60\%$ at 1.0 mL min^{-1} , further highlighting the susceptibility of clusters to shear. At 0.1 mL min^{-1} , G μ F can both capture and release clusters while preserving their integrity.

Cell viability was measured after release from filters using blood samples spiked with ~ 500 OV-90 single cells and clusters (Figure 3E). Dilution, rinsing, and release were performed with complete ovarian surface epithelial (OSE) culture medium, PBS, or fetal bovine serum (FBS) at 4°C and 23°C. A flow rate of 0.1 mL min^{-1} , and filters with 15 μm and 8 μm pores were used to capture clusters and single cells, respectively. Single cells viability varied strongly with temperature; optimal conditions being PBS at 4°C ($75.7 \pm 9.1\%$). Cluster viability was independent of the tested parameters and stable at $\sim 70\text{-}80\%$, exceeding single cell viability in each case, except when using PBS at 4°C which raised single cell viability to the level of that of clusters. The preservation of cell-cell or cell-matrix interactions within clusters could explain their enhanced viability, and the lower effect of temperature compared to single cells. The loss of interaction with the extracellular matrix during shedding from the tumor induces activation of anoikis (Frisch and Francis, 1994), and low temperature could slow down cell death mechanisms, thus accounting for increased single cell viability. As a positive control, cells were simply

incubated for 5h at 37°C in low-adhesion dishes and the viability was similar to that of cells released after G μ F, indicating that neither single cell nor cluster viability were negatively affected by the G μ F process. The full process from capture to release lasts ~5 h, and cluster viability was ~75%, and might be further increased by reducing filtration time by using filters with larger diameters.

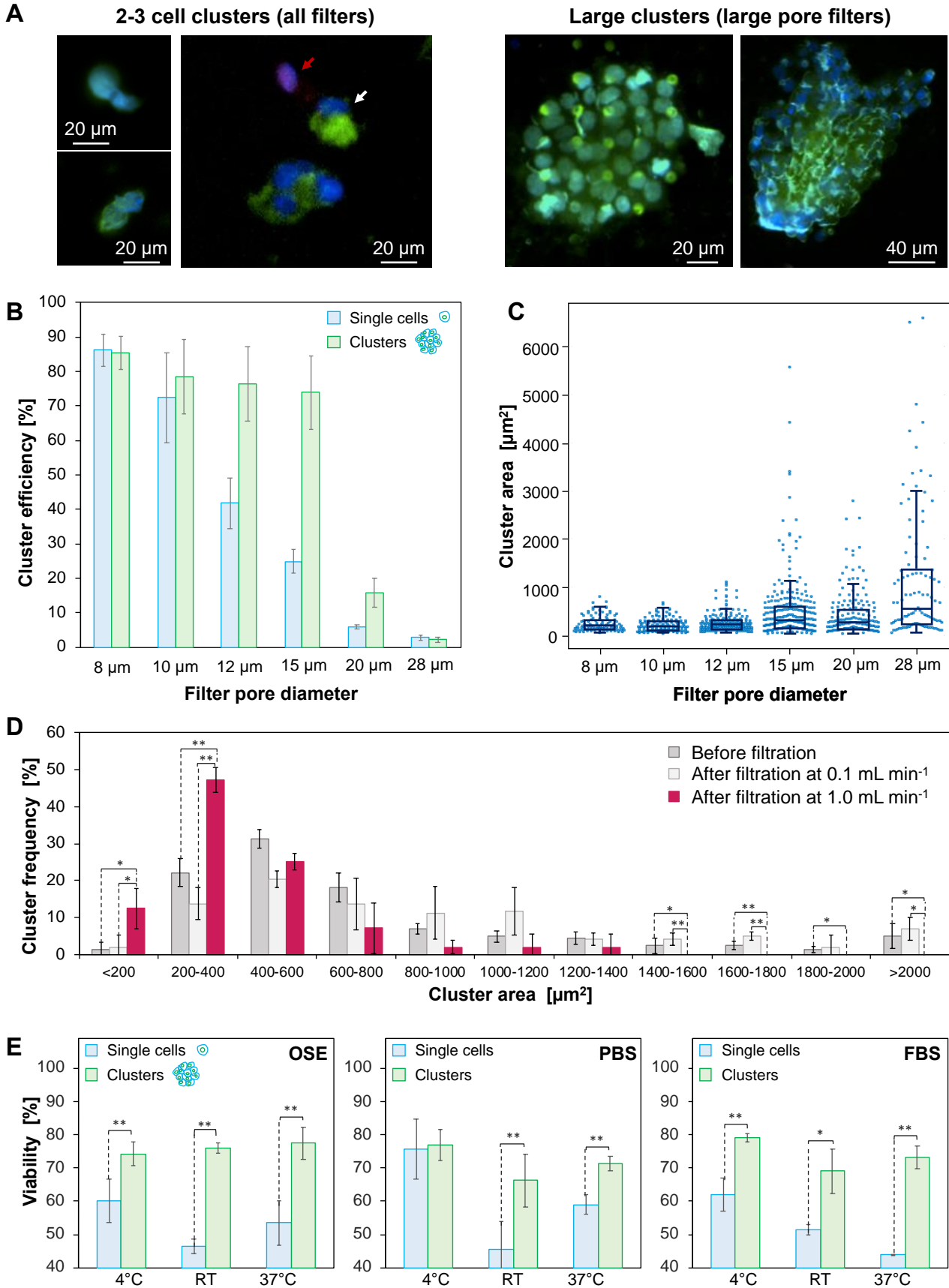


Figure 3. Characterization of clusters captured by G μ F. (A) Fluorescence images of representative large and small clusters. Cells were stained for CK (green), CD45 (red) and with DAPI (blue). CTC-like cells (white arrow) are CK⁺/CD45⁻/DAPI⁺ and WBCs (red arrow) are CK⁻/CD45⁺/DAPI⁺. (B) Capture efficiency depending on pore size, measured with OV-90 single cells (blue) and clusters (green) spiked in diluted blood. (C) Scatterplot and box plot of the size distribution of clusters captured by serial G μ F through filters with decreasing pore size (28, 20, 15, 12, 10 and 8 μ m) for three replicated experiments (n = 145, 300 and 550 spiked clusters). The boxes range from 25th and 75th percentiles, the whiskers correspond to 91st and 9th percentiles, and the horizontal lines represent the medians. (D) Cluster size distribution before filtration (dark grey, n = 80, 39 and 37) and after filtration at 0.1 ml min⁻¹ and release by flowing PBS at either at 0.1 mL min⁻¹ (light grey, n = 61, 30 and 35) or 1 mL min⁻¹ (red, n = 37, 31 and 19). (E) Viability of single cells (blue) and clusters (green) after filtration, rinsing, and release using complete OSE culture medium, PBS, or FBS at 4°C, at RT (22-23°C), and after 5 h incubation in low adhesion plates (no processing) at 37°C. Error bars correspond to the standard deviation of three replicated experiments. p < 0.01: **; p < 0.05: *. See also Figure S3.

Capture of circulating tumor cell clusters (cCTCs) from mouse blood

G μ F was tested with blood from ovarian orthotopic mouse models after injecting OV-90 or OVCAR-3 cells, with high and low invasive potential (Provencher et al., 2000), respectively, and collecting their blood after sacrifice. Orthotopic xenograft results in spontaneous metastasis that closely mimic dissemination from the primary tumor in human cancers (Lengyel et al., 2014), thus recapitulating early events in disease progression. Half of each sample was saved for growth analysis, while the other half was filtered using 8 μ m filters to capture the gamut of scCTCs and cCTCs. From the blood of three OV-90 mice, 505/5, 259/9 and 582/4 scCTCs/cCTCs were captured, cCTCs thus accounting for < 5% of the total CTC population, in agreement with published results (Aceto et al., 2014). cCTCs with size between 2-100+ cells were found in every mouse.

Next, blood from a single OVCAR-3-GFP (green fluorescent protein) mouse was diluted and divided into four identical aliquots. One quarter was saved for further growth analysis, and the three others filtered through 15 μ m filters at 0.1 mL min⁻¹. Respectively 55, 40, and 49 cCTCs were found in each replicate, falling well within the variation expected based on Poisson statistics alone. The size of cCTCs again varied from 2-100+ cells, their frequency was highest for small clusters, with 2-cell and 3-cell clusters representing 27-33% and 5-12% of all cCTC events, respectively, and the larger clusters were rarer, with consistent results across the triplicates (Figure 4A and 4B). cCTCs as big as 30000-35000 μ m² (\emptyset_{eq} ~0.6 mm) were captured directly from the mouse's bloodstream, consistent with previous

observations of large cCTC aggregates in blood (Au et al., 2016). These results give us high confidence in the reproducibility and performance of GµF to isolate cCTCs spontaneously formed *in vivo*.

The blood samples of OV-90 and OVCAR-3-GFP saved for growth analysis were filtered through 15 µm filters, and the cCTCs were released and cultured in regular and low-adhesion culture flasks at 37°C. Both OV-90 and OVCAR-3-GFP cCTCs adhered and spread after a few hours in adherent flasks forming confluent layers after 7-8 days. Migration assays revealed similar growth behaviors for both cell lines, where a full coverage of the cell-free area was reached after 6 days (Figure S4A-D). In low adhesion flasks, OV-90 and OVCAR-3-GFP cCTCs growth also occurred in suspension. After 7 days of incubation, the cluster average diameter increased from 1500-2000 µm² (\emptyset_{eq} ~40-50 µm) at day zero for both cell lines, to ~6000 and ~15500 µm² for OVCAR-3-GFP and OV-90, respectively (Figure 4C). Both cell lines exhibited a broad cluster size distribution (Figure S4E-G) with cCTCs from 160 to more than 20000 µm²; OV-90 clusters were larger than OVCAR-3-GFP however, in agreement with a higher invasive phenotype. After day 2, OV-90 clusters kept increasing in size while OVCAR-3-GFP plateaued and at the same time a significant number of dying OVCAR-3-GFP was observed, likely due to a higher sensitivity of OVCAR-3 clusters to hypoxic conditions in the core.

cCTCs can help understand dissemination in ovarian cancer

In EOC, Snail, a zinc finger transcription repressor, can activate zinc finger E-box-binding homeobox 1 (ZEB-1) that induce the loss of adhesion proteins such as E-cadherin (E-Cad) (Cano et al., 2000) and zonula occludens-1 (ZO-1) (Polette et al., 2007). As in many cancers, cell adhesion plays a critical role in the dissemination of EOC, and notably, the loss of E-Cad and ZO-1 (Polette et al., 2007) was correlated with disease aggressiveness by promoting tumor growth, invasiveness, and resistance to chemotherapy (Haslehurst et al., 2012, Wang et al., 2015). cCTCs were isolated from the blood of two OV-90 and two OVCAR-3 mice, as well as from the ascites of one of the OVCAR-3 mice. After release, cCTCs were stained for aggressiveness markers: E-Cad, ZO-1, ZEB-1 and Snail (Figure 4D and 4E). cCTCs from ascites and blood had not yet been compared to the best of our knowledge, and interestingly, different phenotypes were dominant in each sample. OV-90 cCTCs from blood strongly expressed ZO-1, ZEB-1 and Snail, but exhibited extremely low levels of E-Cad. OVCAR-3 cCTCs captured from blood also displayed a weak expression of E-Cad but lower expression of ZO-1, ZEB-1 and Snail, consistent with a less aggressive behavior. OVCAR-3 cCTCs from ascites exhibited significantly lower levels of ZO-1, ZEB-1 and Snail than OV-90 cells from blood, but in the same range or slightly higher than OVCAR-3

cCTCs from blood of the same mouse. In all samples, cCTCs were strongly heterogeneous with variable levels of epithelial markers. Additional staining for the mesenchymal marker vimentin (Vim) (Pantel and Speicher, 2016), showed that blood OV-90 cCTCs exhibited a pronounced mesenchymal phenotype with low E-Cad and high Vim levels (Figure 4F). Blood and ascites OVCAR-3 cCTCs displayed a hybrid epithelial/mesenchymal (E/M) phenotype, each individual cell co-expressing epithelial and mesenchymal markers. These results support the contribution of EMT in cCTCs dissemination and confirm the potential of G μ F for molecular and functional analysis of living cCTCs.

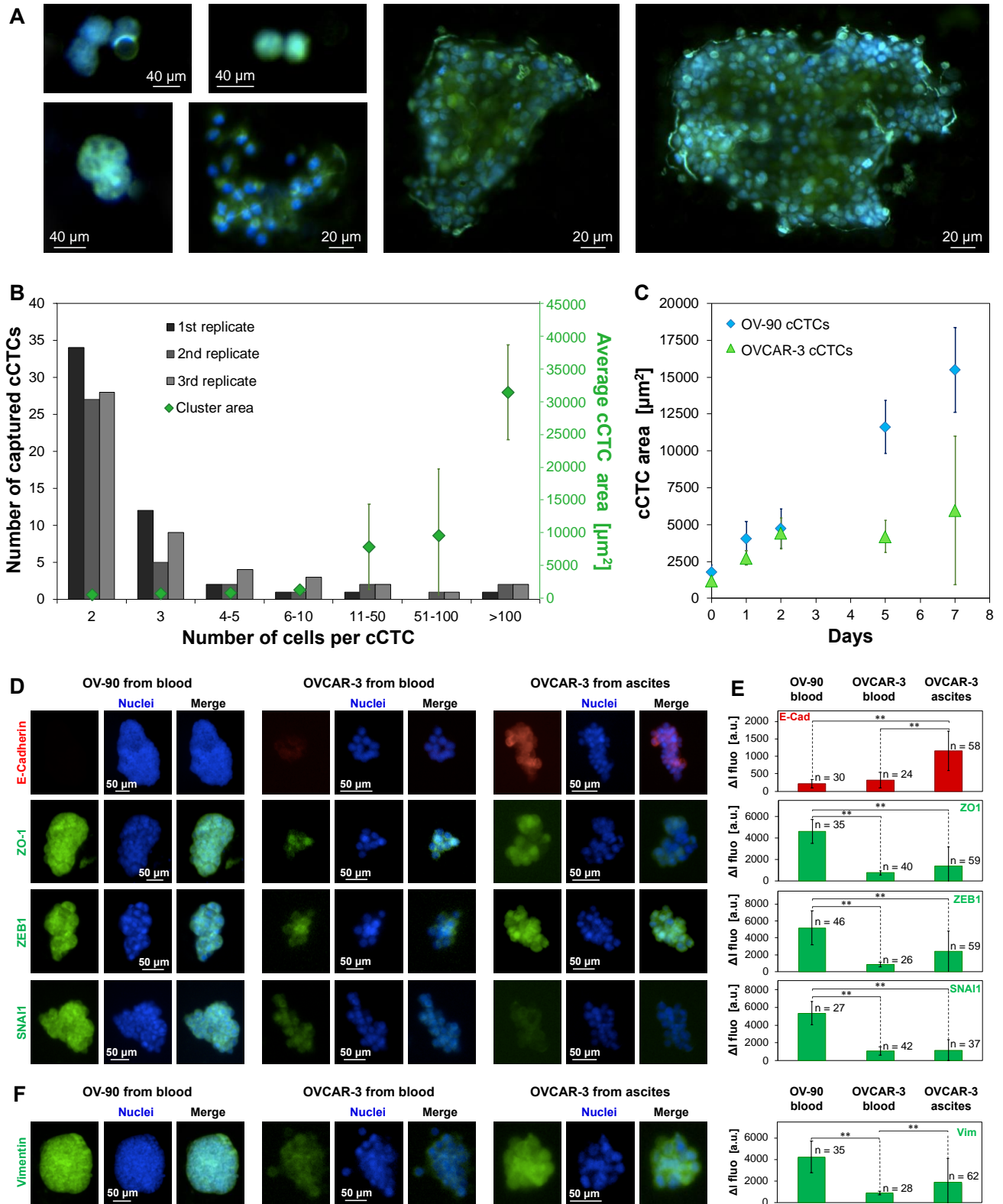


Figure 4. cCTCs captured from mouse. A. Examples of fluorescence images of OVCAR-3-GFP cCTCs captured from mouse blood. Nuclei were stained with DAPI. **B.** Size distribution of the OVCAR-3-GFP cCTCs captured in three replicates from a single mouse. cCTC area is averaged over three replicates. **C.** Evolution of the average area

of OV-90 and OVCAR-3-GFP cCTCs overtime during incubation in low adhesion culture flasks. Error bars correspond to the standard deviation of three replicated experiments. **D.** Fluorescence images of OV-90 cCTCs captured from mice blood, and OVCAR-3 cCTCs from the blood and ascites of the same mouse. cCTCs were stained for aggressiveness markers E-Cad, ZO-1, ZEB1 and Snail. Nuclei were stained with DAPI. **E.** Expression levels of E-Cad, ZO-1, ZEB-1 and Snail in OV-90 and OVCAR-3 cCTCs from blood or ascites with indication of statistical significance. **F.** Additional staining for mesenchymal Vim. OVCAR-3 cCTCs from blood and ascites exhibit a hybrid E/M phenotype. Error bars correspond to the standard deviation between cCTCs. See also Figure S4.

Capture of cCTCs from cancer patients

To show the generality of G μ F, we used it to enrich CTCs from the blood of 17 EOC (Supplementary Table S4) as well as 13 CRCLM (Supplementary Table S5) patients. EOC patients included 10 high-grade serous carcinoma (OC1-OC10) with samples taken both before and after chemotherapy, and 7 other histological subtypes of EOC, at lower stage, and all taken before chemotherapy (OC11-17). Of the 13 CRCLM patients, 4 were treatment naïve and 9 had undergone chemotherapy.

The blood samples were processed by filtering first with 15 μ m followed by 8 μ m filters to capture CTCs. scCTCs and cCTCs were found in every sample, with different relative frequency for each patient. For EOC patients with high-grade serous carcinoma (Figure 5A), the number of scCTCs per mL of blood varied from 22 (OC4) to 584 (OC9), and the number of cCTCs from 1 (OC4) to 62 (OC1). For patients with good response after several cycles of chemotherapy, as indicated by low CA125 levels (Supplementary Table S4), the proportion of cCTCs events was lower, varying from ~4% (OC2) to ~8% (OC5). For OC1 (before chemotherapy), cCTCs represented up to ~30% of all CTCs capture events. For patients with other types of EOC at lower stage (Figure 5B), the number of scCTCs per mL of blood varied from 25 (OC14) to 210 (OC16), and the number of cCTCs per mL ranged from 1 (OC15) to 45 (OC11), and cCTCs represented from ~1% (OC15) to ~39% (OC17) of all CTC events. For CRCLM patients, the number of scCTCs per mL of blood varied from 4 (CR2) to 99 (CR10), and the number of cCTCs from 1 (CR1, 2, 8) to 30 (CR12). cCTCs were found in \leq 10% of all CTC capture events for patients CR7-CR10, 17-27% in CR1-CR6, and \geq 30% for CR11-13, with no apparent correlation with chemotherapy treatment. Note that the size of the tumor was not available.

To better understand the relative contribution of cCTCs and scCTCs, the number of cells captured as cCTCs was quantified by counting the number of cells in each cluster. The high transparency and low autofluorescence of the filters allowed us to precisely determine the number of cells for small clusters

and estimate it for large clusters. In high-grade serous carcinoma (Figure 5D), cells in clusters represented up to ~71% of all CTCs in case of OC1, and was significantly lower for patients having followed several cycles of chemotherapy, varying from ~12% (OC2) to ~17% (OC5). For patients with low stage EOC (Figure 5E) and no chemotherapy, the proportion of cells in clusters varied from ~13% (OC15) to ~82% (OC11). Overall, in 11/17 patients, cells in clusters corresponded to >15% of all CTCs, while they represented the majority of CTCs in 4/17 patients (OC1, 8, 11 and 66). Collectively, these results reveal an unexpected prevalence of cCTCs in patients with various histological subtypes of ovarian cancers, at both high and low stage.

In high-grade serous carcinoma, the size distribution of cCTCs varied from 2-50 cells (Figure 5G). In patients receiving therapy (OC1 at T₁-T₃, OC2-5) small cCTCs with 2 cells were the most frequent, corresponding to 50-90% of all cCTC events. 3-5 cells were found in 5/5 patients (10-50% of all cCTC events); and clusters with more than 11 cells were only found in OC1 and OC2. In patients who did not receive chemotherapy, small clusters with 2 cells were the most prevalent, corresponding to 53-100% of all cCTC events, except for OC1(at T₀) and OC9 presenting 2-cell clusters in 19% and 37% of all cCTC events, respectively. In these two patients, clusters with 5 or fewer cells were still the most frequent prior to chemotherapy, representing 62% and 98% of all cCTC events, respectively. In patients with other EOC at lower stage and no chemotherapy, the size distribution of cCTCs varied from 2-100+ cells (Figure 5H), mirroring the one observed in mice. For OC11 and OC17, with endometrioid carcinoma, clusters of up to 3 cells represented 43% and 84% of all cCTCs, respectively. For OC11, clusters with more than 4 cells represented 57%, including clusters with more than 50 and 100 cells. For OC12 and OC13 with clear-cell adenocarcinoma, OC14 and OC15 with mucinous disease, and OC16 with low-grade ovarian carcinoma, small clusters (2-3 cells) were the most frequent, representing 83-100% of all cCTCs events. No cluster larger than 3 cells were found in OC15 (borderline), and cluster larger than 6 cells were found in OC12, OC16 and OC17 and represented 2-10% of all cCTCs.

All cCTCs in CRCLM patients were less than 10 cells, except for CR1 with 1 cCTC of > 10 cells. In chemo-naïve patients, cCTCs of 2-3 cells were the most prevalent, corresponding to 79-88% of all cCTC events (CR7, CR12 and CR13), except for CR1 presenting only cCTC of 4 cells or more, with cCTCs between 4 and 10 cells in 83% of total cCTC events. In CRCLM patients who underwent chemotherapy, cCTCs of 2-3 cells represent 78%-100% of all cCTC events. There is no apparent correlation between cCTC size and chemotherapy cycles in this small cohort.

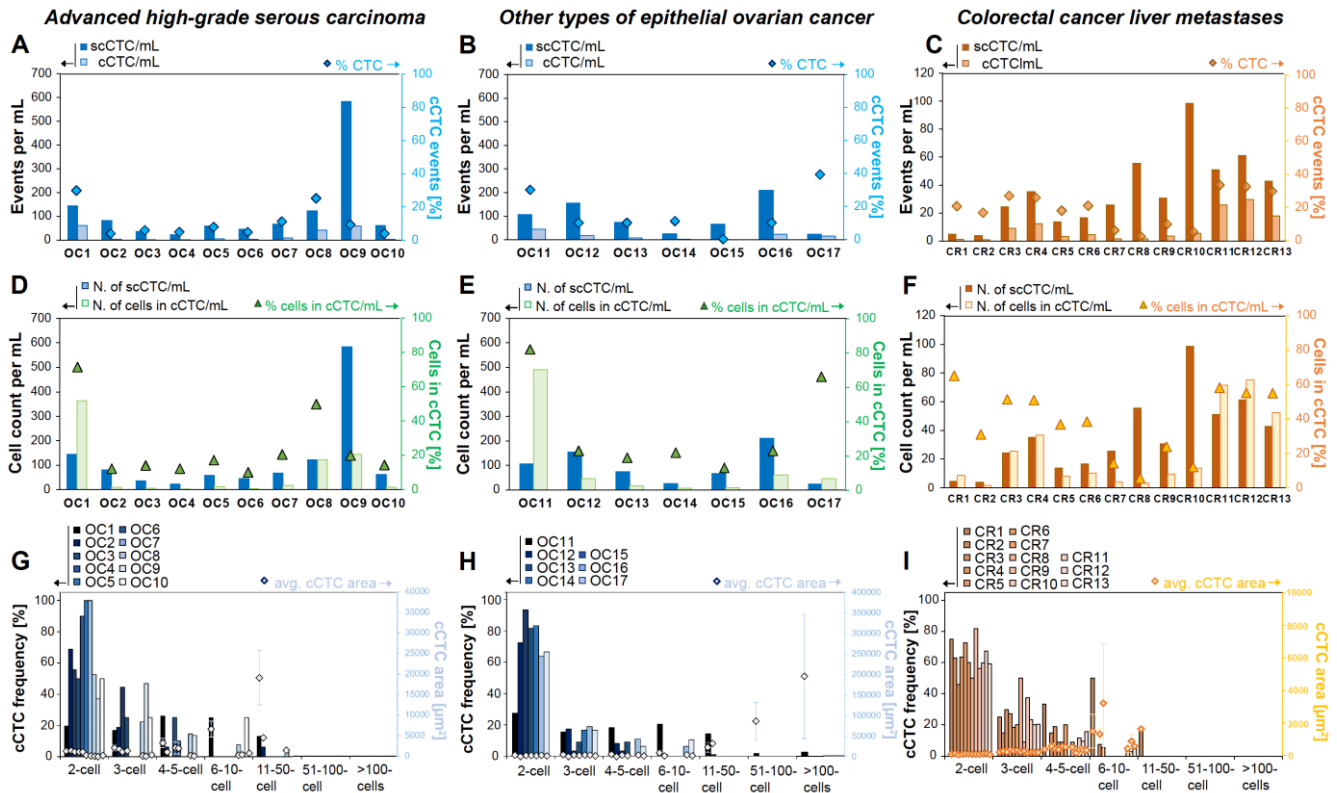


Figure 5. Count and morphological characterization of CTCs captured from the blood of EOC and CRCLM patients. (A-C) Concentration of scCTCs and cCTCs in the blood of patients OC1 to OC17 and CR1 to CR13. The diamonds represent the frequency of cCTC events. (D-F) Number of scCTCs and of cells in cCTCs per milliliter of blood, in each patient sample. The triangles correspond to the percentage of cells in cCTCs vs. all CTCs. (G-I) Size distribution of cCTCs captured from the blood of OC1 to OC17 and CR1 to CR13. The area covered by cCTC clusters is provided (dots) on an indicative basis. Error bars correspond to the standard deviation between cCTC within the cell number bin in each patient.

Differential reduction of scCTC and cCTC during treatment of metastatic EOC high grade serous carcinoma patient

A time-course study was conducted for OC1 by collecting blood sample during the course of chemotherapy (Figure 6A). The concentration of CA125 in blood was used to track response to therapy and levels below the cut-off at 35 U mL^{-1} indicate a good response. The CA125 level of OC1 was reduced from $>2000 \text{ U mL}^{-1}$ at diagnosis to $\sim 50 \text{ U mL}^{-1}$ after surgery and further decreased over the first three cycles of chemotherapy, plateauing at $\sim 10 \text{ U mL}^{-1}$. CTCs analysis was performed at four times points: after surgery and before chemotherapy (T_0), after the first cycle of chemotherapy (T_1), a few days before the third cycle of chemotherapy (T_2), and post treatment (T_3); no pre-surgery samples were available for CTC isolation (Supplementary Table S4). The number of scCTCs and cCTCs was stable between T_0 and

T₁, with ~140 scCTCs and ~60 cCTCs per milliliter. Then, both scCTCs and cCTCs decreased in number as therapy progressed, but followed different trajectories. The number of scCTCs initially remained similar until the third cycle of chemotherapy, with 132 scCTCs per mL at T₂, then decreased to 11 after 6 cycles of chemotherapy (T₃). The number of cCTCs decreased from 62 to 2 in a gradual manner. Thus, while the CA125 level stopped changing after 3 cycles, the number of scCTCs and cCTCs continued dropping.

Cluster size distribution was determined at the four time points (Figure 6B). Before chemotherapy (T₀) and after the first cycle (T₁), cCTC size distribution was similar, respectively with 36% and 42% of cCTCs with 2-3 cells, 52% and 38% of cCTCs with 4-10 cells, 12% and 16% of cCTCs with 11-50 cells. No cCTCs larger than 50 cells were captured at T₀, and, at T₁, clusters with 50-100+ cells corresponded to ~4% of all cCTCs. This small increase in the number of large clusters between T₀ and T₁ is likely due to sampling variability as small blood volume were processed (3-4 mL), and larger clinical study would help determine its significance. Then, after the second cycle of chemotherapy (T₂), in addition to the strong reduction in the number of cCTCs, the cCTCs size was significantly reduced, with the majority (~94%) of cCTCs with 2-5 cells and only 1 cCTC with more than 11 cells. Finally, post-treatment (T₃), only 2- and 3-cells clusters were captured. After the second cycle of chemotherapy (T₂) and, to a much greater extent after the last cycle (T₃), membrane blebbing and leakage of the cell contents was observed suggesting increased death of the cCTCs (Figure 6C). Together, these results indicate that chemotherapy may affect both the number and the size of cCTCs.

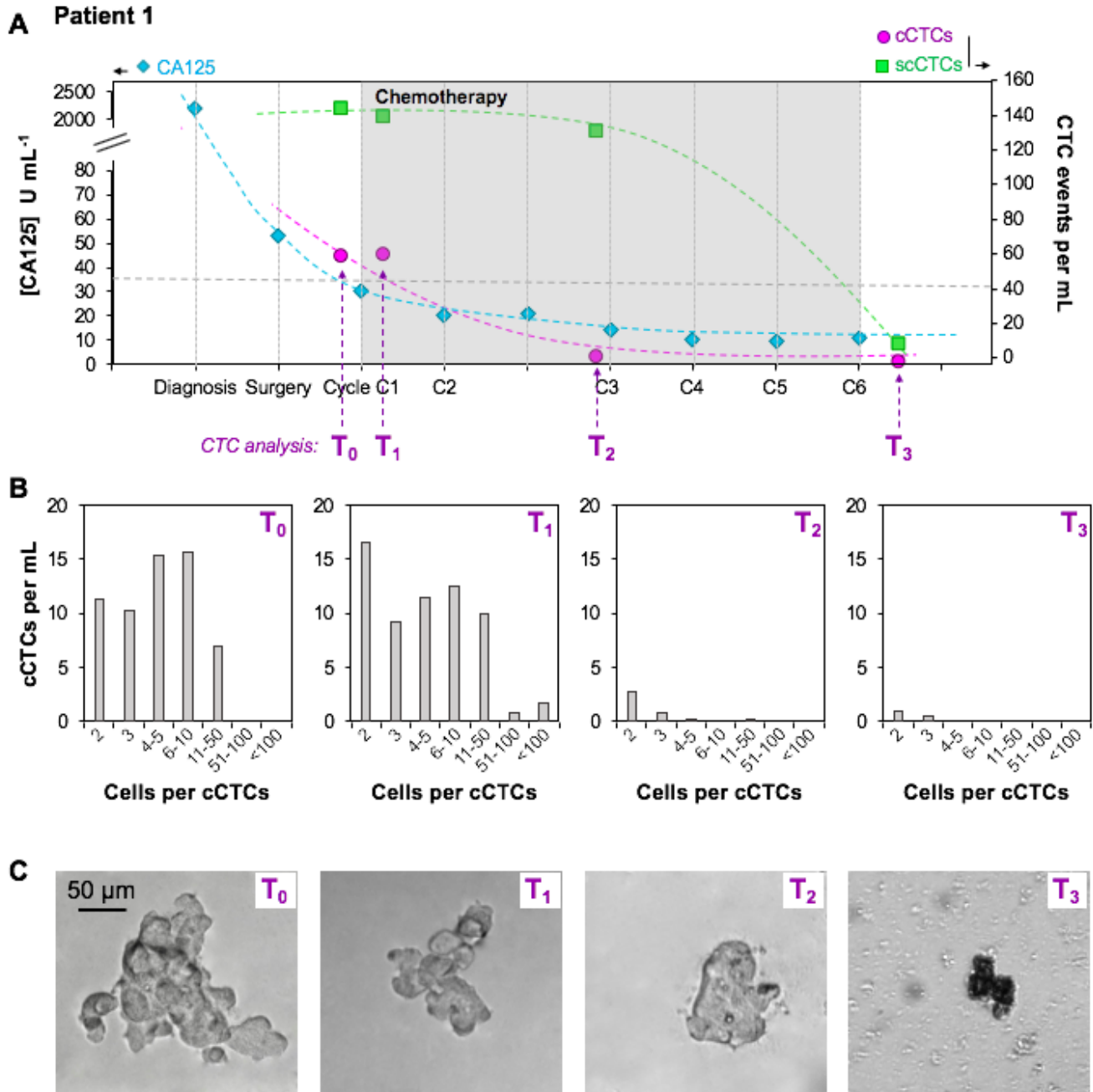


Figure 6. Time-course study for one metastatic EOC high grade serous carcinoma patient. A. Time course study for P1 who responded to therapy, showing the CA125 concentration as well as the number of scCTC and cCTC events per mL of blood at different time points during chemotherapy. **B.** cCTCs size distribution and **C.** representative bright field images of cCTCs captured from the blood of P1 at four time points during follow-up.

Discussion

G μ F using filters with 8 mm diameter and 15 μ m pores for enriching cCTCs, and 8 μ m pores for capturing the cCTCs that slipped through the large filters and scCTCs, is an effective method for capturing and selectively enriching the compendium of single cell CTCs and fragile clusters. Microfiltration was among the very first methods used to capture rare CTCs (Fleischer *et al.*, 1964, Seal, 1964), and whereas several applications for scCTC isolation were successfully developed (Adams *et al.*, 2014, Tang *et al.*, 2014, Lim *et al.*, 2012), its use for cCTCs had not been widely explored. Sarioglu *et al.* recently tested cCTCs isolation with low porosity (< 5%) track-etched membranes with 5 μ m pores, but recovered only ~36% of spiked cCTCs at 0.07 mL min⁻¹ (Sarioglu *et al.*, 2015). We ascribe the high capture yield of cCTCs to higher porosity filters (up to 40%), gravity (pressure) driven flow, larger pores, and painstaking optimization.

G μ F with 15 μ m-pore filters and a flow rate of 0.1 mL min⁻¹ (corresponding to a Δ P of 0.61 Pa, a v_{\max} of 340 μ m s⁻¹, and a shear τ of 0.35 Pa) were found to be optimal for microfiltration in buffer. The velocity and shear in the pores is below the velocity (0.5-1.5 mm s⁻¹) (Arfors *et al.*, 1975) and shear (0.5-2 Pa) (Ballermann *et al.*, 1998) of blood capillaries. Unexpectedly, we achieved a higher cluster recovery rate with G μ F vs constant-flow with ~80% vs. only ~30%, respectively 8 μ m filters while using the same nominal flow rate of 0.1 mL min⁻¹ (Figure 2), and which we cannot explain. To gain better understanding, we determined the number of single cells and clusters and assessed the size distribution of OV-90 clusters spiked in blood, before and after filtration, which had not been studied previously to our knowledge. When the flow rate was 0.5 mL min⁻¹, this analysis revealed twice as many single cells after filtration than were initially spiked into the sample, which we attributed to shear-driven cluster breakup. The cellular context bears significance in most cancers, and the shear forces in many commonly used isolation techniques are high enough to disrupt cCTCs. Hence, the analysis of the cluster number and size before and after filtration is necessary to assess the impact of a particular filtration method on cCTC breakup, and total counts of cCTCs and scCTCs. During detachment from 15- μ m-filters using flow reversal, higher flow rates increased the number of small clusters but reduced the apparent cluster release efficiency (~60% at 1.0 mL min⁻¹ vs. ~85% at 0.1 mL min⁻¹), which again can be attributed to cluster break-up due to shear. A flow rate of 0.1 mL min⁻¹ was thus deemed optimal for both capture and release of clusters with our setup.

The cluster capture efficiency for filters with pore sizes from 28 to 8 μ m was characterized by sequentially filtering the same blood sample spiked with OV-90 clusters through filters with decreasing

pore size and was found higher for pore sizes of 8-15 μm (Figure 3). The deformability and the large size distribution of both single cells and clusters limit the selectivity of size-based sorting. For example, small clusters squeezed through pores smaller than their nominal size, consistent with results by Toner and colleagues (Au *et al.*, 2016). With 15 μm filters, we recovered $\sim 75\%$ of all clusters from blood, and $\sim 85\%$ of captured clusters could be released, and confirmed that the cluster size distribution was the same before and after G μ F.

To evaluate the potential for G μ F for clinical use, 2.5-4 mL of blood from 30 patients, including 17 EOC (12 advanced metastatic stage and 5 early stage) and 13 CRCLM were processed using 15- μm followed by 8- μm -filters, allowing $>85\%$ recovery of both scCTCs and cCTCs. Whereas scCTCs are commonly isolated, the capture of cCTCs remains a rare occurrence, and were previously isolated from patients with metastatic cancer, but only observed in 5-40% of the samples. For example a study using the herringbone-chip (HB-Chip) identified cCTCs in 3/19 patients with metastatic prostate or lung cancer (Stott *et al.*, 2010). Using Dean Flow Fractionation, Hou *et al.* found cCTCs in 1/20 patients with metastatic lung cancer (Hou *et al.*, 2013). Wang *et al.* found cCTCs in 21/107 patients with metastatic breast cancer at baseline and in 19/77 patients at the first follow-up visit (Wang *et al.*, 2017). Using the Cluster-Chip, cCTCs were found in 30-40% of patients with metastatic breast, skin or prostate cancer, which constitutes the highest reported yield to date (Sarioglu *et al.*, 2015). In our study using G μ F, both scCTCs and cCTCs were isolated from every patient whether with CRCLM or EOC, which for the latter included patients with metastatic, localized, or borderline disease. Furthermore, samples from three castrate-resistant prostate and one kidney cancer patients, all metastatic, were processed by G μ F, and again, cCTCs found in every sample (as well as in the urine from the kidney cancer patient, results not shown). Taken together, these results suggest that (i) G μ F is able to isolate cCTCs with high sensitivity, (ii) the current estimates of cCTC (and possibly of scCTCs) constitute a lower bound that is biased by technological limitations, and that (iii) cCTC may in fact be widely prevalent in a number of and metastatic and non-metastatic cancers based on the observations made with EOC patients

G μ F using both 15 μm and 8 μm filters allowed to capture a broad range of CTCs from the blood of cancer patients. cCTCs from 2-100+ cells were captured, and small clusters, with 2-3 cells, were the most prevalent, representing from $\sim 35\%$ to $\sim 95\%$ of all clusters captured. EOC had the largest clusters, and both patient samples and mouse models found very large cCTCs occupying up to 350,000 μm^2 on the microfilters, or ~ 400 pores on a 15- μm -filter, indicating that cCTCs can reach large sizes, consistent with other studies (Lecharpentier *et al.*, 2011, Pantel and Speicher, 2016, Yu *et al.*, 2013). cCTCs across a

wider range were captured by G μ F and with a higher yield than was previously reported. Indeed, cCTCs with 4-12 cells were captured with the HB-Chip (Stott *et al.*, 2010); 99% recovery for MDA-MB-231 clusters with more than 4 cells, but only 41% for 2-cell clusters were reported for the Cluster-Chip (Sarioglu *et al.*, 2015); the ^{neg}CTC-iChip was described as favoring the capture of small clusters and cCTCs with 2-6 cells were isolated from metastatic breast and prostate cancer patients (Ozkumur *et al.*, 2013). Aceto *et al.* established the metastatic potential of cCTCs being 23- to 50-time the one of scCTCs based on the ratio of scCTCs *vs.* cCTCs captured using the HB-Chip from mouse blood. However, the HB-Chip appears less effective than G μ F or the Cluster-chip for capturing cCTCs. Hence the number of cCTCs may have been underestimated and by extension the metastatic potential of cCTCs, overestimated.

The systematic analysis of the number of cells per clusters allowed us to account for the total number of CTCs circulating as cCTCs *vs.* scCTCs. Typically, ~10-25% of CTCs were circulating as cCTCs, but in 10/30 patients most CTCs were not circulating as scCTCs, but as cCTCs. These results challenge two widely held notions, namely (i) that scCTCs represent the great majority of CTCs, and that (ii) cCTCs are rare considering in two patients they covered the majority of cancer cells in circulation and were found with a frequency of ~45-60 cCTCs mL⁻¹.

In EOC, the initial response to therapy is generally good and can be traced by monitoring the CA125 drop in concentration in the blood. Relapse often occurs within 6-24 months, but we are currently lacking predictive blood biomarkers. In our small study, G μ F revealed interesting differences among patients. The number of scCTCs, cCTCs, and the size of cCTCs were significantly lower for patients having followed several cycles of chemotherapy. Five patients (OC1-OC5) with serous cystadenocarcinoma (all metastatic) were analyzed. In one case (OC1) multiple blood samples were collected and processed before and during chemotherapy, and the time course of CTCs was compared to CA125. cCTC numbers were found to fall after the third chemotherapy cycle, mirroring CA125 concentration, but interestingly, the number of scCTCs remained stable and only dropped after the 6th chemotherapy cycle. Thus, in line with previous observations supporting that CTC phenotype correlates with disease progression and recurrence in breast cancer (Yu *et al.*, 2013), these results suggest that scCTCs and cCTCs could complement CA125 as an independent measure of response to therapy. The detection of CTCs in non-metastatic patients by G μ F suggests also possible application to early diagnosis, which is supported by a study by Guo *et al.*, who found CTC counts to be more sensitive than CA125 to identify patients at high risk for ovarian cancer (Guo *et al.*, 2018).

In conclusion, optimized G μ F is a simple yet powerful method for isolating scCTCs and notably cCTCs that are easily fragmented, but preserved thanks to gentle processing conditions. Spiked cCTCs were captured with ~85% yield and released with 85% yield (combined yield 72%). cCTCs collected from patients and mouse models comprised between two to over one hundred cells. Our pilot study with 30 patients (17 EOC, including 5 non-metastatic ones, and 13 CRCLM), found cCTCs in every patient and in one third of the patients more cells were circulating as cCTCs than scCTCs. These results challenge commonly held notions that (i) cCTCs are only found rarely, (ii) only in low numbers, and (iii) constitute only a small fraction relative to scCTCs. To allow comparison between different studies and methods, the capture yield for scCTCs and cCTCs, cluster break-up, size distribution and composition of cCTC will need to be characterized. Effective isolation of cCTCs along with scCTCs will allow studying their respective role in disease progression and metastasis, and their collective potential as surrogate biomarkers for diagnosis, prognosis and therapy monitoring.

Acknowledgments

We acknowledge funding from the Canadian Institutes of Health Research (CIHR), as well as from the National Science and Engineering Research Council of Canada (NSERC) as part of the CHRP program (#446671-13). D.J. acknowledges support from Canada Research Chair (CRC). J.A.H.-C. thanks the Lloyd Carr-Harris Foundation and CONACyT for fellowships. L.M., FRQS research scholar, thanks the CIHR for financial support. A-M.M.-M. and D.P., researchers of the Centre de recherche du Centre Hospitalier de l'Université de Montréal, thank the FRQS and the Institut du Cancer de Montréal, and B.P. thanks the Institut TransMedTech for financial support. Tumor banking was supported by the Banque de tissus et données of the Réseau de recherche sur le cancer (RCC) of the Fond de recherche du Québec – Santé (FRQS), associated with the Canadian Tumor Repository Network (CTRNet). We would also like to acknowledge the MUHC Liver Disease Biobank for the CRCLM patient samples, supported through the MUHC Foundation. We gratefully acknowledge Dr. K. Rahimi from the department of pathology and cell biology at CRCHUM for advice and fruitful discussions. We thank Dr. Maïwenn Beaugrand and Adam Prager for their help in the data analysis of cluster growth in suspension.

Author contributions

D.J. and A.M. designed the study. A.M. developed the G μ F and characterized flow profiles. A.M. and S.K. optimized the G μ F process using cell lines, J.A.H.-C. and N. C. fabricated microfilters and J.A.H.-C. conducted flow simulations. S.A.H., performed the orthotopic injection in mice. A.M. microfiltered mouse blood, while A.M., L.C. and N.C. processed patient samples. A.M. N.C. and N.K. conducted morphological and molecular characterization. L.M., D.P. and A-M.M-M. provided ovarian cancer cells and patient samples. A.L and P. M. provided colorectal cancer liver metastasis patient samples. A.M., A.N. and D. J. analyzed the data. A. M. and A.N. wrote the manuscript with D.J.s assistance. All authors discussed the results and commented on the manuscript.

Declaration of Interests

The authors declare no competing interests.

Methods

Materials and reagents. All solutions were prepared using water from a Milli-Q system (resistivity: 18 M Ω cm; Millipore). Phosphate buffered saline (PBS, 1X, pH 7.4, Fisher Scientific), contains $11.9 \cdot 10^{-3}$, $137.0 \cdot 10^{-3}$ and $2.7 \cdot 10^{-3}$ mol L⁻¹ of phosphates (Na₂HPO₄ and KH₂PO₄), NaCl and KCl, respectively. Trypsin-EDTA, bovine serum albumin (BSA), bovine insulin and Tween 20 were obtained from Sigma-Aldrich. Triton X-100 and paraformaldehyde (PFA) were purchased from Fisher Scientific. OSE (Ovarian surface epithelial) medium, L-glutamine and HEPES were obtained from Wisent. RPMI (Roswell Park Memorial Institute) 1640 medium, fetal bovine serum (FBS) and 4',6-diamidino-2-phenylindole (DAPI) were purchased from Life Technologies. Antibiotics (penicillin/streptomycin) were obtained from Invitrogen. Anti-human CD45-PE (cluster of differentiation 45, Cat. #FAB1430P), anti-CK 18-AF 488 (cytokeratin 18, labeled with Alexa Fluor 488, Cat. #IC7619G) and anti-E-Cad (E-cadherin, Cat. #MAB18382, from mouse) were obtained from R&D systems. Anti-Vim (Vimentin, Cat. #SAB4503081, from rabbit), anti-ZO-1 (Zonula occludens-1, Cat. #AB2272, from rabbit), anti-ZEB-1 (Zinc finger E-box-binding homeobox 1, Cat. #SAB3500514, from rabbit), and anti-Snail (Drosophila embryonic protein, Cat. #SAB2108482, from rabbit) were purchased from Sigma-Aldrich. Anti-EpCAM-PE (anti-epithelial cell adhesion molecule labeled with phycoerythrin, Cat. #12-9326-42), anti-c-MET-FITC (hepatocyte growth factor receptor, labeled with fluorescein isothiocyanate, Cat. #11-8858-42), and detection antibodies goat anti-mouse-Alexa Fluor 647 (Cat. #A21240) and goat anti-rabbit-Cy3 (Cyanine 3, Cat. #A10520) were obtained from Fisher Scientific.

Filter fabrication. The filter fabrication process, extensively described elsewhere (Hernandez-Castro et al., 2017), allows for the fabrication of porous membrane with pore diameters of 8, 10, 12, 15, 20 and 28 μ m, referred to as X μ m filters throughout the text. Briefly, pillar structures with a diameter corresponding to that of the pore to be created were prepared by standard photolithography and deep reactive-ion etching (DRIE). A UV-curable polymer cover coated on polyethylene terephthalate (PET) carrier was placed onto the pillars to close the structure. The formed cavity was then filled with Fluorolink® MD 700, which was then cured through UV exposure (2000-EC Series UV curing flood lamp, DYMAX). Finally, the blank cover was peeled off, and the molds were bathed in acetone for 15-20 min, for the membranes to self-de-mold from the pillars. Filters consist of a 20-40 μ m-thick porous membrane heat bonded to a PMMA ring, which defines an 8 mm-diameter filter. Before filtration, filter surface was passivated by incubation in BSA (2% in PBS) to reduce non-specific adsorption on the filter.

Filtration cartridge. The filtration cartridge ($70 \times 40 \text{ mm}^2$) was designed with AutoCAD software (Autodesk Inc.) and 3D printed (Perfactory Micro EDU, Envision Tech) (Meunier et al., 2016). It consists of a top (10 mm high) and bottom (15 mm high) parts with notches to place the filter between toric joints and allow for its alignment with the inlet and outlet. A silicone gasket and a pair of screws and bolts are used for sealing.

Gravity-based microfiltration (G μ F). The G μ F set-up consists of a 60 mL syringe (top reservoir) with its plunger removed, connected to the cartridge using a PEEK (Polyether ether ketone) tube (i.d. 0.75 mm, Sigma Aldrich). The overall setup is immobilized using a retort stand and the inlet tube is clamped before pouring the sample into the top reservoir. In this G μ F, the height of the fluid column determines the pressure, and consequently the flow rate. Flow rate calibration was performed for whole and diluted blood (1:6 (v/v) in PBS), as well as for PBS for various filter porosities and tube lengths. After the first seconds to minutes of filtration, flow rate stabilized and fluctuate around a unique value for one to two hours. Average flow rates were measured by collecting sample droplets at known time intervals (from few seconds to minutes) during filtration. The average flow rate, measured in this stable regime was found to increase linearly with the initial sample column height. For each fluid, calibration curves of the average flow rate as a function of the sample height were established and used to adjust the tube length to achieve a specific flow rate (Figure S1 and Table S1).

Cell culture. All culture media and solutions were sterile and filtered through a $0.2 \mu\text{m}$ filter. The ovarian cancer OV90 cell line was developed in the laboratory of Drs. Provencher and Mes-Masson and has been well characterized (Provencher et al., 2000). It was established from the cellular fraction of a patient's ascites. OV90 cells were maintained in OSE medium, supplemented with 10% FBS, 2% L-glutamine, 1% HEPES, and 1% (v/v) antibiotics (final concentrations of 100 I.U. mL^{-1} penicillin and $100 \mu\text{g mL}^{-1}$ streptomycin). Ovarian cancer OVCAR-3 cells were cultured in RPMI 1640 medium supplemented with 20% FBS, 1% (v/v) penicillin/streptomycin, and 0.01 mg mL^{-1} bovine insulin. Cell lines were validated by short tandem repeat (STR) profiling. For both cell lines, adherent cells were observed releasing single cells and clusters in their surrounding medium. The culture medium, containing released clusters, was changed every 1-2 days, and when adherent cells formed almost confluent layers (80-90%) in flasks, adherent cells were harvested using diluted trypsin. $200 \mu\text{L}$ of the cell suspension was re-suspended in 5 mL of culture medium in a new flask. All cell cultures were maintained in 5% CO_2 at 37°C in 25 cm^2 flasks (Corning).

Spiking experiments with ovarian cell lines. The culture medium containing OV-90 clusters and very few single cells was harvested, centrifuged at 1300 rpm for 5 minutes, and cells and clusters resuspended in PBS. Single cells were obtained by trypsinization of the cell monolayers. Then, OV-90 single cells were diluted in PBS to obtain approximately 20-50 cells per microliter. In order to precisely determine the number of single cells and clusters, 10 μ L droplets were placed between a microscope glass slide and a coverslip. The actual number of cells was manually counted twice on each slide and averaged on 10 droplets. Then, a known number of single cells and clusters was spiked in 1 mL blood samples. Blood was drawn from healthy volunteers (IRB study #BMB-08-012) into 10 mL CTAD tubes (citrate-based anticoagulant containing the platelet inhibitors theophylline, adenosine, and bipyrindamole, BD Vacutainer). Samples were maintained at 4°C and processed within 72 h of collection.

Flow velocity simulations. Modeling studies were performed using the COMSOL Multiphysics software. Flow velocity profiles were obtained by 3D simulations through a cell of 9 pores. Filter clogging was simulated through the same cells with 2/9 closed pores. For G μ F (constant pressure), inlet pressure was fixed and for pump filtration a constant flow rate was applied. Additional details are provided in Table S3.

Orthotopic mouse model of ovarian cancer. Female (8–12 weeks old) athymic nude mice (CrI:NU (NCr)-Foxn1nu; Charles River) were housed at the GCRC (Goodman Cancer Research Centre) animal facility and all procedures were conducted following ethics approval in accordance with the animal care guidelines at the Animal Resource Centre of McGill University. For orthotopic ovarian injections, 10 μ L of Geltrex (Invitrogen) containing 7.5×10^5 OV90 or OVCAR-3 cells as a single-cell suspension were injected into the ovary. No leakage from the injection site was observed. When specified, and prior to the injection, OVCAR-3 cells were fluorescently labeled by lentiviral transduction (OVCAR-3-GFP). Lentivirus was produced in HEK293LT cells, by transfection with the lentiviral transfer vector plasmid (pWPI) that contains enhanced green fluorescent protein (eGFP) (Addgene plasmid # 12254), and provided by Dr. Didier Trono (Lausanne, Switzerland) (McCaffrey et al., 2012). Ovarian tumors formed in ~6 weeks and ascites were detected 8–10 weeks after injection. Animals that did not develop primary tumors, ascites, and metastases were excluded. Blood (~0.5 mL) and ascites (~0.5-2 mL) were collected under isoflurane anesthesia using a 23G needle and processed within 3-5 hours of collection.

Epithelial ovarian cancer patients. Blood and tumor samples from EOC patients were collected with informed consent from the Centre Hospitalier de l'Université de Montréal (CHUM), in the Division of Gynecologic Oncology (Table S4). This part of the study involving human samples was approved by

both institutional ethics committees: the Comité d'éthique de la recherche du CHUM (CÉR-CHUM) and the McGill research ethics office (IRB study #A05-M27-16B). Tumor stage was determined at time of surgery by a gynecologic oncologist. Histopathology and tumor grade were determined by a gynecological pathologist using criteria consistent with the International Federation of Gynecology and Obstetrics (FIGO) classification. Patient plasma CA125 levels were routinely measured during follow up. Blood samples used for CTC capture were kept at 4°C and processed within 1-14 hours of collection.

Colorectal Cancer Liver Metastases blood samples: The study was done in accordance with the guidelines approved by McGill University Health Centre (MUHC) Institutional Review Board (IRB). Prior written informed consent was obtained from all subjects to participate in the study (protocol: SDR-11-066). The study included a total of 13 CRCLM patients. Clinical data were collected for each patient through the locally established hospital database and medical records. Blood samples were collected fresh the day of the experiment in EDTA tubes and processed within 6 hrs. (DO YOU NEED MORE INFO HERE?)

CTC capture. Before filtration, all samples were diluted 1:6 (v/v) in PBS. For filtration at constant flow rate using a syringe pump, samples were placed in a 10 mL syringe. For GµF, flow rate was adjusted by changing tube length based on calibration (Table S1). Initially, the inlet tube was clamped, and the sample was poured into the top reservoir, then filtration would start as the clamp was removed. Unless mentioned otherwise, filtration was performed at room temperature (22-23°C) and after filtration samples were rinsed twice with 5 mL of PBS at the same flow rate as that of filtration.

Cell staining. Cell staining can be performed on the filter, directly in the cartridge after filtration as previously described (Meunier et al., 2016) or after release in a culture dish. Cells were fixed with 3.7% paraformaldehyde (PFA), rinsed with PBS, permeabilized with 0.2% Triton X-100, then rinsed again with PBS. Blocking was performed with 1.0% BSA in PBS supplemented with 0.1% Tween 20. Then, for identification, cells were stained with anti-CK (cytokeratin) 18-Alexa Fluor 488 (2.0 µg mL⁻¹) and anti-human CD45-PE (cluster of differentiation 45, labeled with phycoerythrin, 1.0 µg mL⁻¹) to further sort cancer cells from blood cells. For characterization, CTCs from mouse blood and ascites were stained using anti-E-Cad, anti-Vim, anti-ZO-1, anti-ZEB-1, or anti-Snail (1 mg mL⁻¹), and GAM-647 or GAR-Cy3 (4.0 µg mL⁻¹) for detection. Cells were rinsed with PBS, then their nucleus was counterstained with 4',6-diamidino-2-phenylindole (DAPI, 0.1 µg mL⁻¹).

Cell release. Once filtration was over, the cartridge was placed upside down and 5 mL of PBS (or another fluid, where mentioned) were flown by gravity. Flow rate was controlled by adjusting the tube length.

The fluid passes through the filter from the outlet to the inlet, thus mechanically detaching cells from the filter. The cell suspension was then centrifuged (1300 rpm, 5 min) and re-suspended in PBS before further staining or in culture medium for growth.

Cell viability. Single cell and cluster viability was characterized after processing (dilution, filtration and release) with ovarian surface epithelial (OSE) culture medium (n=625/248, 690/626, and 508/186 single cells/clusters), phosphate buffer solution (PBS, n = 401/225, 199/58, and 474/238), or fetal bovine serum (FBS, n = 542/415, 384/184, and 459/308) using a live/dead kit (Thermofisher, #L3224). Cell suspensions were centrifuged, rinsed with PBS, centrifuged again and stained by incubation with 4.0 $\mu\text{mol L}^{-1}$ of EthD-1 (red, dead cells) and 2.0 $\mu\text{mol L}^{-1}$ of calcein AM (green, live cells) diluted in PBS for 45 min at room temperature. As a positive control, single cells and clusters, directly harvested from culture flasks, were seeded in ultra-low attachment well plates (Corning #3473) to avoid cell adhesion and then incubated for 5 hours at 37°C in OSE, PBS, or FBS. For negative control, dead cells were prepared by incubation in 70% methanol for 45 minutes. Viability, was determined using fluorescence microscopy (excitation/emission wavelengths: 485/530 and 530/645 nm for calcein AM and EthD-1, respectively), corresponds to the ratio between the number of live single cells or clusters versus the total number of single cells or clusters per image, and was averaged over 5 images per condition and three replicated experiments.

Fluorescence microscopy. Filters were placed upside down on the platform of an inverted microscope (TE-2000-E, Nikon) connected to a CCD camera (QuantEM 512SC, Photometrics), and fluorescence images were recorded with NIS-Elements Advanced Research software (Nikon), and analyzed with ImageJ (W. Rasband). Images were collected with a mercury arc lamp and using 41001 (blue, for AF 488, GFP, FITC and Cy3), 41004 (green, for PE and AF647), and 31000v2 (UV for DAPI) filter cubes (Chroma Technology Corp.). Cells are defined as CTC(-like) when they have a nucleus (DAPI) and express CK, a cytoplasmic protein of epithelial origin. White blood cells (WBCs) also possess a nucleus but express CD45. For comparison and relative quantification of the expression levels of E-Cad, Vim, ZEB-1, ZO-1, Snail, EpCAM, and c-MET within different cluster models, same exposure time (1 s) was used for all images.

Migration assay. Growth of OVCAR-3 and OV-90 clusters, isolated from mouse blood, was evaluated using migration assays. About 5×10^5 cells mL^{-1} were seeded in each well of 2-well silicone inserts (Ibidi, Germany) placed on the bottom of a petri dish. Cells were incubated overnight, then the silicon insert was removed. The free-cell area was imaged and averaged over 10 images at different time points. The

closure of the free-cell area overtime (% closure) was thus determined by comparison with the reference, measured right after removing the silicone inserts, and averaged over three replicated experiments (Figure S4A-D).

Sphere forming assay. After capture from mouse blood, OV-90 and OVCAR-3 clusters were re-suspended in culture medium and incubated in ultra-low attachment wells. Spheres were grown for seven days, with gentle mixing once a day by pipetting. Samples were imaged right after seeding and over a few days of incubation using bright field microscopy. The area covered by clusters was measured using ImageJ software. Cluster proliferation in suspension was estimated by averaging the area of ~400-500 clusters over a few days and for three replicated experiments (Figure 4C). Evolution of the area distribution of OV-90 and OVCAR-3 clusters over time is presented in Figure S4E-G.

Statistical analysis. The data are presented as mean \pm standard deviation measured over three replicates. Comparison of quantitative measures carried out on two independent groups was performed using unpaired two-tailed Student's t-tests. Statistical significance was set as $p < 0.05$.

Supplemental Information

All data generated or analyzed in this study are included in this published article and its supplementary information file.

References

- ABDALLA, T. S. A., MEINERS, J., RIETHDORF, S., KONIG, A., MELLING, N., GORGES, T., KARSTENS, K. F., IZBICKI, J. R., PANTEL, K. & REEH, M. 2021. Prognostic value of preoperative circulating tumor cells counts in patients with UICC stage I-IV colorectal cancer. *PLoS One*, 16, e0252897.
- ACETO, N., BARDIA, A., MIYAMOTO, D. T., DONALDSON, M. C., WITTNER, B. S., SPENCER, J. A., YU, M., PELY, A., ENGSTROM, A., ZHU, H., BRANNIGAN, B. W., KAPUR, R., STOTT, SHANNON L., SHIODA, T., RAMASWAMY, S., TING, DAVID T., LIN, CHARLES P., TONER, M., HABER, DANIEL A. & MAHESWARAN, S. 2014. Circulating tumor cell clusters are oligoclonal precursors of breast cancer metastasis. *Cell*, 158, 1110-1122.

- ADAMS, D. L., ZHU, P., MAKAROVA, O. V., MARTIN, S. S., CHARPENTIER, M., CHUMSRI, S., LI, S., AMSTUTZ, P. & TANG, C.-M. 2014. The systematic study of circulating tumor cell isolation using lithographic microfilters. *RSC Advances*, 4, 4334-4342.
- ALLARD, W. J., MATERA, J., MILLER, M. C., REPOLLET, M., CONNELLY, M. C., RAO, C., TIBBE, A. G., UHR, J. W. & TERSTAPPEN, L. W. 2004. Tumor cells circulate in the peripheral blood of all major carcinomas but not in healthy subjects or patients with nonmalignant diseases. *Clinical Cancer Research*, 10, 6897-6904.
- ARFORS, K.-E., BERGQVIST, D., INTAGLIETTA, M. & WESTEREGREN, B. 1975. Measurements of blood flow velocity in the microcirculation. *Upsala Journal of Medical Sciences*, 80, 27-33.
- ARRAZUBI, V., MATA, E., ANTELO, M. L., TARIFA, A., HERRERA, J., ZAZPE, C., TEJEIRA, L., VIUDEZ, A., SUAREZ, J., HERNANDEZ, I. & VERA, R. 2019. Circulating Tumor Cells in Patients Undergoing Resection of Colorectal Cancer Liver Metastases. Clinical Utility for Long-Term Outcome: A Prospective Trial. *Ann Surg Oncol*, 26, 2805-2811.
- ASHWORTH, T. 1869. A case of cancer in which cells similar to those in the tumours were seen in the blood after death. *The medical Journal of Australia*, 14, 146-149.
- AU, S. H., EDD, J., STODDARD, A. E., WONG, K. H. K., FACHIN, F., MAHESWARAN, S., HABER, D. A., STOTT, S. L., KAPUR, R. & TONER, M. 2017. Microfluidic isolation of circulating tumor cell clusters by size and asymmetry. *Scientific Reports*, 7, 2433.
- AU, S. H., STOREY, B. D., MOORE, J. C., TANG, Q., CHEN, Y.-L., JAVAID, S., SARIOGLU, A. F., SULLIVAN, R., MADDEN, M. W., O'KEEFE, R., HABER, D. A., MAHESWARAN, S., LANGENAU, D. M., STOTT, S. L. & TONER, M. 2016. Clusters of circulating tumor cells traverse capillary-sized vessels. *Proceedings of the National Academy of Sciences*, 113, 4947-4952.
- BALLERMANN, B. J., DARDIK, A., ENG, E. & LIU, A. 1998. Shear stress and the endothelium. *Kidney International*, 54, S100-S108.
- BIDARD, F. C., KIAVUE, N., YCHOU, M., CABEL, L., STERN, M. H., MADIC, J., SALIOU, A., RAMPANOU, A., DECRAENE, C., BOUCHE, O., RIVOIRE, M., GHIRINGHELLI, F., FRANCOIS, E., GUIMBAUD, R., MINEUR, L., KHEMISSA-AKOUZ, F., MAZARD, T., MOUSSATA, D., PROUDHON, C., PIERGA, J. Y., STANBURY, T., THEZENAS, S. & MARIANI, P. 2019. Circulating Tumor Cells and Circulating Tumor DNA Detection in Potentially Resectable Metastatic Colorectal Cancer: A Prospective Ancillary Study to the Unicancer Prodige-14 Trial. *Cells*, 8.

- BRANDT, B., JUNKER, R., GRIWATZ, C., HEIDL, S., BRINKMANN, O., SEMJONOW, A., ASSMANN, G. & ZÄNKER, K. S. 1996. Isolation of prostate-derived single cells and cell clusters from human peripheral blood. *Cancer Research*, 56, 4556-4561.
- CANO, A., PEREZ-MORENO, M. A., RODRIGO, I., LOCASCIO, A., BLANCO, M. J., DEL BARRIO, M. G., PORTILLO, F. & NIETO, M. A. 2000. The transcription factor Snail controls epithelial-mesenchymal transitions by repressing E-cadherin expression. *Nature Cell Biology*, 2, 76-83.
- CHENG, S.-B., XIE, M., CHEN, Y., XIONG, J., LIU, Y., CHEN, Z., GUO, S., SHU, Y., WANG, M., YUAN, B., DONG, W.-G. & HUANG, W.-H. 2017. Three-dimensional scaffold chip with thermosensitive coating for capture and reversible release of individual and cluster of circulating tumor cells. *Analytical Chemistry*, 89, 7924-7932.
- COHEN, S. J., PUNT, C. J., IANNOTTI, N., SAIDMAN, B. H., SABBATH, K. D., GABRAIL, N. Y., PICUS, J., MORSE, M., MITCHELL, E., MILLER, M. C., DOYLE, G. V., TISSING, H., TERSTAPPEN, L. W. & MEROPOL, N. J. 2008. Relationship of circulating tumor cells to tumor response, progression-free survival, and overall survival in patients with metastatic colorectal cancer. *J Clin Oncol*, 26, 3213-21.
- EFFENBERGER, K. E., SCHROEDER, C., HANSSSEN, A., WOLTER, S., EULENBURG, C., TACHEZY, M., GEBAUER, F., IZBICKI, J. R., PANTEL, K. & BOCKHORN, M. 2018. Improved Risk Stratification by Circulating Tumor Cell Counts in Pancreatic Cancer. *Clin Cancer Res*, 24, 2844-2850.
- FAN, T., ZHAO, Q., CHEN, J. J., CHEN, W.-T. & PEARL, M. L. 2009. Clinical significance of circulating tumor cells detected by an invasion assay in peripheral blood of patients with ovarian cancer. *Gynecologic Oncology*, 112, 185-191.
- FERREIRA, M. M., RAMANI, V. C. & JEFFREY, S. S. 2016. Circulating tumor cell technologies. *Molecular Oncology*, 10, 374-394.
- FLEISCHER, R. L., PRICE, P. B. & SYMES, E. M. 1964. Novel filter for biological materials. *Science*, 143, 249-250.
- FRISCH, S. M. & FRANCIS, H. 1994. Disruption of epithelial cell-matrix interactions induces apoptosis. *The Journal of Cell Biology*, 124, 619-626.
- GARREL, R., MAZEL, M., PERRIARD, F., VINCHES, M., CAYREFOURCQ, L., GUIGAY, J., DIGUE, L., AUBRY, K., ALFONSI, M., DELORD, J. P., LALLEMANT, B., EVEN, C., DAURES, J. P., LANDAIS, P., CUPISSOL, D. & ALIX-PANABIÈRES, C. 2019. Circulating

- Tumor Cells as a Prognostic Factor in Recurrent or Metastatic Head and Neck Squamous Cell Carcinoma: The CIRCUTECH Prospective Study. *Clin Chem*, 65, 1267-1275.
- GAZZANIGA, P., DE BERARDINIS, E., RAIMONDI, C., GRADILONE, A., BUSETTO, G. M., DE FALCO, E., NICOLAZZO, C., GIOVANNONE, R., GENTILE, V., CORTESI, E. & PANTEL, K. 2014. Circulating tumor cells detection has independent prognostic impact in high-risk non-muscle invasive bladder cancer. *Int J Cancer*, 135, 1978-82.
- GUO, Y.-X., NEOH, K. H., CHANG, X.-H., SUN, Y., CHENG, H.-Y., YE, X., MA, R.-Q., HAN, R. P. & CUI, H. 2018. Diagnostic value of HE4+ circulating tumor cells in patients with suspicious ovarian cancer. *Oncotarget*, 9, 7522–7533.
- HASLEHURST, A. M., KOTI, M., DHARSEE, M., NUIN, P., EVANS, K., GERACI, J., CHILDS, T., CHEN, J., LI, J. & WEBERPALS, J. 2012. EMT transcription factors snail and slug directly contribute to cisplatin resistance in ovarian cancer. *BMC Cancer*, 12, 91.
- HEIDRICH, I., ABDALLA, T. S. A., REEH, M. & PANTEL, K. 2021. Clinical Applications of Circulating Tumor Cells and Circulating Tumor DNA as a Liquid Biopsy Marker in Colorectal Cancer. *Cancers (Basel)*, 13.
- HERNANDEZ-CASTRO, J. A., LI, K., MEUNIER, A., JUNCKER, D. & VERES, T. 2017. Fabrication of large-area polymer microfilter membranes and their application for particle and cell enrichment. *Lab on a Chip*, 17, 1960-1969.
- HOU, H. W., WARKIANI, M. E., KHOO, B. L., LI, Z. R., SOO, R. A., TAN, D. S.-W., LIM, W.-T., HAN, J., BHAGAT, A. A. S. & LIM, C. T. 2013. Isolation and retrieval of circulating tumor cells using centrifugal forces. *Scientific Reports*, 3, 1259.
- JUDSON, P. L., GELLER, M. A., BLISS, R. L., BOENTE, M. P., DOWNS, L. S. & ARGENTA, P. A. 2003. Preoperative detection of peripherally circulating cancer cells and its prognostic significance in ovarian cancer. *Gynecologic Oncology*, 91, 389-394.
- KIM, S., KIM, B. & SONG, Y. S. 2016. Ascites modulates cancer cell behavior, contributing to tumor heterogeneity in ovarian cancer. *Cancer Science*, 107, 1173-1178.
- LECHARPENTIER, A., VIELH, P., PEREZ-MORENO, P., PLANCHARD, D., SORIA, J. & FARACE, F. 2011. Detection of circulating tumour cells with a hybrid (epithelial/mesenchymal) phenotype in patients with metastatic non-small cell lung cancer. *British Journal of Cancer*, 105, 1338–1341.

- LENGYEL, E., BURDETTE, J., KENNY, H., MATEI, D., PILROSE, J., HALUSKA, P., NEPHEW, K., HALES, D. & STACK, M. 2014. Epithelial ovarian cancer experimental models. *Oncogene*, 33, 3619–3633.
- LHEUREUX, S., GOURLEY, C., VERGOTE, I. & OZA, A. M. 2019. Epithelial ovarian cancer. *The Lancet*, 393, 1240-1253.
- LIM, L. S., HU, M., HUANG, M. C., CHEONG, W. C., GAN, A. T. L., LOOI, X. L., LEONG, S. M., KOAY, E. S.-C. & LI, M.-H. 2012. Microsieve lab-chip device for rapid enumeration and fluorescence in situ hybridization of circulating tumor cells. *Lab on a Chip*, 12, 4388-4396.
- MCCAFFREY, L. M., MONTALBANO, J., MIHAI, C. & MACARA, I. G. 2012. Loss of the Par3 polarity protein promotes breast tumorigenesis and metastasis. *Cancer Cell*, 22, 601-614.
- MEUNIER, A., HERNÁNDEZ-CASTRO, J. A., TURNER, K., LI, K., VERES, T. & JUNCKER, D. 2016. Combination of Mechanical and Molecular Filtration for Enhanced Enrichment of Circulating Tumor Cells. *Anal. Chem.*, 88, 8510-8517.
- OZKUMUR, E., SHAH, A. M., CICILIANO, J. C., EMMINK, B. L., MIYAMOTO, D. T., BRACHTEL, E., YU, M., CHEN, P.-I., MORGAN, B., TRAUTWEIN, J., KIMURA, A., SENGUPTA, S., STOTT, S. L., KARABACAK, N. M., BARBER, T. A., WALSH, J. R., SMITH, K., SPUHLER, P. S., SULLIVAN, J. P., LEE, R. J., TING, D. T., LUO, X., SHAW, A. T., BARDIA, A., SEQUIST, L. V., LOUIS, D. N., MAHESWARAN, S., KAPUR, R., HABER, D. A. & TONER, M. 2013. Inertial focusing for tumor antigen-dependent and -independent sorting of rare circulating tumor cells. *Science Translational Medicine*, 5, 179ra47-179ra47.
- PANTEL, K. & SPEICHER, M. R. 2016. The biology of circulating tumor cells. *Oncogene*, 35, 1216-1224.
- POLETTE, M., MESTDAGT, M., BINDELS, S., NAWROCKI-RABY, B., HUNZIKER, W., FOIDART, J. M., BIREMBAUT, P. & GILLES, C. 2007. β -Catenin and ZO-1: shuttle molecules involved in tumor invasion-associated epithelial-mesenchymal transition processes. *Cells Tissues Organs*, 185, 61-65.
- POVEDA, A., KAYE, S. B., MCCORMACK, R., WANG, S., PAREKH, T., RICCI, D., LEBEDINSKY, C. A., TERCERO, J. C., ZINTL, P. & MONK, B. J. 2011. Circulating tumor cells predict progression free survival and overall survival in patients with relapsed/recurrent advanced ovarian cancer. *Gynecologic Oncology*, 122, 567-572.
- PROVENCHER, D., LOUNIS, H., CHAMPOUX, L., TETRAULT, M., MANDERSON, E., WANG, J., EYDOUX, P., SAVOIE, R., TONIN, P. & MES-MASSON, A.-M. 2000. Characterization of four

- novel epithelial ovarian cancer cell lines. *In Vitro Cellular & Developmental Biology-Animal*, 36, 357-361.
- REDDY, R. M., MURLIDHAR, V., ZHAO, L., GRABAUŠKIENE, S., ZHANG, Z., RAMNATH, N., LIN, J., CHANG, A. C., CARROTT, P., LYNCH, W., ORRINGER, M. B., BEER, D. G. & NAGRATH, S. 2016. Pulmonary venous blood sampling significantly increases the yield of circulating tumor cells in early-stage lung cancer. *The Journal of Thoracic and Cardiovascular Surgery*, 151, 852-858.
- RIPPERGER, S., GÖSELE, W., ALT, C. & LOEWE, T. 2012. Filtration, 1. Fundamentals. *Ullmann's Encyclopedia of Industrial Chemistry*. Wiley-VCH Verlag GmbH & Co. KGaA.
- SARIOGLU, A. F., ACETO, N., KOJIC, N., DONALDSON, M. C., ZEINALI, M., HAMZA, B., ENGSTROM, A., ZHU, H., SUNDARESAN, T. K., MIYAMOTO, D. T., LUO, X., BARDIA, A., WITTNER, B. S., RAMASWAMY, S., SHIODA, T., TING, D. T., STOTT, S. L., KAPUR, R., MAHESWARAN, S., HABER, D. A. & TONER, M. 2015. A microfluidic device for label-free, physical capture of circulating tumor cell clusters. *Nat. Methods*, 12, 685-691.
- SEAL, S. H. 1964. A sieve for the isolation of cancer cells and other large cells from the blood. *Cancer*, 17, 637-642.
- SILVA, V. S. E., ABDALLAH, E. A., BRITO, A. B. C., BRAUN, A. C., TARIKI, M. S., DE MELLO, C. A. L., CALSAVARA, V. F., RIECHELMANN, R. & CHINEN, L. T. D. 2021. Baseline and Kinetic Circulating Tumor Cell Counts Are Prognostic Factors in a Prospective Study of Metastatic Colorectal Cancer. *Diagnostics (Basel)*, 11.
- STOTT, S. L., HSU, C.-H., TSUKROV, D. I., YU, M., MIYAMOTO, D. T., WALTMAN, B. A., ROTHENBERG, S. M., SHAH, A. M., SMAS, M. E. & KORIR, G. K. 2010. Isolation of circulating tumor cells using a microvortex-generating herringbone-chip. *Proceedings of the National Academy of Sciences*, 107, 18392-18397.
- TANG, Y., SHI, J., LI, S., WANG, L., CAYRE, Y. E. & CHEN, Y. 2014. Microfluidic device with integrated microfilter of conical-shaped holes for high efficiency and high purity capture of circulating tumor cells. *Scientific Reports*, 4, 6052.
- WANG, C., MU, Z., CHERVONEVA, I., AUSTIN, L., YE, Z., ROSSI, G., PALAZZO, J. P., SUN, C., ABU-KHALAF, M. & MYERS, R. E. 2017. Longitudinally collected CTCs and CTC-clusters and clinical outcomes of metastatic breast cancer. *Breast Cancer Research and Treatment*, 161, 83-94.

- WANG, Y.-L., ZHAO, X.-M., SHUAI, Z.-F., LI, C.-Y., BAI, Q.-Y., YU, X.-W. & WEN, Q.-T. 2015. Snail promotes epithelial-mesenchymal transition and invasiveness in human ovarian cancer cells. *International Journal of Clinical and Experimental Medicine*, 8, 7388–7393.
- YOKOBORI, T., IINUMA, H., SHIMAMURA, T., IMOTO, S., SUGIMACHI, K., ISHII, H., IWATSUKI, M., OTA, D., OHKUMA, M., IWAYA, T., NISHIDA, N., KOGO, R., SUDO, T., TANAKA, F., SHIBATA, K., TOH, H., SATO, T., BARNARD, G. F., FUKAGAWA, T., YAMAMOTO, S., NAKANISHI, H., SASAKI, S., MIYANO, S., WATANABE, T., KUWANO, H., MIMORI, K., PANTEL, K. & MORI, M. 2013. Plastin3 is a novel marker for circulating tumor cells undergoing the epithelial-mesenchymal transition and is associated with colorectal cancer prognosis. *Cancer Res*, 73, 2059-69.
- YU, M., BARDIA, A., WITTNER, B. S., STOTT, S. L., SMAS, M. E., TING, D. T., ISAKOFF, S. J., CICILIANO, J. C., WELLS, M. N., SHAH, A. M., CONCANNON, K. F., DONALDSON, M. C., SEQUIST, L. V., BRACHTEL, E., SGROI, D., BASELGA, J., RAMASWAMY, S., TONER, M., HABER, D. A. & MAHESWARAN, S. 2013. Circulating breast tumor cells exhibit dynamic changes in epithelial and mesenchymal composition. *Science*, 339, 580-584.
- ZHANG, D., ZHAO, L., ZHOU, P., MA, H., HUANG, F., JIN, M., DAI, X., ZHENG, X., HUANG, S. & ZHANG, T. 2017. Circulating tumor microemboli (CTM) and vimentin+ circulating tumor cells (CTCs) detected by a size-based platform predict worse prognosis in advanced colorectal cancer patients during chemotherapy. *Cancer Cell Int*, 17, 6.